ACCESSIBILITY
Open

OSLO METROPOLITAN UNIVERSITY
STORBYUNIVERSITETET

Master's Degree in
Structural Engineering and Building Technology
Department of Civil Engineering and Energy Technology

MASTER THESIS

THESIS TITLE	DATE
Formability analysis of AA6016-T4 aluminium alloy sheets subjected to roping	15.06.2020
	NUMBER OF PAGES 124
AUTHOR(S) Sigbjørn Tveit	SUPERVISOR(S) Aase Reyes

IN COLLABORATION WITH	CONTACT PERSON

SUMMARY

Due to its good formability characteristics, AA6xxx aluminium alloys have become popular as a light-weight alternative to steel for components produced by stamping operations for use in the bodywork of cars. In this thesis, a short introduction to aluminium alloys as a material, along with a general presentation to key theory relevant to metal sheet forming was given, including several state-of-the-art anisotropic yield criteria, hardening laws, and instability and fracture criteria. Some of the presented models were calibrated to data from the experimental programme conducted by Dimitry Vysochinskiy in 2012 on AA6016-T4 sheets subjected to the phenomenon of roping. A method to model the effects of roping in aluminium alloy sheets was proposed and implemented in an FEA-model in LS-DYNA. Using the Yld2003 anisotropic yield criterion, and the isotropic two-term Voce hardening law, experimental forming limit were recreated with good accuracy for proportional strain paths using two different local necking instability criteria.

3 KEYWORDS
Aluminium alloys
FEA-based FLD
Roping

Acknowledgements

First, the author would like to recognize the invaluable assistance provided by supervisor Professor Aase Reyes, who has generously shared from her great knowledge and experience in the field of research through weekly chats. Further gratitude is aimed towards Dr Dimitry Vysochinskiy at the University of Agder (UiA) who conducted the experiments at which this thesis was based upon, and Dr Torodd Berstad at the Norwegian University of Science and Technology (NTNU), who assisted with software which allowed for further explorations.

The efforts made by the support team at DYNAmore Nordic AB, along with Harald Hofseter and Tore Øfsdahl at the department of ICT at Oslo Metropolitan University are also largely appreciated.

Lastly, the author would like to value the support from friends and family, with a special thanks to Brynjulv Tveit for technical and moral support, and to Thea Østerberg and the Østerberg family for their patience and hospitality.

Contents

Acknowledgements i

Contents iii

Notations vi

1 Introduction 1

1.1 Background and motivation 1

1.2 Preliminary work 3

1.3 Objectives and method of research 5

1.4 Outline and scope 5

2 Theory I: General theory 8

2.1 Aluminium 8

2.1.1 Anisotropy and roping 10

2.1.2 AA6016-T4 aluminium alloy 12

2.2 Continuum mechanics and plasticity 13

2.2.1 Cauchy stress tensor 13

2.2.2 Isotropic elasticity 15

2.2.3 Yield functions 16

2.2.4 Hardening and the associate flow-rule 19

2.2.5 Nominal and logarithmic stresses and strains 21

2.2.6 Traverse strain ratios (Lankford constants) 24

2.2.7 Flow-stress ratios 26

2.3 Material failure in metal sheet forming 28

2.3.1 Forming limit diagrams 28

2.3.2 Governing phenomena 30

3 Theory II: Material models 33

3.1 Yield functions 33
3.1.1 Hill48 33
3.1.2 Yld89 38
3.1.3 Yld2000-2d 41
3.1.4 Yld2003 46
3.2 Hardening 49
3.3 Local necking, fracture and damage 50
3.3.1 Non-local instability-criterion (NLIC) 50
3.3.2 Non-local extremal thickness strains deviation-criterion (NLETSDC) ... 51
3.3.3 Through-thickness shear instability criterion (TTSIC) 52
3.3.4 Original Cockcroft-Latham fracture criterion (OCLFC) 54
3.3.5 Generalized incremental stress state dependent damage model (GISSMO) 55
3.4 Roping model 57
4 Calibration 59
4.1 Experimental program by Dimitry Vysochinskiy 59
4.1.1 Uniaxial tensile tests 60
4.1.2 Marciniak-Kuczynski tests 67
4.2 Yield functions 68
4.2.1 Calibration methods 68
4.2.2 Hill48 calibration 73
4.2.3 Yld89 calibration 75
4.2.4 Yld2000-2d calibration 78
4.3 Hardening calibration 81
4.4 Through-thickness shear instability criterion 83
4.5 Roping model calibration 85

5 Non-linear finite element analysis in LS-DYNA 88
5.1 Uniaxial tensile tests 92
5.2 Forming and fracture diagrams from FEA in LS-DYNA 96
5.2.1 FEA-model 96
5.2.2 Non-local extremal thickness strain deviation criterion (NLETSDC) 97
5.2.3 Through-thickness shear instability criterion (TTSIC) 103
5.2.4 Original Cockcroft-Latham fracture criterion (OCLFC) 107
6 Discussion 110
7 Summary and concluding remarks 113
References 116

Notations

AA	*Aluminium Alloy*
FEM	*Finite Element Method*
FEA	*Finite Element Analysis*
BCC	*Body-Centred Cubic*
FCC	*FCC-Centred Cubic*
RD	*Rolling Direction*
TD	*Traverse Direction*
MK	*Marciniak-Kuczynski*
NK	*Nakajima*
NLIC	*Non-Local Instability Criterion*
NLETSDC	*Non-Local Extremal Thickness Strain Deviation Criterion*
TTSIC	*Through-Thickness Shear Instability Criterion*
OCLFC	*Original Cockcroft-Latham Fracture Criterion*
GISSMO	*Generalized Incremental Stress State dependent damage Model*
MSSE	*Minimized Sum of Squared Errors*
PST	*Plain-Strain Tension*
UT	*Uniaxial Tension*
WTM	*Weak Texture Model*
STM	*Strong Texture Model*
FLD	*Forming Limit Diagram*
FLC	*Forming Limit Curve*
DIC	*Digital Image Correlation*
SD	*Standard Deviation*
SIMLab	*Structural Impact Laboratory*
NTNU	*Norwegian University of Science and Technology*
$\boldsymbol{\sigma_{ij}}$	*Cauchy stress tensor*
σ_i	*Cauchy stress tensor normal stress component*

τ_{ij}	*Cauchy stress tensor shear stress component*
$\sigma_1, \sigma_2, \sigma_3$	*Cauchy stress tensor principal components*
$\boldsymbol{\sigma_H}$	*Hydrostatic stress tensor*
σ_m	*Hydrostatic stress*
$\boldsymbol{s_{ij}}$	*Deviatoric stress tensor*
E	*Young's modulus*
v	*Poisson's ratio*
G	*Shear modulus*
$\boldsymbol{\varepsilon_{ij}}$	*Strain tensor*
ε_i	*Strain tensor normal component*
γ_{ij}	*Strain tensor shear component*
$\varepsilon_1, \varepsilon_2, \varepsilon_3$	*Strain tensor principal component*
σ_e	*Effective stress*
ε_e	*Effective strain*
σ^Y	*Yield stress or flow stress*
σ_0	*Yield stress or flow stress in reference direction*
L	*Current length*
L_0	*Original length*
D	*Displacement*
A	*Current area*
A_0	*Original area*
F	*Force*
e	*Nominal strain*
s	*Nominal stress*
ε	*Logarithmic strains*
σ	*Logarithmic (true) stress*
l	*Specimen length-direction*
w	*Specimen width-direction*

t	*Specimen thickness-direction*
ε^t	*Total (logarithmic) strains*
ε^p	*Plastic (logarithmic) strains*
ε^{el}	*Elastic (logarithmic) strains*
θ	*Angle to reference/rolling direction*
R_θ	*Traverse strain ratio*
r_θ	*Flow-stress ratio*
W_p	*Plastic work*
F, G, L, H, L, M, N	*Hill48 anisotropy coefficients*
K_1, K_2	*Yld89 stress tensor invariants*
a, c, h, p	*Yld89 anisotropy coefficients*
M	*Non-quadratic yield function exponent*
$\boldsymbol{X}'_{\boldsymbol{ij}}, \boldsymbol{X}'_{\boldsymbol{ij}}$	*Yld2000-2d linearly transformed stress tensors*
α_i	*Yld2000-2d anisotropy coefficients*
σ'_i, σ''_i	*Yld2003 stress tensor invariants*
a_i	*Yld2003 anisotropy coefficients*
K	*Power/Ludwik's law hardening coefficient*
n	*Power/Ludwik's law hardening exponent*
Θ_{Ri}, Q_{Ri}	*Voce rule hardening coefficients*
Ω_{el}	*Non-local criterion area in NLIC/NLETSDC*
β_{cr}	*Critical thickness strain increment ratio of NLIC*
ξ_{cr}	*Critical thickness strain ratio of NLETSDC*
τ_{cr}	*Critical through-thickness shear stress in NLETSDC*
W_{cr}	*Critical plastic work in OCLFC*
ε_{cr}	*Critical strain at necking in GISSMO*
ε_f	*Critical strain at fracture in GISSMO*
η	*Stress triaxiality*
n	*Damage exponent in GISSMO*

F	*Instability variable in GISSMO*
D	*Damage variable in GISSMO*
$\tilde{D}$	*Strain localization damage in GISSMO*
m	*Fading exponent in GISSMO*
$AMPL_i$	*Amplitude of harmonic thickness perturbation function*
$XOFF_i, YOFF_i$	*Wavelength of harmonic thickness perturbation function*
XWL_i, YWL_i	*Off-set of harmonic thickness perturbation function*
err	*Error function*
w	*Weighting factor of error function*

1 Introduction

1.1 Background and motivation

Due to its good formability characteristics, AA6xxx aluminium alloys have become popular as a light-weight alternative to steel, for components produced by stamping operations for use in the bodywork of cars. The material assessed in this thesis are sheets of aluminium alloy AA6016-T4. As the current material is used in non-visible parts in the bodywork of cars due to its good formability, enhanced knowledge about the behaviour of this material allows for reductions in material use. Weight reduction of automobile constructions has obvious benefits to both the environmental and economic aspects of the production phase. Also, predictability of the structural material's behaviour allows for enhanced performance of the products concerning fuel consumption and crashworthiness.

When designing forming operations to produce formed metal sheet products, numerical simulations by the finite element method (FEM), or finite element analysis (FEA), are used to simulate the non-linear procedures. In such processes, accurate material models to describe plasticity and forming limits are important to successfully design optimized products and production processes without the reliance on trial-and-error research. For aluminium alloys used in metal sheet forming, the anisotropic plasticity characteristics caused by the directional rolling process has therefore been subject to extensive research over the last decades.

In 1948, Robert Hill presented a modification to the Von Mises yield criterion intending to describe the directional differences in stiffness observed in some metals [1]. A higher-order yield criterion that with different exponents could take on shapes bridging the gap between the Von Mises and the Tresca yield criterion, was first presented by Hershey in 1954 [2]. In 1980 Logan and Hosford [3] proved that this yield function was able to closely resemble the yield characteristics of sheet metals with body centred-cubic (BCC) and face centred-cubic (FCC) crystallographic structure and isotropic characteristics when its exponent was respectively set to 6 and 8. From the late 1980s until the middle of the 2000s, Frédéric Barlat with peers published a series of advanced anisotropic

constitutive models based on one or more linear transformations on invariants of the Cauchy stress tensor [4-7]. The yield functions commonly referred to in the literature as Yld89, Yld91, Yld2000-2d, and Yld2004-13p/18p, have different formulations and complexity but have all proved to describe the anisotropic plasticity characteristics of sheet aluminium with good accuracy [8-11].

When implemented into FEA-programs, suiting plasticity models in conjunction with criteria describing the onset of local necking – potentially also accompanied by models predicting ductile damage and shear damage – can for many aluminium alloys generate accurate forming and fracture limits, with and without anisotropy. One approach is to generate forming limit curves inspired by the Marciniak-Kuczynski (MK) model [4], where initial imperfections are implemented into the FEA model causing strain localization to occur as a consequence of imposing force equilibrium. Using the Yld89 plasticity model by Barlat and Lian [5] along with a non-local detection of through-thickness strain concentrations (NLIC) the approach was able to capture experimental forming limits and their strain path dependency of AA2008-T4 and AA6111-T4 sheets in the 2008 article by Reyes et al. [6]. In this study, a through-thickness shear instability criterion (TTSIC) based on the work of Bressan and Williams [7] was also used, displaying results consistent with the MK-inspired approach and experimental limits.

Based on early experiments on AA6016-T4, a 2009 article by Lademo et al. [8] presented FEA-based forming limit strains using a similar thinning-based method to detect strain localizations in a Marciniak-Kuczynski-inspired criterion, in conjunction with the ductile fracture criterion presented by Cockcroft and Latham in 1968 [9]. The predicted limit strains seemed to accurately reproduce the experimental data it was compared to. However, in this study, the anisotropy of the forming limits was not addressed, as the FEA-based forming limits were seemingly only compared to experimental limit strains where the major strain was in the rolling direction of the sheet.

In the work on his thesis for the degree of PhD [10], Dmitry Vysochinskiy in 2012 conducted a relatively extensive experimental program on sheets of rolled aluminium alloy AA6016 with temper T4 with the aim to investigate effects of plastic anisotropy in the material, and to establish an accurate constitutive model for the alloy. While the plastic anisotropy of the material was characterized as rather weak, the presented

experimental forming limit diagrams (FLD) constructed from Marciniak-Kuczynski tests [4] exhibited a clear anisotropic tendency for both necking- and fracture strains. The experimental data was further used to calibrate the advanced anisotropic yield criterion Yld2004-18p by Barlat et al. [11] and a two-term Voce hardening rule. To investigate whether the weak anisotropy of the plasticity of the material was able to describe the severe anisotropy of the forming limits, numerical implementation of the MK-model was used to construct the predicted forming limit diagram. The results displayed a weak anisotropy of forming limits in the opposite direction of what was observed from experiments. From this, a conclusion was drawn that the reduced forming limits in the direction traverse to the rolling direction of the sheet was likely an effect of the roping phenomenon, which was observed through macroscopic valleys and ridges in the sheet surface. The theory was strengthened by the observations of unexpected crack orientations and the formations of multiple local necks observed through digital image correlation (DIC)-based strain mappings.

Attempts to understand and describe the occurrence of the roping phenomenon in aluminium sheets, based on crystal plasticity has been subject to research by several authors [16-19]. However, less attention has been directed towards modelling the phenomenological effects of roping on forming limits and crack orientations. To the knowledge of the author, no attempts to address the anisotropy of forming limits and the occurrence of these “anomalous” crack orientations, as later reported from the extensive experimental program of Dimitry Vysochinskiy, has been conducted for AA6016-T4 sheets subjected to roping. In this thesis, models of anisotropic plasticity, isotropic hardening, instability and fracture will be presented, calibrated and tested in FE-analyses, along with a model to describe the effects of roping.

1.2 Preliminary work

Leading up to the work on this thesis on the formability of aluminium alloy AA6016-T4, two preliminary written reports [20, 21] concerning non-linear analyses of the mechanics of aluminium alloys have been assigned by the author as obligatory assignments during the Master’s Programme Structural Engineering and Building Technology at Oslo

Metropolitan University. Due to this, some formulations in this report may be recognized from previous unpublished but internally distributed work of the author.

The first project report [12], assigned in May 2019 in the course *'Structural Analysis and Design'*, included the assessment of an I-sectioned cantilever beam of aluminium alloy AA6082-T6 with a displacement-controlled point load applied at the tip of the beam. Here, a literature study, along with a non-linear finite element analysis in the FEA software Abaqus/CAE was carried out.

Like this thesis, the second report [13], assigned in December 2019 in the course *'Structural Engineering Specialisation'*, was concerning the formability characteristics of aluminium alloy AA6016 with temper T4. In addition to addressing some of the key theory of metal sheet forming, experimental data from Dimitry Vysochinskiy [10] was used to calibrate the quadratic anisotropic yield criterion Hill48 [1] along with isotropic two-term Voce hardening, and implemented in Abaqus/CAE. An effort was then made to conduct non-linear simulations of tensile tests sampled at 0° and to 90° to the rolling direction, using the limited possibilities provided by pre-programmed modules in Abaqus/CAE. The results were then presented and discussed through comparisons with the isotropic von Mises yield function [14]. While the simulations using the von Mises yield function managed to quite accurately reproduce the materials plastic behaviour for both directions, the Hill48 description yielded a false additional strength in the orientation 90° to the rolling direction. Although the plasticity of the material examined in this study was proved to rather isotropic characteristics, yield criteria with rotational asymmetry seem to be the norm in the literature when dealing with profiles made of extruded aluminium. An important reading from this study was therefore that the Hill48 yield criterion – although it is known to reduce to von Mises by the right calibration – did not produce isotropic yield behaviour when calibrated to an isotopically behaving material. This observation is in agreement with results found in the literature [15] and has been some of the motivation behind further work on developing yield criteria better suited to describe the plasticity of extruded and rolled aluminium alloys.

1.3 Objectives and method of research

The objective of the current work is to gain advanced knowledge in the field of metal sheet forming with aluminium alloys and to model the effects of roping observed in AA6016-T4 aluminium alloy sheets on forming limits with proportional strain paths. To this aim, a literature study will be conducted where theoretical familiarization is to be obtained with governing phenomena and state-of-the-art material models for metal sheet forming with aluminium alloy. Experimental data from Vysochinskiy [10] will then be used to calibrate some of the presented models to the currently assessed material, before non-linear analysis in the finite element analysis LS-DYNA will be conducted.

Ultimately, the described method aims to eventually test the hypothesis that the effects of the roping observed in AA6016-T4 aluminium alloy sheets on forming limits from proportional strain paths can be described by introducing perturbations to the sheet thickness based on the spatial distribution of effective plastic strains observed from experiments.

1.4 Outline and scope

In this thesis some relevant key theory about aluminium and metal sheet forming is first presented in *Ch. 2* Next, a series of established phenomenological mathematical models with application to FEA, which have been used to describe the behaviour of aluminium alloys in metal sheet forming processes, are presented in *Ch. 3*. Here, a model that is used in an attempt to model the effects of roping on forming limits, through scaled harmonic perturbations to the sheet thickness, is also presented. Followed by this, *Ch. 4* presents results from the experimental program of Dimitry Vysochinskiy, which is then used to calibrate some of the material models described in the previous chapter. In *Ch. 5,* an advanced anisotropic plane stress yield function with two criteria to predict local necking and one criterion to predict ductile damage is implemented into an FEA-software along with the presented model to simulate the effects of roping. FEA-based FLDs generated by the different criteria without and with different amplitudes to the implemented roping model is then presented and discussed. Finally, a general discussion and summary of

noticeable discoveries made during the work with the study, in *Ch. 6*, is followed by a conclusion and suggestions to further work in *Ch. 7.* Table 1-1 displays the different yield criteria, hardening laws, instability and fracture criteria presented in this report. Furthermore, it shows which models have been calibrated and then used in finite element analyses.

Table 1-1: Overview of the appearances of material models.

	Model	***Theory***	***Calibration***	***FEA***
Yield functions	*Hill48* [1]	*x*	*x*	
	Yld89 [5]	*x*	*x*	*x**
	Yld2000-2d [16]	*x*	*x*	
	Yld2003 [17]	*x*	*(1)*	*x*
Hardening	*Power law*	*x*	*(2)*	
	Ludwig's law	*x*	*x*	
	One-term Voce	*x*	*x*	
	Two-term Voce	*x*	*(2)*	*x*
Local necking/fracture	*NLIC/NLESDC*	*x*	*x*	*x*
	TTSIC [7]	*x*	*x*	*x*
	OCLFC [9]	*x*	*(2)*	*x*
	GISSMO [18]	*x*		
Roping	*Four-term sine wave*	*x*	*x*	*x*

(1) Calibrated automatically in LS-DYNA

(2) Calibrated by Dimitry Vysochinskiy [10]

** Unsuccessfully*

Disregarding the general theory, the following report can roughly be divided into three parts: a *theoretical* part, a *calibration* part, and an *FEA* part. In the theoretical part, several material models relevant to metal sheet forming are presented. Many of the material models were fitted by the author to data from the experimental program described in the Ph.D.-thesis of Dimitry Vysochinskiy [10], while only a few of the models were used to

conduct FEA in LS-DYNA. To clarify the scope of this report, an overview is displayed in Table 1-1.

2 Theory I: General theory

To establish a theoretical foundation for the following thesis to be built upon, a literature study is presented, where an introduction to aluminium and aluminium alloys as a material is first given. Followingly, a short introduction to the key theory of continuum mechanics and plasticity theory relevant to aluminium sheet forming is given, followed by an introduction to the theory of material failure.

2.1 Aluminium

With the symbol Al and the atomic number 13, aluminium is a solid chemical element which can be found on the periodic table among the metallic elements. Aluminium oxides found in ancient pottery artefacts from Egypt and Rome reveals that the characteristics of the element have been utilized by humans since before the Common Era [19]. While scientists earlier believed that the metal was rare and difficultly extracted, we now know that the raw material bauxite which contains around 15 to 25 per cent of aluminium is found in quantities large enough to make aluminium the third most common element in the Earth's crust.

After the sedimentary rock is extracted from the ground, the production process starts by processing the aluminium oxide – also referred to as alumina – from the raw material by a refining process called the Bayer process. Secondly, the extracted aluminium oxide, which consists of two aluminium atoms and three oxygen atoms, is transformed into pure aluminium by breaking the molecule bonds. The breaking of the bonds is performed using electrolysis in a very energy-demanding process [20]. The pure aluminium metal obtained from the electrolytic reduction carries a little less than half the mass of the aluminium oxide it was produced from [21].

For structural purposes, the pure aluminium is classified in the low-end category of metals due to its extreme malleability. However, the enhanced properties of various nature which can be achieved by adding compounds to the pure metal when in its molten liquid form

is what makes aluminium – or more specifically aluminium alloys – the versatile material it is known to be. An aluminium alloy is a chemical compound where elements such as iron, silicon, zinc, magnesium and manganese have been added to the pure aluminium. One or more additives can together contribute to up to 15 per cent of the weight of the composition of the alloy, where different composition yields different properties. The combination of different compounds affects the alloys strength, workability and density, electric conductivity [22], in addition to visual appearance. Thus – whether the material is to be used in a marine environment, as a car component, as a welded bicycle frame or in an air- or spacecraft – or simply as soda cans or aluminium foil, the aluminium alloy can be tailored to its intended use.

Depending on the product, aluminium alloys are on average between 10 and 40 % lighter than steel. Combined with good formability characteristics and resistance to corrosion, the material has features which are of obvious interest to the automotive industry, where lighter weight and furtherly optimized shapes often are synonyms with enhanced performance. When the world's first aluminium-bodied sports car appearing at the Berlin International Motor Show in 1899, it took only two years before Carl Benz constructed the first aluminium car engine. In other words, the metal has been around in the automotive industry for over a decade although more than 60 years had to pass before aluminium could be considered a commonly used material. Next to steel, the lightweight aluminium alloys is now the second most used material in the automobile industry [19].

For wrought aluminium alloys, the International Alloy Designation System is the most widely accepted naming scheme to identify the different alloys. The designation system, which is a four-digit code often with the prefix "AA", identifies the alloying elements and is sometimes accompanied with a designation for the temper.

*AA**X**XXX* The first digit indicates the principal alloying element which has been added to the alloy. The digit indicates what is often referred to as the aluminium alloy series, running from the 1000 series, up to the 8000 series.

*AAX**X**XX* The second digit indicates the modification of the alloy. If AA6016 is the original alloy, AA6316 would be the third modification to the original alloy.

*AAXX**XX*** The last two digits are simply the arbitrary numbers assigned to the material to separate it from other alloys of the same series [23].

In the automotive industry, aluminium alloys in the 6000-series of are commonly preferred for the use in the bodywork of cars. The series is characterized by a significant amount of added magnesium and silicon, to produce a versatile, weldable and heat treatable alloy with moderately high strength. Also, the series is known for its excellent resistance to corrosion [22].

2.1.1 Anisotropy and roping

While the lattice arrangement of the aluminium atoms is orderly aligned as face-centred cubic, the material is on a microscopical scale divided into crystallites, or grains, which may vary in size and orientation.

Sheets of wrought aluminium alloys used for metal forming purposes are produced by rolling the material to the desired sheet thickness. This process typically leads to a dislocation of the grains in the materials' microstructure. As the microscopic dislocations of grains are due to a directional rolling process, a preferred alignment of the grains can occur which causes the material to exhibit anisotropic plasticity characteristics. Alone, this can lead rolled sheets to display different forming limit strains in the directions parallel and traverse to the rolling direction.

For some aluminium alloys in the 6000-series, the production methods might even cause grains with similar orientations to cluster in bands parallel to the rolling direction of the sheets. These bandings in the spatial distribution of textural components can have enhanced or diminished resistance to thinning [24] when subjected to biaxial stretching. The phenomenon, which also is rather common in ferritic stainless steel sheets, is referred

to in the literature as ridging or roping and can be visually observed as perturbations in the sheet thickness in the form of valleys and ridges [25].

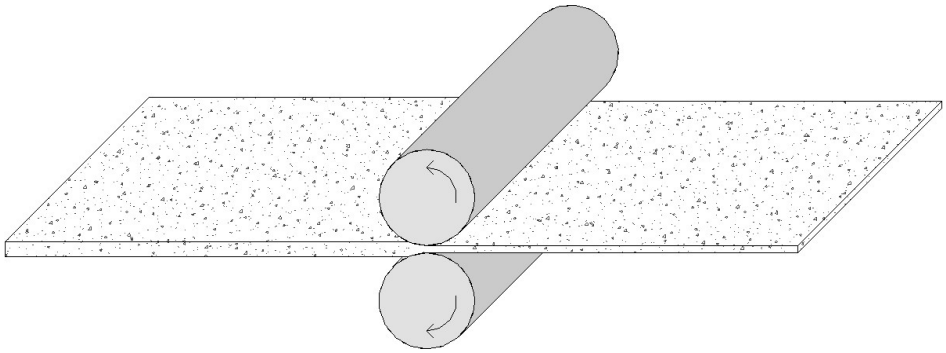

Figure 2-1: Illustration of the cold rolling process of sheet metals.

Several studies based on crystal plasticity-based finite element analysis was been published on the subject of what causes roping to appear in some metal sheets. In such a study on AA6111 automotive sheets by Wu et al. [26], the spatial distribution of clusters of grain orientations are reported to be the predominant factor for roping, while the effects of work hardening and its strain rate sensitivity, crystal elasticity and texture evolution were negligible.

In a 2012 article by O. Engler et al. [24], the correlation between microtextural characteristics and roping in AA6016 aluminium alloy sheets in T4 temper were studied through crystal-plasticity simulations. In Fig. 2-2.a), an optical micrograph rendered with permission from author displays how crystallites with similar orientations, illustrated with similar colours, are clustered in bands parallel to the diagonal rolling direction. For quantitative mapping of the sheets surface topography, sheets prone to roping were stretched by 15 % in the traverse direction to further reveal the textures by white-light interferometry. As displayed in Fig. 2-2.b), the pseudo-3D plot reveals the manifestation of band clusters of grains with similar orientations, as observed in the optical micrograph image.

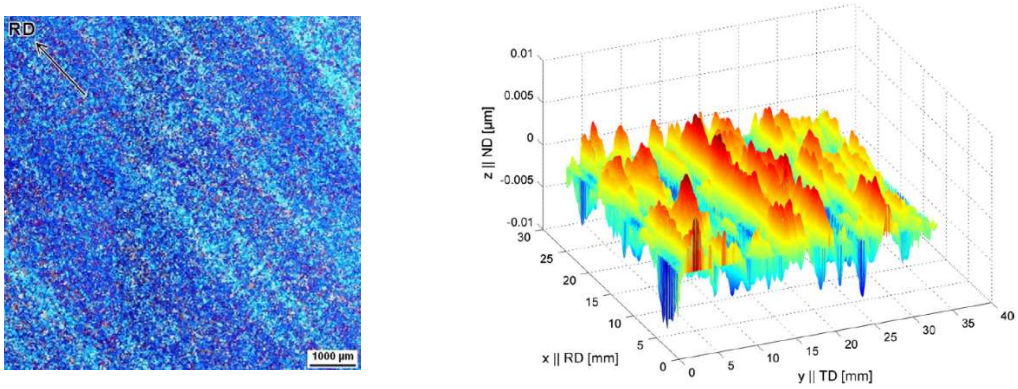

a) *b)*

Figure 2-1: a) Microstructure of an AA6016 sheet in T4 temper. Grains with similar orientations are identified by similar colours, evidently clustered in bands parallel to the diagonal rolling direction. b) Surface topography of sheet with pronounced roping, where the vertical axis represents sheets through-thickness direction.
Both figures are rendered from the 2012 article "Crystal-plasticity simulation of the correlation of microtexture and roping in AA 6xxx Al–Mg–Si sheet alloys for automotive applications" by O. Engler et al. [24] *with permission from the author.*

With the prominent roping in the sheets rolling direction displayed by the alternating valleys and ridges, the above figure serves as great illustrations of the roping effect in the material assessed in the present study. Rather than to explain the reason and cause of plastic anisotropy and roping, the phenomenological effects on forming limits will be addressed further in this thesis.

2.1.2 AA6016-T4 aluminium alloy

The material subjected to assessment in this thesis is 1.5 mm thick sheets of AA6016 aluminium alloy. All information regarding the characteristics of the sheets as described in this section is rendered from the PhD thesis of Dimitry Vysochinskiy [10], where the experimental work which the current thesis is built on, is presented.

Due to its good forming properties, the rolled alloy is suited for use in the bodywork of cars. Its chemical composition is presented in Table 2-1.

Table 2-1: Chemical composition of AA6016 aluminium alloy [10]. Shares of added elements to pure aluminium as percentages of the total composition.

	Si	**Fe**	**Cu**	**Mn**	**Mg**	**Cr**	**Zn**	**Ti**
AA6016	*1.0 - 1.5*	*0.5*	*0.2*	*0.2*	*0.25 - 0.6*	*0.1*	*0.2*	*0.15*

The metal sheets, produced by Hydro Aluminium Rolled Products GmbH, were rolled to their nominal thickness and solution heat-treated before they were stored for six months natural ageing process, giving them the temper designation T4.

In advance of the experimental programme which was carried out by Dimitry Vysochinskiy at Structural Impact Laboratory (SIMLab) at the Norwegian University of Science and Technology, precise measurements of the sheet thicknesses of the sheets as received specified the mean thickness of the sheets to be 1.496 mm with a standard deviation (SD) of 0.004 mm. Prescribed for use in the non-visible parts of the car's bodywork, no quality requirements for the finished surface after the forming process is set. Further presentation of experimental results from this study is presented in *Ch. 4.1*.

2.2 Continuum mechanics and plasticity

2.2.1 Cauchy stress tensor

In continuum mechanics, the triaxial stress state in a three-dimensional material is mathematically described by the symmetric second-order Cauchy stress tensor, $\boldsymbol{\sigma_{ij}}$. Describing the stresses acting on an infinitesimal cube with sides aligned with a cartesian coordinate system where $i = x, y, z$ and $j = x, y, z$, the stress tensor is popularly referred to on the following notation:

$$\left[\boldsymbol{\sigma_{ij}}\right] = \begin{bmatrix} \sigma_x & \tau_{xy} & \tau_{xz} \\ \tau_{xy} & \sigma_y & \tau_{yz} \\ \tau_{xz} & \tau_{yz} & \sigma_z \end{bmatrix} \qquad \text{Eq. 2.2-1}$$

Here, σ_x, σ_y and σ_z are the normal stress components, while τ_{xy}, τ_{yz} and τ_{xz} are the shear stress components. Note that the tensor of nine components can be entirely described by six individual components due to its symmetric nature.

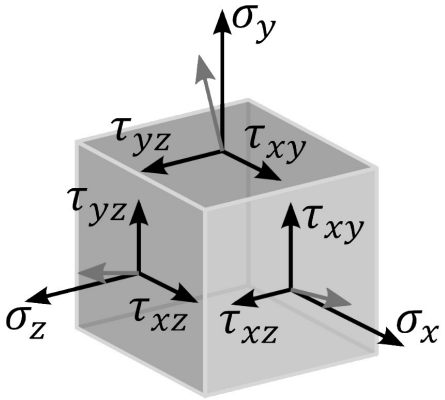

Figure 2-2: Graphical representation of the Cauchy stress tensor in cartesian coordinates. The figure is a modification of an original image publicly free to distribute and modify through Wikimedia Commons [27].

Another feature worth mentioning about the stress tensor is the exitance of the shear stress-vanishing frame of reference. For any physical stress state in an arbitrarily chosen frame of reference, a rotational transformation can be made to a principle reference frame where the stress tensor can be expressed in terms of the three normal stresses alone, in continuum mechanics popularly denoted as σ_1, σ_2 and σ_3, where $\sigma_1 \geq \sigma_2 \geq \sigma_3$.

The stress tensor can be separated into two parts; the hydrostatic stress tensor, $\boldsymbol{\sigma_H}$, which solely contributes to volumetric strains, and the deviatoric stress tensor, $\boldsymbol{s_{ij}}$, which solely contributes to distortional strains, and no volumetric strains.

$$[\boldsymbol{\sigma_H}] = \begin{bmatrix} \sigma_m & 0 & 0 \\ 0 & \sigma_m & 0 \\ 0 & 0 & \sigma_m \end{bmatrix} \quad , \quad \sigma_m = \frac{1}{3}(\sigma_1 + \sigma_2 + \sigma_2) \qquad \text{Eq. 2.2-2}$$

$$[\boldsymbol{s_{ij}}] = [\boldsymbol{\sigma_{ij}}] - [\boldsymbol{\sigma_H}] = \begin{bmatrix} \sigma_x - \sigma_m & \tau_{xy} & \tau_{xz} \\ \tau_{xy} & \sigma_y - \sigma_m & \tau_{yz} \\ \tau_{xz} & \tau_{yz} & \sigma_z - \sigma_m \end{bmatrix} \qquad \text{Eq. 2.2-3}$$

In metal sheet forming, which is mainly governed by stretching in the plane of the sheet, plane stress formulations are often used to simplify the mathematics of the models and computational demand. In plane stress, stresses in the though-thickness direction are neglected due to their vanishing magnitude. If a cartesian coordinate system with the axis x, y and z is introduced so that the z-direction represents the sheet's normal direction, the plane stress-formulation is achieved by setting $\sigma_z = \tau_{yz} = \tau_{zx} = 0$. Furthermore, the matrix describing the Cauchy stress tensor is then contracted to a two-by-two matrix with three independent components, namely σ_x, σ_y and τ_{xy}.

2.2.2 Isotropic elasticity

In isotropic elasticity descriptions, the relationships between triaxial stresses and elastic strains can be formulated by two material constants; the Young's modulus, E, and the Poisson's ratio, ν, which describes the materials tendency to contract and elongate in the traverse directions when subjected to tension and compression, respectively. If a material is deformed in the x-directions, the Poisson's ratio is expressed as

$$\nu = -\frac{\varepsilon_y}{\varepsilon_x} = -\frac{\varepsilon_z}{\varepsilon_x} \qquad \text{Eq. 2.2-4}$$

where ε_x, ε_y and ε_z are the logarithmic strains in the x, y and z-directions of a Cartesian coordinate system. By establishing an expression for the shear modulus from the two independent material parameters as $G = E/2(1 + \nu)$, the relationships between strains and stresses in isotropic elasticity is governed by the constitutive law, $\{\boldsymbol{\sigma_{ij}}\} = [E]\{\boldsymbol{\varepsilon_{ij}}\} \rightarrow \{\boldsymbol{\varepsilon_{ij}}\} = [E]^{-1}\{\boldsymbol{\sigma_{ij}}\}$ as:

$$\begin{Bmatrix} \varepsilon_x \\ \varepsilon_y \\ \varepsilon_z \\ \gamma_{xy} \\ \gamma_{yz} \\ \gamma_{xz} \end{Bmatrix} = \begin{bmatrix} 1/E & -\nu/E & -\nu/E & 0 & 0 & 0 \\ -\nu/E & 1/E & -\nu/E & 0 & 0 & 0 \\ -\nu/E & -\nu/E & 1/E & 0 & 0 & 0 \\ 0 & 0 & 0 & 1/G & 0 & 0 \\ 0 & 0 & 0 & 0 & 1/G & 0 \\ 0 & 0 & 0 & 0 & 0 & 1/G \end{bmatrix} \begin{Bmatrix} \sigma_x \\ \sigma_y \\ \sigma_z \\ \tau_{xy} \\ \tau_{yz} \\ \tau_{xz} \end{Bmatrix} \quad \text{Eq. 2.2-5}$$

Like the stress tensor, the strain tensor, $\boldsymbol{\varepsilon_{ij}}$, is symmetric with six independent components, where ε_x, ε_y and ε_z are the normal strains, and γ_{xy}, γ_{yz} and γ_{xz} are the shear strains. Note that the shear strains, γ_{ij}, are the sums of the two symmetrical counterparts of the strain tensor, ε_{xy} and ε_{yx}, when the tensor is written in matrix form as partial derivatives of the displacements.

In the plane stress formulation – popularly used when describing stresses and strains in metal sheet forming – normal strains in the z-direction, ε_z, is still present due to the effect of the Poisson's ratio, although the stress tensor reduces to only three independent components.

2.2.3 Yield functions

To separate stress configurations corresponding to elastic behaviour from configurations of plastic behaviour, a yield criterion – or yield function – must be implemented into the analysis. Yield criteria are convex functions in stress space which describes a state of the material in terms of stress tensor components attempting to describe the stress configurations which initiates the onset of yield in the material.

The uniaxial tensile test is perhaps the simplest experiment to detect the onset of yield, with its simple stress state where σ_1 is the only non-zero component, the test is used to relate the yield criterion description of effective stresses, σ_e, to the measured yield stress, σ^Y. The function can be defined as

$$f(\sigma_{ij}) = \sigma_e - \sigma^Y \leq 0 \quad \text{Eq. 2.2-6}$$

where $f(\sigma_{ij})$ is the yield function, σ_e is the equivalent stress and σ^Y is the yield stress measured in uniaxial tension.

The perhaps simplest criterion to determine the onset of yield is the Tresca criterion which considers a limit of the maximum shear stresses. Using the notation for principal stresses, the maximum shear stress is calculated as the discrepancy of the largest and the smallest principle strain

$$\sigma_1 - \sigma_3 = \sigma^Y \qquad \text{Eq. 2.2-7}$$

where σ^Y is the materials yield strength in uniaxial tension.

Usually, yield functions for metals are based on the experimentally confirmed observation that the phenomenon of yielding in solid metals occurs independently of the amount of hydrostatic pressure present. From this, the surfaces appear in principle stress space as open, usually rounded, cylinders centred around the hydrostatic axis and can be described in terms of components of the deviatoric stress tensor alone.

The isotropic quadratic von Mises yield criterion, named after the Austrian mathematician Richard Edler von Mises who first rigorously formulated it in 1913, is a quadratic isotropic function which considers the distortion strain energy density of a material to determine the onset of yield [14]. When this quantity reaches the limit observed in a uniaxial tensile test for a material point in a triaxial stress state, the criterion predicts the onset of plastic deformations. In terms of Cartesian stress components, the Von Mises yield criterion is expressed as [28]:

$$(\sigma_y - \sigma_z)^2 + (\sigma_z - \sigma_x)^2 + (\sigma_x - \sigma_y)^2 + 6(\tau_{yz}{}^2 + \tau_{zx}{}^2 + \tau_{xy}{}^2) = 2\sigma^Y \qquad \text{Eq. 2.2-8}$$

Because anisotropic materials yield different values of σ^Y depending on which direction the material is pulled in, a reference direction is chosen where the yield stress is commonly referred to as the *reference yield stress,* σ_0. Due to this, the notations σ_0 and σ^Y are used somewhat interchangeably in the literature. In Fig. 2-4.a), a comparison between the Tresca and Von Mises yield functions are displayed. Although the yield

criteria plotted in this chapter are isotropic, the values on the abscissa and ordinate are normalized by the yield stress, σ_0, for the sake of consistency of figures.

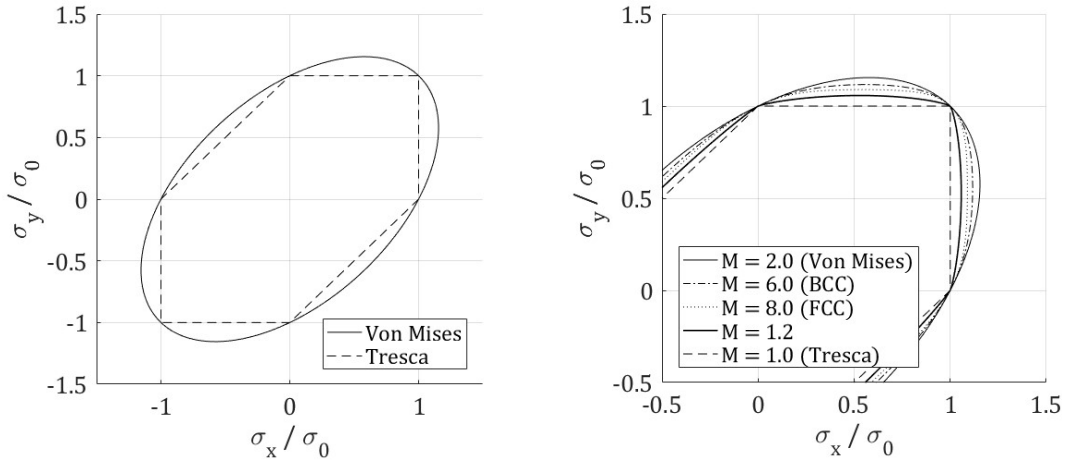

Figure 2-3: a) Comparison between the Tresca maximum shear stress yield criterion and the Von Mises distortion strain energy density criterion in plane stress. b) Hershey non-quadratic yield function with different values of the exponent, M.

A higher-order yield criterion that with different exponents, M, which could take on shapes bridging the gap between the Von Mises and the Tresca yield criterion, was first presented by Hershey in 1954 [2], and later by Hosford in 1972 [29]. In 1980 Logan and Hosford [3] proved that this yield function was able to closely resemble the yield characteristics of sheet metals with body centred-cubic (BCC) and face centred-cubic (FCC) crystallographic structure and isotropic characteristics when the exponent was respectively set to 6 and 8. The yield function was presented by Hosford in 1972 [29] from principal stresses as:

$$|\sigma_1 - \sigma_3|^M + |\sigma_3 - \sigma_2|^M + |\sigma_2 - \sigma_1|^M = 2(\sigma^Y)^M \qquad \text{Eq. 2.2-9}$$

Fig. 2-4.b) displays the Hershey non-quadratic yield function with different values of the exponent, M.

2.2.4 Hardening and the associate flow-rule

As the stress configuration in a material reaches yield, the behaviour of the material is usually characterised by a sudden or gradual drop in stiffness. Nevertheless, the observed continuation of increased stresses for correspondingly increased strains in ductile materials is the reason why the phenomenon is – somewhat confusingly – referred to in the literature as hardening.

Mainly, the increased stresses may affect the state of the yield loci in two different ways – by isotropic or kinematic hardening. As illustrated in Fig. 2-5.a) – for isotropic hardening descriptions, the yield surface keeps its initial shape while it uniformly expands as the yield stress, or flow stress, is increased by strain hardening. From this description, plastic strains would cause the yield stress in tension and the yield stress in compression to rise equally. This type of hardening law is suitable when describing problems where the strain is predominantly in the same direction throughout the analysis, which is the case for uniaxial tension tests.

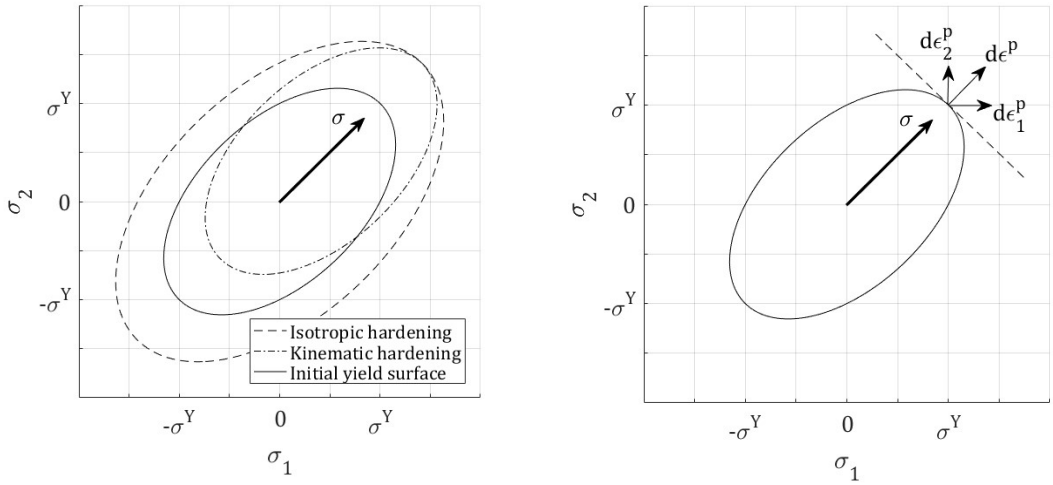

Figure 2-4: a) Conceptual visualization of the effects of kinematic hardening and isotropic hardening on the yield surface in-plane stress. b) Graphical representation of the associated flow rule on a von Mises yield surface (see Ch. 2.2.3) in-plane stress with zero shear component, showing the normality of the strain increment vector on the yield surface.

By kinematic hardening, plastic stains do not affect the shape or size of the yield surface – instead, its location in stress space is shifted. For problems where materials are

subjected to cyclic loading, the kinematic hardening description is used to capture the Bauschinger effect. This material-specific effect where the yield stress is reduced after load-reversal has been observed to occur in many metals [30], including aluminium alloy AA6016-T4 [31].

Whether the nature of the assessed material obeys an isotropic or kinematic hardening or a combination of the two, a flow rule which defines the evolution of the plastic strain tensor and thus the effective plastic strain during hardening is required. The most common one is the associate flow rule, also sometimes referred to in the literature as the normality rule. The rule says that the increments of plastic strains are normal to its associated yield surface during plastic deformations. Mathematically this is the case when plastic strain increment vectors are proportional to the gradient of the yield function:

$$d\varepsilon_{ij} = d\lambda \frac{\partial f(\sigma_{ij})}{\partial \sigma_{ij}} \qquad \text{Eq. 2.2-10}$$

where $f(\sigma_{ij})$ is the yield function as defined in Eq. 2.2-6 and $d\lambda$ is the incremental plastic multiplier which describes the relationship of the plastic increment to the gradient of the yield surface.

In a non-linear analysis, analyses are often path- and time-dependent. Furthermore, the differential notation of the strain increment presented in Eq. 2.2-10 does not hold as a rigorous formulation. Instead, strain increments should be described in terms of the derivatives with respect to time as

$$\dot{\varepsilon}_{ij} = \dot{\lambda} \frac{\partial f(\sigma_{ij})}{\partial \sigma_{ij}} \qquad \text{Eq. 2.2-11}$$

Because the $f(\sigma_{ij})$ in the above equations serves as the potential of a vector field proportional to the possible strain increments, the yield function is sometimes referred to as the plastic potential [28]. The associate flow-rule requires the yield criteria to be able to serve as a plastic potential described in terms of derivative of the yield function. Because the Tresca criterion, as presented in the previous chapter has corners where the curvature of the loci is infinite, yielding undefined normals, the Tresca maximal shear stress criterion cannot serve to describe the evolution of plastic strains.

In addition to the requirement of being differentiable, the convexity of the yield function must be assured to guarantee stable results in non-linear analysis. If a non-convex yield function is allowed to develop through hardening by the associate flow rule, unique solutions of the function cannot be guaranteed. Therefore, a convexity condition is imposed to ensure stable solutions. Proof for a function's convexity is obtained if the Hessian matrix of the function is shown to be positive semi-definite [32]. This is the case when the Hessian matrix, defined as

$$\boldsymbol{H_{ij}} = \frac{\partial f^2(\sigma_{ij})}{\partial \sigma_i \, \partial \sigma_j} \qquad \text{Eq. 2.2-12}$$

is identified to have eigenvalues which are all non-negative [33].

2.2.5 Nominal and logarithmic stresses and strains

Performing uniaxial tensions tests, the nominal stress-strain curve is obtained by coupling the readings of the applied force, with readings of the current length, typically obtained from an extensometer. Based on the known geometry of the test specimen – the initial cross-section area, A_0, and an initial gauge length, L_0 – the engineering strains, e, and engineering stresses, s, are respectively calculated as

$$e = \frac{L - L_0}{L_0} = \frac{L}{L_0} - 1 \qquad \text{Eq. 2.2-13}$$

and

$$s = \frac{F}{A_0} \qquad \text{Eq. 2.2-14}$$

For modelling of post-yield behaviour in FEA-software, the relationship between stresses and strains are typically described in terms of true stresses and logarithmic plastic strains, ε^p, described later in this chapter.

Considering the relationship between infinitesimal current length increments and the current length, integrating from L_0 to L, the true strains can be expressed as the natural logarithm of the relationship between current and original length as

$$\varepsilon = \frac{L - L_0}{L} = \int_{L_0}^{L} \frac{dL}{L} = ln\left(\frac{L}{L_0}\right) \qquad \text{Eq. 2.2-15}$$

Thus, true strains are often referred to as logarithmic strains. Combining the above equation with Eq. 2.2-13, the true strains can be expressed as a function of the nominal strains as

$$\varepsilon = ln\left(\frac{L}{L_0}\right) = ln(e + 1) \qquad \text{Eq. 2.2-16}$$

To find the true stresses, the well-proven assumption of incompressibility – giving zero volumetric true strains, ε_v – is applied to the entire domain, including the elastic regime. By this,

$$\varepsilon_v = \varepsilon_L + \varepsilon_W + \varepsilon_T = ln\left(\frac{L}{L_0}\right) + ln\left(\frac{W}{W_0}\right) + ln\left(\frac{T}{T_0}\right) \qquad \text{Eq. 2.2-17}$$

$$\varepsilon_v = ln\left(\frac{L}{L_0}\right) + ln\left(\frac{A}{A_0}\right) = 0$$

which gives;

$$\varepsilon = ln\left(\frac{L}{L_0}\right) = -ln\left(\frac{A}{A_0}\right) = ln\left(\frac{A_0}{A}\right) \qquad \text{Eq. 2.2-18}$$

An important realization is the limitation of the true strain formulation in terms of the current and initial length. Uniaxial tensile tests are usually accompanied by the phenomenon of diffuse necking. Reduction in the specimen's width-direction occurs when the nominal stress reaches its maximal value. After this, true strains may not be described only in terms of the logarithmic relationship between the current and initial

gauge length. Instead, the area-based formulation should be used. Also, with an expression of the current area,

$$A = A_o \frac{L_o}{L} \qquad \text{Eq. 2.2-19}$$

the true stress as a function of parameters obtained from the uniaxial tension test can be expressed as

$$\sigma = \frac{F}{A} = \frac{F}{A_0}\frac{L}{L_0} \qquad \text{Eq. 2.2-20}$$

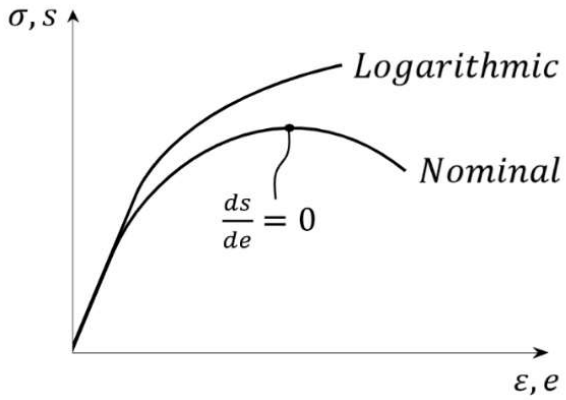

Figure 2-5: Schematic illustration showing the logarithmic (true) and nominal (engineering) stress vs. strain-curves. The onset of diffuse necking in a uniaxial tensile test occurs when the slope of the nominal curve is zero.

From combinations of Eq. 2.2-13 to Eq. 2.2-20 we can summarize the relationships between nominal and true stresses and strains as

$$e(\varepsilon) = \exp(\varepsilon) - 1$$

$$\varepsilon(e) = \ln(1 + e)$$

$$s(\varepsilon, \sigma) = \frac{\sigma}{\exp(\varepsilon)} \qquad \text{Eq. 2.2-21}$$

$$\sigma(e, s) = s(1 + e)$$

As the true stress in a uniaxial tensile test reaches the materials yield stress, σ^Y, the material enters the plastic regime of the stress-strain diagram.

$$\varepsilon^p = \varepsilon^t - \varepsilon^{el} = \varepsilon^t - \frac{\sigma}{E} \qquad \text{Eq. 2.2-22}$$

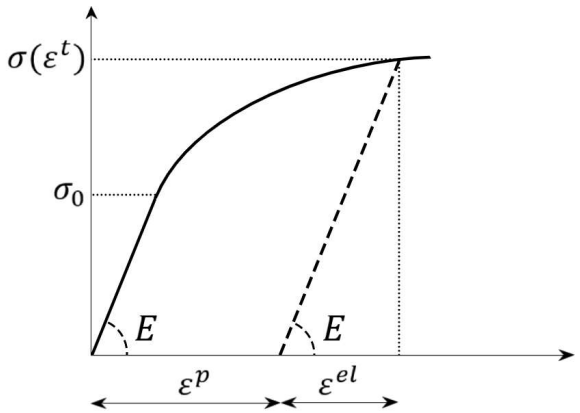

Figure 2-6: Schematic representation of the plastic and elastic portion of the total strains. If a material experiencing stresses in the plastic regime is unloaded, the reversion of stresses and strains follows the dotted line, by the elastic stiffness.

Because the elastic strains are usually very small compared to the plastic strains, the elastic strains are often neglected when considering large strains. Due to this, the plastic strains, ε^p, and the total strains, ε^t or simply ε, are sometimes used interchangeably in the field of plasticity analysis. Although consistency is strived for in this thesis, depending on the context, the notation ε can refer to both total logarithmic strains and large plastic strains. However, in cases where elastic strains make up a considerable share of the total strains, the notation presented in Eq. 2.2-22 holds.

2.2.6 Traverse strain ratios (Lankford constants)

Traverse strain ratios – often referred to in the literature as Lankford constants, R_θ, (also in some literature denoted as r_θ – not to be confused with the flow stress-ratios presented in the next chapter) are defined as the ratio of incremental plastic strains in the width direction, $d\varepsilon_w$, to the incremental plastic strains in the through-thickness direction, $d\varepsilon_t$, [34] of a uniaxial tensile test performed on a specimen sampled at an angle, θ, to the rolling direction of the sheet. Because the ratio of strains in different directions has a

constant proportional relationship during uniaxial tensile tests, the Lankford constant is equally correctly presented in a similar form in terms of plastic strains.

$$R_\theta = \frac{d\varepsilon_w}{d\varepsilon_t} = \frac{\varepsilon_w}{\varepsilon_t} \qquad \text{Eq. 2.2-23}$$

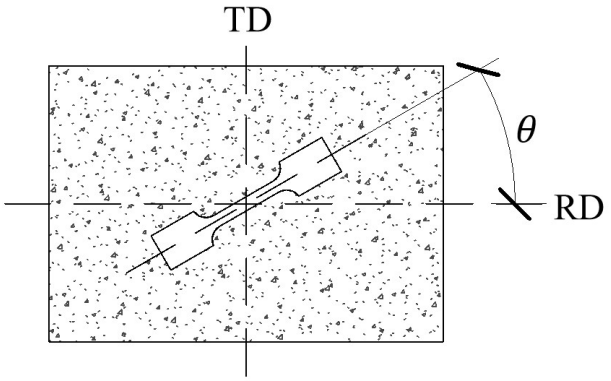

Figure 2-7: Tensile test specimen carved from a metal sheet with denoted material coordinates. θ represented the inclination of the specimen's longitudinal axis to the sheets rolling direction, RD.

Measurements of uniaxial tensile tests have traditionally been conducted using mechanical extensometers. By monitoring the history of length and width displacements of the gauge of the specimen, logarithmic strains in the length and width direction - ε_l and ε_w, can be calculated directly from the equations presented in *Ch. 2.2.5*. Recently, the use of digital image correlation (DIC) [35] where a strain field on the sheet plane of specimens is mapped during the tensile test has become an increasingly common method for the task. While the strains in the specimen width and length directions are detected directly in both methods as a virtual extensometer, thickness strain are calculated from the constant volume assumption, $\varepsilon_l + \varepsilon_w + \varepsilon_t = 0$, due to the difficulties associated with accurately determining the thickness evolution of thin specimens. Thus, the traverse strain ratio becomes

$$R_\theta = \frac{-\varepsilon_w}{\varepsilon_l + \varepsilon_w} \qquad \text{Eq. 2.2-24}$$

2.2.7 Flow-stress ratios

Another measure used to characterize a materials anisotropic plastic behaviour is the flow-stress ratio, r_θ. As sheet metals with anisotropic plasticity might experience variations in yield stress in different orientations, the coefficient was introduced to describe this effect. Although the notations of the traverse strain ratios or Lankford constants presented in the previous chapter, and the flow-stress ratios are switched in some literature, they must not be confused as they represent different physical quantities. While the Lankford constants is a measure of the ratio of the two traverse strains in a uniaxial tensile test sample, the flow-stress ratio represents the flow stress measured in a uniaxial tensile test specimen carved at an angle, θ, to the sheet's rolling direction versus the flow stress in another specimen carved from a reference direction. Usually, the sheets' rolling direction is used as the reference direction.

As the coefficient represents a ratio of measurements taken from different specimens, a quantity relating flow-stresses from different specimens which describe at which point the comparison should be made must be established. For metals where the onset of yield is not clearly distinguished by a yield plateau – as is the case for the material considered in this thesis – the onset of yield is usually defined as the stress measured at a logaithmic strain level of 0.002. Often, these yield stresses are used when calculating the flow-stress ratio. With $\theta = 0$ as the reference directions, the flow-stress ratio can be written as

$$r_\theta = \left.\frac{\sigma_\theta}{\sigma_0}\right|_{\varepsilon_l = 0.002} \qquad \text{Eq. 2.2-25}$$

In a discussion addressing considerations regarding material anisotropy characterization, Barlat et al. [16] points out an issue when processing of experimental test results used for yield function calibration. In addition to how well the yield function manages to capture the material anisotropy, the amount of plastic work – at which experimental data points are harvested at might influence the final accuracy of the calibrated plasticity model when isotropic hardening is assumed. While flow-stresses captured at the onset of yield produces a more accurate description of the separation between elastic and plastic stress states, the approach of using flow-stresses at a chosen magnitude of plastic work might give a better material description for analyses where the whole plastic range is considered.

As the same amount of plastic work might represent different magnitudes of strains in an anisotropic material as illustrated in Fig. 2-9, the accurate definition of the flow-stress ratio is

$$r_\theta = \left.\frac{\sigma_\theta}{\sigma_0}\right|_{W_p} \qquad \text{Eq. 2.2-26}$$

where the flow-stresses,σ_θ and σ_0, are captured at the same magnitude of plastic work, $W_p = \int \sigma_\theta d\varepsilon_\theta^p$.

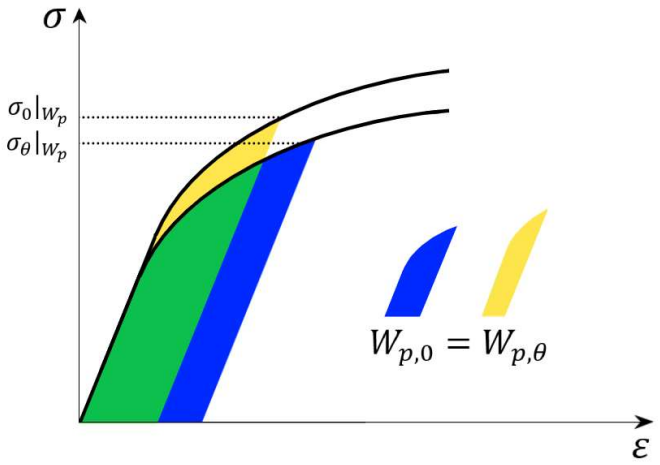

Figure 2-8: Schematic of equivalent plastic work in uniaxial tensile tests with different angles to the rolling direction.

For calibrations of anisotropic plasticity models in this thesis, values of r_θ for AA6016-T4 presented by Dimitry Vysochinskiy in his thesis for the degree of PhD in 2014 [10] were used. Vysochinskiy reports that the presented values were calculated at the onset of yield as described in Eq. 2.2-25. Note that this formulation also obeys the representation presented in Eq. 2.2-26, as the elasticity is considered to be isotropic.

2.3 Material failure in metal sheet forming

If a failure model is not incorporated into the finite element analysis code, the finite element analysis will run according to the specified elastoplastic constitutive behaviour for the entirety of the analysis. Therefore, additional features of the material model must be established and incorporated into the finite element code when material failure is to be simulated.

2.3.1 Forming limit diagrams

For rolled sheets and other thinly extruded aluminium components – which mechanics can be described in terms of stresses in the plane of the components – material failure is generally caused by one of the following mechanisms, or combinations of them; localised necking instability, ductile fracture and shear fracture [36].

In metal sheet forming the state of the material at the occurrence of failure is usually described in terms of the current strains at failure, despite the representation's incapability of yielding results in which corresponds to experimental values in many loading histories. The forming limit diagram (FLD) has played an important role in the industry as a tool for planning and designing forming operations. By performing experiments where different biaxial stress configurations are applied while measuring the evolving strain fields of the specimens beyond the occurrence of failure, a forming limit curve (FLC) which separates safe and unsafe strains combinations can be plotted in biaxial stress space. The domain under the FLC which represents safe strain combinations is often referred to as the forming window.

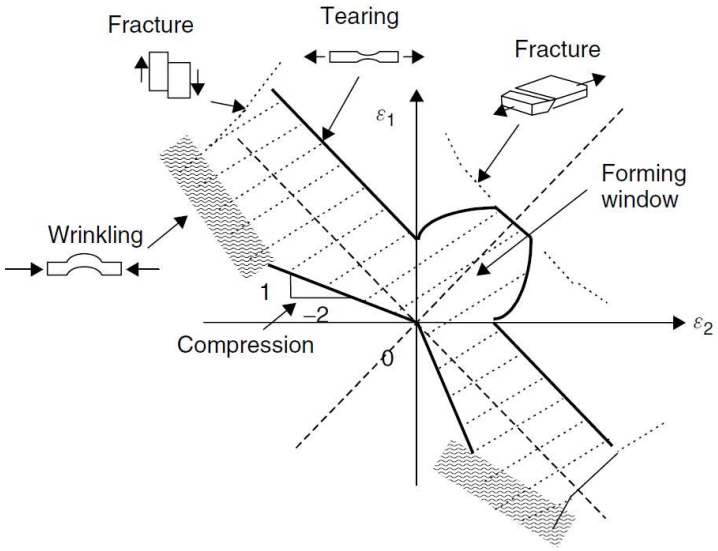

Figure 3-1: Forming limit diagram displaying the state-of-the-art comprehension of relevant failure mechanisms in metal sheet forming. Figure copyrighted to Marciniak et al. [37].

Although the traditional FLDs describing isotropic failure strains, first presented in 1968 by Goodwin [38] and Keeler [39], are plotted with the minor and major biaxial principal strains respectively on the abscissa and ordinate, a presentation in terms of the in-plane material rolling and traverse directional strains is valuable when working with extruded metal sheets of anisotropic mechanical behaviour.

The introduction of ISO 12004-2:2008 [40] provided a standard method to determine strains at the onset of failure. Still, the need for further research to address scatter in reported FLDs from different research teams and laboratories is pointed out by Vysochinskiy et al. [41]. Due to this, considerations should be made regarding the accuracy of experimentally obtained forming limit diagrams. However, the evaluation of different experimental methods is beyond the scope of this report.

A weakness of the forming limit diagram is the fact that it only serves as a valid damage criterion for processes of proportional strain paths, i.e. when strain increments remain constant throughout the forming process. Thus, the traditional method is incapable of predicting damage in processes which are non-proportional e.g. due to pre-strains or geometric conditions of the formed part. To deal with this issue, various versions of stress-based forming limit stress diagrams have been introduced and evaluated in the literature [47-50]. The overall conclusion to be drawn is that a much less strain path-

dependent damage criterion can be obtained by using an appropriate constitutive law to map forming limit strains into biaxial stress space, or onto the axis of equivalent plastic strains along with ratios of principle stresses [42] or principle strain increments [43].

The failure strains predicted by the different failure mechanisms depends on multiple factors. Intuitively, the characteristics on the material itself – including its homogeneity, ductility and plastic symmetry – plays a role. Additionally, geometric imperfections such as random or structured variances in the sheet thickness can cause components to be more or less favourable to experience failure due to local necking instabilities. Two other dependencies – which are neglected throughout the entirety of this thesis due to the narrowing on quasi-static loading conditions – are the influences of temperature and strain rates. Lastly, the influence of the strain path history and the state of stress has proved to have large influences on predicted failure strains, making the task of accurately simulating failure by computationally inexpensive macroscopic models an intricate task.

2.3.2 Governing phenomena

In Fig. 3-1 the state-of-the-art comprehension of the governing failure mechanisms relevant for metal sheet forming as presented by Marciniak et al. in 2002 [37] is displayed. In the figure, *tearing* refers to what is often denoted as local necking instability in modern literature on the field.

Localized necking instability, which is the primary phenomenon leading to fracture in ductile metal sheets [36], is commonly described to be a natural consequence of the equilibrium equations and the constitutive relationship between stresses and strains, where strain localizations eventually occurs by the presence of material imperfections, typically in forms of random or structured variances in the sheet thickness. Though the model only considers isotropic power-law hardening and linear strain paths, the model is perhaps best comprehended by studying the work of Marciniak and Kuczynski (MK) et al. [53, 42] who described the natural evolution of local strains up until instability at the presence of an initial thickness imperfection in a uniaxial tensile test. Furtherly, Marciniak in the same work presented an incomplete model to predict the observed phenomenon of local necking for metal sheet in biaxial tension – based on the same

principles – with the previously stated restrictions, where the initiation of local necking is postulated to occur then the major tension reaches its maximum value. The method has later been developed into what is commonly known as the MK-model. In another theory, Bressan and Williams in a 1982 article [7] suggested that shear instability on critical planes could be the underlying phenomenon of instabilities in sheet metals. The theory was based on observations that many of the models that up until then had been successful in describing forming limits, had the criterion intrinsically built into them. In addition, fractures caused by biaxial stretching had been observed in experiments to produce fracture planes inclined near the plane of maximum shear stress at 45°.

At the onset of instability, a thinning neck with a width measuring in the order of the sheet thickness forms, immediately causing strain localization which at once is followed by rupture of the material. Because the typical shell element size in large scale FE-analysis is often several times larger than the width of the local neck, capturing the evolution of strains up until a fracture strain is reached is not practically feasible in such cases. However, due to the rapidness of the process, the global strains at the onset of instability is typically used as a slightly conservative failure criterion in finite element simulation when the lengths of the mesh elements are greater than 5 times the sheet thickness [36].

Another phenomenon which leads to failure in metal sheet forming is ductile damage. Ductile fracture is a consequence of damage caused by the onset of void nucleation in the material, which further grows before they coalescence, leading to fracture in the material, illustrated in Fig. 3-2.

Any load and/or temperature-induced stress state is associated with some damage. Once the damage reaches a material-dependent critical level, the material fails. Especially for cast aluminium alloys and high strength steel qualities, which have significantly lower ductility compared to wrought alloys, material models which also considers material damage has been proved to be important to obtain reliable results for energy absorption [54, 55]. In advanced general-purpose finite element analysis programs such as Abaqus/CAE and LS-DYNA, coupled damage and failure models for ductile metals which can be used in conjunction with the classical metal plasticity models are often provided. The models are used by defining one or more damage initiation criteria, as well as specifying the evolutions of the respective damage models after initiation, up until a

failure that is induced by removing elements meeting a failure criterion. With strict requirements for safety and crashworthiness in the automotive industry, the field of damage mechanics for sheet metals and its implementations into FE-codes has in recent years been subject to extensive research. However, uncoupled models which nevertheless incorporates fracture from ductile damage can be satisfying for may purposes.

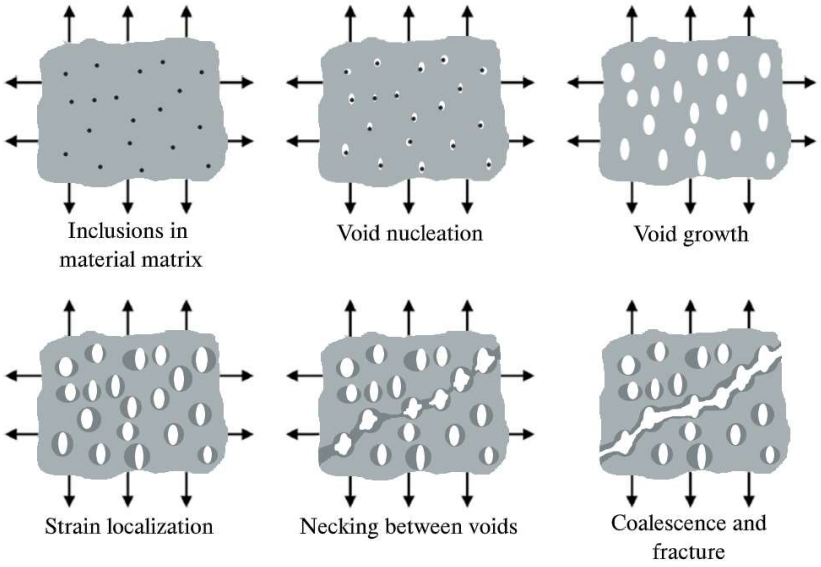

Figure 3-2: Schematic illustration of nucleation, growth and coalescence of voids, leading to failure by ductile fracture. The figure is inspired by the work presented in a 2017 article by Gatea Shakir et al. [44].

To fully comprehend the mechanics of fracture in metals sheets, knowledge of crystal plasticity theory is required, but this is considered beyond the scope of what will be addressed in this thesis. Instead, a brief introduction to relevant theory about material failure in metal sheet forming was given in this chapter. Later in the following chapter some models based on macroscopic stresses and strains used to describe instabilities in finite element analysis for metal sheet forming – including onset and evolution of damage after initiation – will be presented.

3 Theory II: Material models

To describe the several phenomena addressed in the previous theory chapter, multiple authors have published articles presenting models to mathematically predict and simulate the behaviour of metals, where some has gained more attention than others. In the following chapter the theory of some material models which could be more and less suited for use in FEA-models to describe the behaviour of AA6016-T4 subjected to the phenomenon of, roping will be presented.

Additionally, a model where a sum of four sine waves is fitted to a sheet's thickness profile obtained from measurements – aiming to attempt to model the effects of roping as scaled harmonic perturbations to the sheet thickness – is presented in the final section of this chapter. As such a thickness profile was not available in this study, a fictive thickness profile based on the actual mean thickness and standard deviations of the sheets sampled in the experimental program of Vysochinskiy was used instead.

3.1 Yield functions

3.1.1 Hill48

The Hill yield criterion is a generalized version of the Von Mises yield criterion and was presented by Rodney Hill in 1948 [1]. The theory assumes symmetry in yield strength for compressive and tensile stresses but accounts for anisotropic behaviour assumed to appear on three orthogonal axes through six constants, F, G, H and L, M, N, hereby referred to as the *normal stress Hill's constants* and the *shear stress Hill's constants*, respectively. In a Cartesian coordinate system, the Hill48 potential function or yield criterion is on the form

$$2f(\boldsymbol{\sigma_{ij}}) \equiv F(\sigma_y - \sigma_z)^2 + G(\sigma_z - \sigma_x)^2 + H(\sigma_x - \sigma_y)^2 + 2(L{\tau_{yz}}^2 + M{\tau_{zx}}^2 + N{\tau_{xy}}^2)$$

$$2f(\boldsymbol{\sigma_{ij}}) = 1 \qquad \text{Eq. 3.1-1}$$

Isotropy is obtained when $F = G = H$ and $L = M = N = 3F$, and Eq. 3.1-1 reduces to the Von Mises criterion when $2F = (1/\sigma^Y)$.

In metal sheet forming, a cartesian coordinate system is conventionally aligned with the axis of anisotropy of the undeformed sheet, aligning the x-, y- and z-axis with the rolling, traverse and sheet normal directions, respectively.

Based on the assumption of orthogonal anisotropy, considering yielding from uniaxial stresses (when $\sigma_i = \sigma_i^Y$ and all other components in the stress tensor are zero) in the three orthogonal directions, the following three equations are obtained

$$(\sigma_x^Y)^2(G+H) = 1, \qquad \left(\sigma_y^Y\right)^2(H+F) = 1, \qquad (\sigma_z^Y)^2(F+G) = 1, \qquad \text{Eq. 3.1-2}$$

allowing to obtain the following expressions for the normal stress Hill's constants

$$F = \frac{1}{2}\left(\frac{1}{\left(\sigma_y^Y\right)^2} + \frac{1}{(\sigma_z^Y)^2} - \frac{1}{(\sigma_x^Y)^2}\right)$$

$$G = \frac{1}{2}\left(\frac{1}{(\sigma_z^Y)^2} + \frac{1}{(\sigma_x^Y)^2} - \frac{1}{\left(\sigma_y^Y\right)^2}\right) \qquad \text{Eq. 3.1-3}$$

$$H = \frac{1}{2}\left(\frac{1}{(\sigma_x^Y)^2} + \frac{1}{\left(\sigma_y^Y\right)^2} - \frac{1}{(\sigma_z^Y)^2}\right)$$

A similar expression for N is obtained in the same way as in Eq. 3.1-3 giving:

$$N = \frac{1}{2\left(\tau_{xy}^Y\right)^2} \qquad \text{Eq. 3.1-4}$$

As shear strains with relation to the z-axis, τ_{yz} and τ_{zx}, are usually zero in sheet metal forming, efforts to obtain the corresponding shear stress Hill's constants, L and M, can be disregarded when working with sheet metal formability.

While the yield strengths in the rolling and traverse directions, σ_x^Y and σ_y^Y, easily can be determined for sheet metals from tensile tests of specimens carved at 0° and 90° angles, directly obtaining the yield strength in the sheet normal direction, σ_z^Y, from tensile tests is not achievable for thin metal sheets.

To address this problem, measurements of traverse strain ratios during uniaxial tensile tests (as described in *Ch. 2.2.6*) are used together with the associate flow rule to determine the normal stress Hill's constants when σ_z^Y cannot be obtained directly from experiments. Expressing the shear stress terms in the yield criterion by means of the symmetric and anti-symmetric counterparts from the stress tensor on the form $L\left({\tau_{yz}}^2 + {\tau_{zy}}^2\right) + M({\tau_{zx}}^2 + {\tau_{xz}}^2) + N\left({\tau_{xy}}^2 + {\tau_{yx}}^2\right)$, the strain increments can be obtained from the associate flow rule. Applying Eq. 2.2-9 to the Hill48 criterion the six distinct strain increments are [28]:

$$
\begin{aligned}
d\varepsilon_x &= d\lambda\left[H\left(\sigma_x - \sigma_y\right) + G(\sigma_x - \sigma_z)\right] \\
d\varepsilon_y &= d\lambda\left[F\left(\sigma_x - \sigma_y\right) + H(\sigma_x - \sigma_z)\right] \\
d\varepsilon_z &= d\lambda\left[G\left(\sigma_x - \sigma_y\right) + F(\sigma_x - \sigma_z)\right] \\
d\varepsilon_{yz} &= d\varepsilon_{zy} = d\lambda\left[L\tau_{yz}\right] \\
d\varepsilon_{xz} &= d\varepsilon_{zx} = d\lambda[M\tau_{xz}] \\
d\varepsilon_{xy} &= d\varepsilon_{yx} = d\lambda\left[N\tau_{xy}\right]
\end{aligned}
\qquad \text{Eq. 3.1-5}
$$

Substituting $d\varepsilon_i$ in the above equations with the expressions from Eq. 3.1-3 gives:

$$
R_0 = \frac{H}{G} \quad \text{, and} \quad R_{90} = \frac{H}{F} \qquad \text{Eq. 3.1-6}
$$

From this, the normal stress Hill's constants can be expressed from quantities obtained from the two tensile tests as [45]

$$
F = \frac{R_0}{R_{90}(1 + R_0)}
$$

$$G = \frac{1}{(1 + R_0)} \qquad \text{Eq. 3.1-7}$$

$$H = 1 - G = 1 - \frac{1}{(1 + R_0)}$$

Lastly, the relevant shear stress Hill's constant can be obtained by performing yet another tensile test at an angle, $0° < \alpha < 90°$, to the rolling direction. To establish a relationship between the stresses in material coordinates, $\boldsymbol{\sigma_{ij}}$, and the stresses in the specimen coordinates, $\boldsymbol{\sigma'_{ij}}$, a transformation matrix to perform a clockwise rotation of angle α is written as

$$[T_\alpha] = \begin{bmatrix} \cos\alpha & \sin\alpha & 0 \\ -\sin\alpha & \cos\alpha & 0 \\ 0 & 0 & 1 \end{bmatrix} \qquad \text{Eq. 3.1-8}$$

Using the specimen coordinates established earlier as $x' = l$, $y' = w$ and $z' = t$, local stresses at yield in the uniaxial tension test at angle α are written as

$$\left[\boldsymbol{\sigma'_{ij}}\right] = \begin{bmatrix} \sigma'_x & \tau'_{xy} & \tau'_{xz} \\ \tau'_{xy} & \sigma'_y & \tau'_{yz} \\ \tau'_{xz} & \tau'_{yz} & \sigma'_z \end{bmatrix} = \begin{bmatrix} \sigma'_l & \tau'_{lw} & \tau'_{lt} \\ \tau'_{lw} & \sigma'_w & \tau'_{wt} \\ \tau'_{lt} & \tau'_{wt} & \sigma'_t \end{bmatrix} = \begin{bmatrix} \sigma_\alpha^Y & 0 & 0 \\ 0 & 0 & 0 \\ 0 & 0 & 0 \end{bmatrix} \qquad \text{Eq. 3.1-9}$$

The stress tensor can thus be written in the frame of reference of the material coordinates as

$$\left[\boldsymbol{\sigma_{ij}}\right] = [T_\alpha]^T\left[\boldsymbol{\sigma'_{ij}}\right][T_\alpha] = \sigma_\alpha^Y \begin{bmatrix} \cos^2\alpha & \cos\alpha\sin\alpha & 0 \\ \cos\alpha\sin\alpha & \sin^2\alpha & 0 \\ 0 & 0 & 0 \end{bmatrix} \qquad \text{Eq. 3.1-10}$$

Substituting from Eq. 3.1-10 into the yield criterion, the shear stress Hill's constant N can straightforwardly be solved for. Sampling the diagonal tensile test specimen at an angle of 45°, the expression for the last relevant shear stress Hill's constant is

$$N = 2\sigma_{45}^Y - \frac{(F + G)}{2} \qquad \text{Eq. 3.1-11}$$

where σ_{45}^{Y} is the yield stress from a uniaxial tensile test where the angle between the specimen's longitudinal axis and the rolling direction in 45°.

From this, the predicted Lankford constant can be calculated from

$$R_{45}^{pre} = \frac{2N - (F + G)}{2(F + G)} \qquad \text{Eq. 3.1-12}$$

In some cases (as in the FEA-software Abaqus/CAE) the anisotropic yield characteristics of metals are specified in terms of anisotropic yield stress ratios, Rij, where $i = 1, 2, 3$ and $j = 1, 2, 3$ are referring to orthogonal spatial directions of anisotropy. Unlike the continuum mechanics description presented in *Ch. 2.2.1*, where 1, 2 and 3 maps to directions of principal stress where $\sigma_1 \geq \sigma_2 \geq \sigma_3$, this is not necessarily the case in the current description – here, 1, 2 and 3 will be referring to the material directions previously established as x, y and z, where x is the rolling direction, y is the traverse direction, and z is the through-thickness direction of the sheet metal.

Choosing the rolling direction, x, as the reference direction, the four anisotropic yield stress ratios relevant for sheet metal forming can be calculated from the Lankford constants obtained from uniaxial tensile tests at 0° and 90° angle to the reference rolling direction, along with the predicted Lankford constant at 45° as presented in Eq. 3.1-12

$$\begin{aligned} R11 &= \frac{\sigma_x^Y}{\sigma_x^Y} = 1 \\ R22 &= \frac{\sigma_y^Y}{\sigma_x^Y} = \sqrt{\frac{R_{90}(R_0 + 1)}{R_0(R_{90} + 1)}} \\ R33 &= \frac{\sigma_z^Y}{\sigma_x^Y} = \sqrt{\frac{R_{90}(R_0 + 1)}{(R_0 + R_{90})}} \\ R12 &= \sqrt{\frac{3(R_0 + 1)R_{90}}{(2 \cdot R_{45}^{pre} + 1)(R_0 + R_{90})}} \end{aligned} \qquad \text{Eq. 3.1-13}$$

3.1.2 Yld89

The plane stress anisotropic yield function introduced by Barlat & Lian in 1989 [5] – popularly referred to as Yld89 – is based on introducing modifications to the non-quadratic isotropic yield function by Hershey [2] which was presented in Ch. 2.2.3. A drawback with the original yield function formulation in terms of principle stresses – in addition to its isotropic nature – is the lack of interaction between normal stresses and shear stresses. In preliminary work leading up to Yld89, Barlat & Richmond [46] in 1987 presented calculations based on polycrystalline plasticity which suggested that such a coupling should exist for models describing isotropic FCC metals.

From this, a modification to the Hershey yield function starts by expressing the isotropic yield function in-plane stress in terms of two stress tensor invariants, K_1 and K_2 to introduce the shear stress coupling. In Cartesian coordinates that are aligned with the sheet metal's axes of anisotropy, the isotropic function then takes the following form

$$|K_1 + K_2|^M + |K_1 - K_2|^M + |2K_2|^M = 2(\sigma^Y)^M \qquad \text{Eq. 3.1-14}$$

$$K_1 = \frac{\sigma_x + \sigma_y}{2}$$

$$K_2 = \sqrt{\left(\frac{\sigma_x - \sigma_y}{2}\right)^2 + {\tau_{xy}}^2} \qquad \text{Eq. 3.1-15}$$

In Fig. 3-3, a yield surface is plotted for different values of the shear component τ_{xy}. The outer contour line illustrates the shape of the yield loci when $\tau_{xy} = 0$, while the inner contour represents a higher value of τ_{xy}. As the size and shape of the loci changes with varying magnitudes of the shear component, a coupling between the shear component and the normal stresses exists in the new formulation.

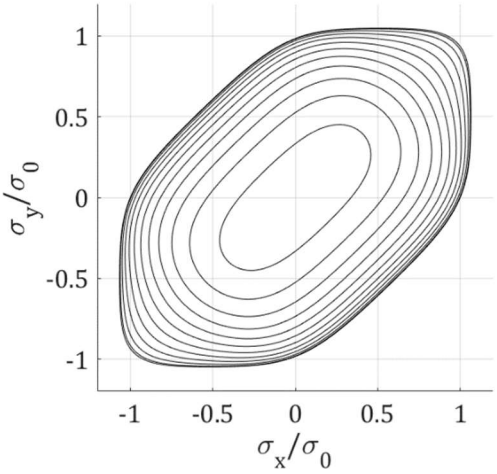

Figure 3-3: Schematic illustration of a shear stress-coupled yield surface plotted for different values of the shear component τ_{xy}. The shape change for different values of τ_{xy} indicates a coupling between shear stress and normal stresses.

As a next step, three constants a, b and c are applied to the yield function to characterize the anisotropy:

$$a|K_1 + K_2|^M + b|K_1 - K_2|^M + c|2K_2|^M = 2(\sigma^Y)^M \qquad \text{Eq. 3.1-16}$$

To obtain continuity for the derivatives of this function at equibiaxial stresses the relationship between the applied constants must according to Barlat and Lian be

$$a = b = 2 - c \qquad \text{Eq. 3.1-17}$$

where a, b and c must always be positive to ensure convexity. The resulting function – which is proved by Barlat and Lian to obey the convexity condition – is lastly complimented with a dilatation to the relationships between the current components of the stress tensor. Finally, the Yld89 yield function with the four anisotropy coefficients a, c, h and p is presented as a function of the Cauchy stress tensor:

$$f = a|K_1 + K_2|^M + a|K_1 - K_2|^M + c|2K_2|^M = 2(\sigma^Y)^M$$

$$K_1 = \frac{\sigma_x + h\sigma_y}{2} \qquad \text{Eq. 3.1-18}$$

$$K_2 = \sqrt{\left(\frac{\sigma_x - h\sigma_y}{2}\right)^2 + p^2{\tau_{xy}}^2}$$

As the previous function has been proved to satisfy the convexity requirement, the argument still holds for Yld89 as the anisotropy coefficients h and p are simply linear transformations of the input arguments of the function. For the quadratic form of the function, Yld89 reduces to the Hill48 [1] yield function which has been presented in detail in the previous chapter.

As the relationship between a and c is specified from Eq. 3.1-17 to ensure continuity of the yield function, the function only needs to be calibrated for three anisotropy coefficients if M is assumed to be known for BCC and FCC structured materials. Experimental data to obtain the unknown parameters are suggested in the original article to be calibrated in a semi-analytical manner from traverse strain ratios obtained from uniaxial tensile tests at three different directions – e.g. R_0, R_{15} and R_{90}.

Using the associate flow rule along with the constant volume assumption and the Euler's theorem on homogeneous functions, the traverse train ratio for a uniaxial tensile test specimen with its longitudinal axis inclined with angle θ to the rolling direction is presented as

$$R_\theta = \frac{2M(\sigma^Y)^M}{\left(\frac{\partial f}{\partial \sigma_x} + \frac{\partial f}{\partial \sigma_y}\right)\sigma} - 1 \qquad \text{Eq. 3.1-19}$$

where σ is the tensile stress in the uniaxial tensile test specimen.

In the original article by Barlat and Lain, the expressions for the partial derivatives of the yield function with respect to the three plane stress components are presented. From the experience of the author, the presented expressions seem to not comply with expressions

obtained through simple symbolic differentiation in MATLAB or other symbolic computer algebra systems and were not able to produce realistic magnitudes of the traverse strain ratios. The obtained expressions for the partial derivatives were validated by using the anisotropy coefficients presented by Reyes et al. [6] for two different aluminium alloys to successfully recreate their associated plots for the traverse strain ratio, R_θ, vs. the angle to the rolling direction, θ.

Using the semi-analytical approach presented in the original article, the described equations are used to identify the three first anisotropy coefficients a, c and p from R_0 and R_{90} alone as

$$a = 2 - c = 2 - 2\sqrt{\frac{R_0}{1+R_0}\frac{R_{90}}{1+R_{90}}}$$

Eq. 3.1-20

$$h = \sqrt{\frac{R_0}{1+R_0}\frac{1+R_{90}}{R_{90}}}$$

The last coefficient of anisotropy, p, is found numerically when the three other coefficients are known. Although a mathematical proof isn't provided, repeated simulations performed at $\theta = 45$ is said to suggest a monotonic relationship between p and the traverse strain ratio, R_θ. Thus, for the Lankford constant, R_{45}, a unique corresponding value of p should exist.

3.1.3 Yld2000-2d

Based on the philosophy of linear transformation-based anisotropic yield criteria, a high exponent anisotropic yield criterion for plane stress states was presented by F. Barlat et al. in 2003 [16]. A formulation which reduces to an isotropic high-exponent yield criterion was used as a framework for the linearly transformed stress tensor. The isotropic criterion by Hershey [2], can be presented as the sum of two terms as

$$\psi = \psi' + \psi'' = 2(\sigma^Y)^M$$

Eq. 3.1-21

where the respective terms are formulated as

$$\psi' = |s_1 - s_2|^M$$
$$\psi'' = |2s_2 + s_1|^M + |2s_1 + s_2|^M \qquad \text{Eq. 3.1-22}$$

where s_i are the principal values of the deviatoric stress tensor $\boldsymbol{s}$ in plane stress.

To address anisotropy, a new function, ϕ, on the same form as ψ is established, where the principle deviatoric stresses in Eq. 3.1-22 are replaced with the principle values of two anisotropic stress states, $\boldsymbol{X}'$ and $\boldsymbol{X}''$, which are obtained through linear transformations on the stress tensors in ψ' and ψ'', respectively. Because the given yield function is independent of hydrostatic stresses, the anisotropic stress state can be formulated as a transformation acting of the stress deviator, $\boldsymbol{s_{ij}}$, just as well as the Cauchy stress tensor, $\boldsymbol{\sigma_{ij}}$. The different mathematical formulations might serve different practical purposes – thus, both are presented followingly.

Using the relationship

$$\{\boldsymbol{s_{ij}}\} = [\boldsymbol{T}]\{\boldsymbol{\sigma}\} \qquad \text{Eq. 3.1-23}$$

where

$$[\boldsymbol{T}] = \begin{bmatrix} 2/3 & -1/3 & 0 \\ -1/3 & 2/3 & 0 \\ 0 & 0 & 1 \end{bmatrix} \qquad \text{Eq. 3.1-24}$$

we get

$$\{\boldsymbol{X'}_{ij}\} = [\boldsymbol{C'}]\{\boldsymbol{s_{ij}}\} = [\boldsymbol{C'}][\boldsymbol{T}]\{\boldsymbol{\sigma_{ij}}\} = [\boldsymbol{L'}]\{\boldsymbol{\sigma_{ij}}\}$$
$$\{\boldsymbol{X''}_{ij}\} = [\boldsymbol{C''}]\{\boldsymbol{s_{ij}}\} = [\boldsymbol{C''}][\boldsymbol{T}]\{\boldsymbol{\sigma_{ij}}\} = [\boldsymbol{L''}]\{\boldsymbol{\sigma_{ij}}\} \qquad \text{Eq. 3.1-25}$$

Assuming a cartesian coordinate system of x and y, respectively aligned with the RD and TD, the two transformations acting on the stress deviator take the forms

$$\begin{Bmatrix} X'_{xx} \\ X'_{yy} \\ X'_{xy} \end{Bmatrix} = \begin{bmatrix} C'_{11} & C'_{12} & 0 \\ C'_{21} & C'_{22} & 0 \\ 0 & 0 & C'_{66} \end{bmatrix} \begin{Bmatrix} s_{xx} \\ s_{yy} \\ s_{xy} \end{Bmatrix}$$

Eq. 3.1-26

$$\begin{Bmatrix} X''_{xx} \\ X''_{yy} \\ X''_{xy} \end{Bmatrix} = \begin{bmatrix} C''_{11} & C''_{12} & 0 \\ C''_{21} & C''_{22} & 0 \\ 0 & 0 & C''_{66} \end{bmatrix} \begin{Bmatrix} s_{xx} \\ s_{yy} \\ s_{xy} \end{Bmatrix}$$

Note that the anisotropic stress states, $\boldsymbol{X'}$ *and* $\boldsymbol{X''}$, (and thus the yield criterion) reduce to the isotropic form when the transformation tensors $\boldsymbol{C'}$ and $\boldsymbol{C''}$ takes the form of the identity matrix, i.e. when $C^{(k)}{}_{11} = C^{(k)}{}_{22} = C^{(k)}{}_{66} = 1$ and $C^{(k)}{}_{12} = C^{(k)}{}_{21} = 0$ for $k = 1$ and 2.

An alternative and equivalent formulation of the linearly transformed stresses $\boldsymbol{X^{(k)}}$ is obtained by performing the two linear transformations on the Cauchy stress tensor, $\boldsymbol{\sigma}$, rather than on the stress deviator, $\boldsymbol{s}$, are formulated as

$$\begin{Bmatrix} X'_{xx} \\ X'_{yy} \\ X'_{xy} \end{Bmatrix} = \begin{bmatrix} L'_{11} & L'_{21} & 0 \\ L'_{21} & L'_{22} & 0 \\ 0 & 0 & L'_{66} \end{bmatrix} \begin{Bmatrix} \sigma_x \\ \sigma_y \\ \tau_{xy} \end{Bmatrix}$$

$$\begin{Bmatrix} X''_{xx} \\ X''_{yy} \\ X''_{xy} \end{Bmatrix} = \begin{bmatrix} L''_{11} & L''_{21} & 0 \\ L''_{21} & L''_{22} & 0 \\ 0 & 0 & L''_{66} \end{bmatrix} \begin{Bmatrix} \sigma_x \\ \sigma_y \\ \tau_{xy} \end{Bmatrix}$$

Eq. 3.1-27

where

$$\begin{Bmatrix} L'_{11} \\ L'_{12} \\ L'_{21} \\ L'_{22} \\ L'_{66} \end{Bmatrix} = [\boldsymbol{C'}][\boldsymbol{T}] = \begin{bmatrix} 2/3 & 0 & 0 \\ -1/3 & 0 & 0 \\ 0 & -1/3 & 0 \\ 0 & 2/3 & 0 \\ 0 & 0 & 1 \end{bmatrix} \begin{Bmatrix} \alpha_1 \\ \alpha_2 \\ \alpha_7 \end{Bmatrix}$$

$$\begin{Bmatrix} L''_{11} \\ L''_{12} \\ L''_{21} \\ L''_{22} \\ L''_{66} \end{Bmatrix} = [\boldsymbol{C''}][\boldsymbol{T}] = \frac{1}{9} \begin{bmatrix} -2 & 2 & 8 & -2 & 0 \\ 1 & -4 & -4 & 4 & 0 \\ 4 & -4 & -4 & 1 & 0 \\ -2 & 8 & 2 & -2 & 0 \\ 0 & 0 & 0 & 0 & 9 \end{bmatrix} \begin{Bmatrix} \alpha_3 \\ \alpha_4 \\ \alpha_5 \\ \alpha_6 \\ \alpha_8 \end{Bmatrix}$$

Eq. 3.1-28

Through the anisotropic stress states, the Yld2000-2d yield criterion allows the material anisotropy to be described in terms of eight independent coefficients, from α_1 to α_8, which must be determined through calibration to experiments, as will be described later in this chapter. The isotropic states of $\boldsymbol{X'}$ and $\boldsymbol{X''}$ are is this in this formulation achieved when these coefficients are all of unity magnitude.

The two principle values of each of the linearly transformed stresses, $\boldsymbol{X'}$ and $\boldsymbol{X''}$ are calculated as

$$X^{(k)}{}_1 = \frac{1}{2}\left(X^{(k)}{}_{xx} + X^{(k)}{}_{yy} + \sqrt{\left(X^{(k)}{}_{xx} - X^{(k)}{}_{yy}\right)^2 + 4\left(X^{(k)}{}_{xy}\right)^2} \right)$$

$$X^{(k)}{}_2 = \frac{1}{2}\left(X^{(k)}{}_{xx} + X^{(k)}{}_{yy} - \sqrt{\left(X^{(k)}{}_{xx} - X^{(k)}{}_{yy}\right)^2 + 4\left(X^{(k)}{}_{xy}\right)^2} \right)$$

Eq. 3.1-29

Finally, the Yld200-2d anisotropic yield criterion, ϕ, is obtained by substituting the principle stress deviators, s_i, by the principle anisotropic values, X'_i and X''_i, into ψ' and ψ'', respectively, to generate the two subfunctions

$$\phi' = |X'_1 - X'_2|^M$$

$$\phi'' = |2X''_2 + X''_1|^M + |2X''_1 + X''_2|^M$$

Eq. 3.1-30

This gives:

$$\phi = \phi' + \phi'' = |X'_1 - X'_2|^M + |2X''_2 + X''_1|^M + |2X''_1 + X''_2|^M = 2(\sigma^Y)^M$$

Eq. 3.1-31

With the correct anisotropy coefficients, Eq. 3.1-31 provides the model's predicted yield stresses with various stress states as input. As eight data points must be provided to determine the eight anisotropy coefficients, experimentally obtained yield stresses at

eight different stress states would have to be obtained to calibrate the unknowns, α_1 to α_8. However, to restrict the number of experiments, expressions describing the predicted directions of strain increments, and thus, strain ratios, R, are obtained by the associated flow rule. With the irreversible nature of plastic strains, the three strain increments are described from the associate flow rule in terms of time increment as

$$\dot{\varepsilon}_{xx} = \dot{\lambda} \cdot \frac{\partial \phi}{\partial \sigma_x}$$

$$\dot{\varepsilon}_{yy} = \dot{\lambda} \cdot \frac{\partial \phi}{\partial \sigma_y} \qquad \text{Eq. 3.1-32}$$

$$\dot{\varepsilon}_{xy} = \dot{\lambda} \cdot \frac{\partial \phi}{\partial \tau_{xy}}$$

where $\dot{\lambda}$ is the proportionality factor.

The derivatives of the yield function with respect to the Cauchy stress tensor, $\boldsymbol{\sigma}$, can be expressed as [47]

$$\frac{\partial \phi^{(k)}}{\partial \sigma_x} = \frac{\partial \phi^{(k)}}{\partial X_{xx}^{(k)}} \cdot L_{11}^{(k)} + \frac{\partial \phi^{(k)}}{\partial X_{yy}^{(k)}} \cdot L_{21}^{(k)}$$

$$\frac{\partial \phi^{(k)}}{\partial \sigma_y} = \frac{\partial \phi^{(k)}}{\partial X_{xx}^{(k)}} \cdot L_{12}^{(k)} + \frac{\partial \phi^{(k)}}{\partial X_{yy}^{(k)}} \cdot L_{22}^{(k)} \qquad \text{Eq. 3.1-33}$$

$$\frac{\partial \phi^{(k)}}{\partial \tau_{xy}} = \frac{\partial \phi^{(k)}}{\partial X_{xy}^{(k)}} \cdot L_{66}^{(k)}$$

where the derivatives of $\phi^{(k)}$ with respect to the linearly transformed stresses $\boldsymbol{X^{(k)}}$ are on the form

$$\frac{\partial \phi^{(k)}}{\partial X_{\alpha\beta}^{(k)}} = \frac{\partial \phi^{(k)}}{\partial X_1^{(k)}} \cdot \frac{\partial X_1^{(k)}}{\partial X_{\alpha\beta}^{(k)}} + \frac{\partial \phi^{(k)}}{\partial X_2^{(k)}} \cdot \frac{\partial X_2^{(k)}}{\partial X_{\alpha\beta}^{(k)}} \qquad \text{Eq. 3.1-34}$$

In these calculations singularities which appear when the principle values of the two linearly transformed stress vectors equal each other must be addressed. Expressions for the terms appearing in the above equation, along with how to handle the singular cases of the derivatives are presented in Appendix A1 in the original paper on Yld2000-2d by Barlat et al. [16], and will not be addressed in detail here.

To determine the values of the eight independent coefficients, α_1 to α_8, which fits the Yld2000-2d criterion to capture the anisotropic yield characteristics of a material, eight data points with information about the modelled materials constitutive behaviour must be provided. In the approach described here, six of these data points are obtained through measurements from the uniaxial tensile test. From tensile test specimens carved at 0°, 45° and 90° to the rolling direction, the yield stresses, σ_0^Y, σ_{45}^Y and σ_{90}^Y, and the Lankford constants, R_0, R_{45} and R_{90} are supplied.

The last two data points required for calibration of the yield function, are the yield stress and strain ratio from biaxial tension in the sheet plane, respectively denoted as σ_b^Y and R_b. The biaxial yield stress, σ_b^Y, is typically obtained by performing a bulge test, where a clamped circular freestanding part of the sheet metal is subjected to a pressurized fluid on one side, while the resulting bulge on the opposite side is monitored [48].

As suggested by Barlat et al., the equibiaxial strain ratio can be determined using three different approaches. One approach is to acquire knowledge of the materials crystallographic texture, and then to calculate the value based on a polycrystal model. Another method is to calculate the value based on another yield function which does not require the biaxial strain ratio as input for calibration. The third suggested approach is to obtain R_b is by measuring it experimentally from a disc compression test as described by Barlat in the original article.

3.1.4 Yld2003

With the relatively complicated mathematical form of the Yld2000-2d, a new yield function – clearly inspired by the work of Barlat – surfaced in the 2004 article by Holger Artez [17]. The yield function Yld2003 is, like its older brother, based on an eight-term

modification to the high exponent plane stress Hershey yield function in order to add anisotropic characteristics to the function.

What makes Yld2003 interesting is its simple mathematical form. With a similar approach as in Yld2000-2d, the Hershey yield function in terms of its principle components is divided into two separate functions, where the stress configurations in each of the functions are individually linearly transformed to establish enhanced flexibility when the function is to be fitted to experimental measurements. However, while the Yld2000-2d function uses rather complicated matrix transformations on the stress deviator to obtain the linearly transformed stresses, Aretz uses a simpler approach inspired by the Yld89 yield function [5] where the Cartesian stress tensor components are simply scaled in the expressions for the principal stresses.

In plane stress, the Hershey yield function in terms of its principle stresses takes the form:

$$|\sigma_1|^M + |\sigma_2|^M + |\sigma_1 - \sigma_2|^M = 2(\sigma^Y)^M \qquad \text{Eq. 3.1-35}$$

The standard formula for stress transformations from the frame of reference of a Cartesian coordinate system to the principle stress frame is

$$\left.\begin{matrix}\sigma_1 \\ \sigma_2\end{matrix}\right\} = \frac{\sigma_x + \sigma_y}{2} \pm \sqrt{\left(\frac{\sigma_x - \sigma_y}{2}\right)^2 + {\tau_{xy}}^2} \qquad \text{Eq. 3.1-36}$$

The Hershey yield function is divided into two, where the first and second absolute terms are subjected to a transformation from five of the eight anisotropy coefficients a_1 to a_8, so that $\sigma_1 \rightarrow {\sigma'}_1$ and $\sigma_2 \rightarrow {\sigma'}_2$:

$$\left.\begin{matrix}{\sigma'}_1 \\ {\sigma'}_2\end{matrix}\right\} = \frac{a_8 \cdot \sigma_x + a_1 \cdot \sigma_y}{2} \pm \sqrt{\left(\frac{a_2 \cdot \sigma_x - a_3 \cdot \sigma_y}{2}\right)^2 + {a_4}^2 \cdot {\tau_{xy}}^2} \qquad \text{Eq. 3.1-37}$$

Next, the last absolute term of the plane stress Hershey yield function is subjected to a resembling transformation from the remaining anisotropy terms, a_5, a_6 and a_7, so that $\sigma_1 \rightarrow {\sigma''}_1$ and $\sigma_2 \rightarrow {\sigma''}_2$:

$$\left.\begin{matrix}\sigma''_1\\ \sigma''_2\end{matrix}\right\} = \frac{\sigma_x + \sigma_y}{2} \pm \sqrt{\left(\frac{a_5 \cdot \sigma_x - a_6 \cdot \sigma_y}{2}\right)^2 + {a_7}^2 \cdot {\tau_{xy}}^2} \qquad \text{Eq. 3.1-38}$$

Reconstructing the yield function on the form of the Hershey function, the relatively simple eight-term anisotropic yield function Yld2003 takes the form:

$$|\sigma'_1|^M + |\sigma'_2|^M + |\sigma''_1 - \sigma''_2|^M = 2(\sigma^Y)^M \qquad \text{Eq. 3.1-39}$$

In the special case when all anisotropy coefficients a_1 to a_8 are taken as unity, and the exponent of the function is taken as M = 2, the Yld2003 yield function reduces to the Von Mises' yield criterion for plane stress.

The function is suggested fitted to the eight experimental datapoints in a minimized sum of squared errors-fashion (see *Ch. 4.2.1*) to obtain the eight anisotropy coefficients. In the original article, flow-stress ratios, $r_{\theta,}$ and traverse strain ratios, R_θ, form uniaxial tensile tests with longitudinal direction inclined at $\theta = 0°$, 45° and 90° to a metal sheet's rolling direction made of six of the data points, while the last two were the corresponding quantities taken from equibiaxial tests, r_b and R_b.

As with the previously presented yield functions, the associate flow rule is used along with the constant volume assumption to express the model's predicted traverse strain ratios, R_θ, as derivatives of the yield function.

The same arguments as was used to defend the convexity of the Yld2000-2d function can be used for the above function. By performing a simple linear transformation on the input of a function which is isotropic to its input, convexity is safely maintained.

From the understanding of the author, a drawback with Yld2003 by Aretz to its predecessor in the Yld2000-2d is that singularities of the yield function are not addressed in the original article. In work with the current thesis, an attempt to analytically calculate the derivatives of the yield function in the equibiaxial states of the transformed stress tensors was made. For the Yld2000-2d yield function, these configurations are known to be singular cases and thus the function is undefined in these points. The calculations

showed that singularities were seemingly found in the Yld2003 function as well, for stress configurations fulfilling these conditions. Without mentioning the matter, a numerical differentiation by a forward difference scheme is suggested in the article by Aretz, which is likely to avoid these special cases in the calibration.

3.2 Hardening

As the longitudinal stresses and strains equal the effective stresses and strains in a uniaxial tensile test, the uniaxial tensile test directly describes the relationship of effective stresses, σ_e, to effective plastic strains, ε_e^p. However, because uniaxial tensile specimens' experiences diffuse necking which leads to expedited rupture, a hardening model which extrapolates a material's observed constitutive behaviour to strains beyond the strain-domain of the uniaxial tensile test is needed when FEA-simulations of other geometries and load cases are to be conducted.

Regardless of whether the hardening of the material is isotropic or kinematic, several functions of the equivalent plastic strains are used to describe the work hardening of ductile materials. One of the most established hardening rules for metals is the Power law, which is through a hardening coefficient, K, and a hardening exponent, n, written on the following form:

$$\sigma_e = K\left(\varepsilon_e^p\right)^n \qquad \text{Eq. 3.2-1}$$

While the Power law predicts zero stress at zero plastic strains, a modification to the Power law – often referred to as the Swift law or the Ludwik's – is equivalent but with an additional yield stress term, σ_0.

$$\sigma_e = \sigma_0 + K\left(\varepsilon_e^p\right)^n \qquad \text{Eq. 3.2-2}$$

Another group of work hardening formulas which are popularly used to describe the hardening of aluminium alloys is the Voce rule. In addition to a yield stress term, the equation comes with a desired number of additional terms, each term containing two

parameters, giving increased flexibility to accurately fit the curve to the experimental data. The one- and two-term Voce rule takes the following form:

$$\sigma_e = \sigma_0 + Q_R\left(1 - exp\left(-\frac{\Theta_R}{Q_R}\varepsilon_e^p\right)\right) \quad \text{Eq. 3.2-3}$$

$$\sigma_e = \sigma_0 + Q_{R1}\left(1 - exp\left(-\frac{\Theta_{R1}}{Q_{R1}}\varepsilon_e^p\right)\right) + Q_{R2}\left(1 - exp\left(-\frac{\Theta_{R2}}{Q_{R2}}\varepsilon_e^p\right)\right) \quad \text{Eq. 3.2-4}$$

Comparing the Ludwik's law to the one-term Voce rule – both containing two hardening variables, in addition to the yield stress at zero plastic strains – the Voce curve typically produces a more moderate hardening evolution for higher plastic strains than the other.

3.3 Local necking, fracture and damage

3.3.1 Non-local instability-criterion (NLIC)

When comparing different meshes in finite element simulations, the localization of strains as described in the theory chapter on forming limits seems to occur almost randomly. By monitoring the state of a material at a larger surrounding area, non-local failure theories are successfully used to tackle this issue by reducing the mesh size sensitivity on failure, and thus greatly enhancing the prediction of onset of local necking instabilities [49].

The typical approach to the non-local criteria is to define an area of interest where an average of a quantity at the integration points within that area is used as a non-local reference value. In the non-local instability criterion (NLIC) localisations of plastic strain in the through-thickness direction of the sheet, ε_z^p, is under investigation. By monitoring the ratio of the increments of local to non-local values of the quantity, local necking instabilities – which Marciniak and Kuczynski [4] proved that naturally will occur when inducing inhomogeneities in the strength of the material – can be detected.

If R_Ω is a user-defined radius, Ω_{el} is the area made up of elements with at least one integration point within the circle defined by R_Ω. The relationship between the local and the non-local quantity is calculated stepwise for every element throughout the analysis as

$$\beta_i = \frac{\Delta\varepsilon_z^{p(i)}}{\Delta\varepsilon_z^{p,\Omega_{el}}} \qquad \text{Eq. 3.3-1}$$

In some cases, a weighting of different elements' contribution to the non-local value, $\Delta\varepsilon_z^{p,\Omega_{el}}$, based on their distance to the local element, might be desirable. However, when all elements within the considered radius are treated fairly the non-local value of the through-thickness plastic strain increment is defined as

$$\Delta\varepsilon_z^{p,\Omega_{el}} = \frac{1}{\Omega_{el}} \int_{\Omega_{el}} \Delta\varepsilon_z^p \, d\Omega_{el} \quad , \qquad \text{Eq. 3.3-2}$$

or when the radius, R_Ω, is defined as large enough to cover the entire model:

$$\Delta\varepsilon_z^{p\Omega_{el}} = \frac{1}{n_{el}} \sum_{i=1}^{n_{el}} \Delta\varepsilon_z^{p(i)} \qquad \text{Eq. 3.3-3}$$

where n_{el} is the number of elements in the entire model.

Local necking is assumed to occur when the ratio of local to non-local through-thickness strain increments exceeds a critical value, β_{cr}.

3.3.2 Non-local extremal thickness strains deviation-criterion (NLETSDC)

Although the finite element program LS-DYNA provides the possibility to detect localized necking instabilities from NLIC through the *NONLOCAL*-keyword [49], the history variable which describes the relationship between the local and non-local through-thickness strain increment, β_i, was seemingly not produced as output from the analysis as requested. Thus, a simple alternative method tailored to detect the onset of local necking from the available history variables was established as a replacement.

The method resembles the non-local instability criterion in that the through-thickness plastic strains, ε_z^p, are monitored at all locations throughout the analysis of a model which has initial spatially distributed weaknesses. Within a considered area, the minimum and the maximum of all values of $\varepsilon_z^{p(i)}$ was monitored. From this the relationship of the two quantities, a history variable was established as

$$\xi_i = \frac{\varepsilon_z^{p,\Omega_{max}}}{\varepsilon_z^{p,\Omega_{min}}} \qquad \text{Eq. 3.3-4}$$

The onset of local necking is assumed to occur when the history variable ξ_i reaches a critical value, ξ_{cr}.

To validate the NLESD-criterion in the current analyses, care was taken to make sure that the minimal value of the through-thickness plastic strain was of magnitude comparable to the magnitude of a reasonable chunk of the other values at the same instance. Additionally, visual inspections were made of the effective plastic strain field plots to assure that ξ_i reached the critical value around the time when strain localization occurred. Lastly, a sensitivity analysis of the critical value, ξ_{cr}, was conducted. The result revealed that the discrepancy between the forming limit curves produced with $\xi_{cr} = 2$ and with $\xi_{cr} = 1.5$ was negligible.

3.3.3 Through-thickness shear instability criterion (TTSIC)

The through-thickness shear instability criterion (TTSIC) for sheet metal forming was first introduced by Bressan and Williams in 1982 [7]. Up until then, several different criteria had been introduced which suggested that shear instability was the underlying common feature in many of them. Supported by the experimental observation that sheet metals often exhibited fracture planes with inclination near 45°, which is the maximum shear stress plane.

Assuming that elastic strains are of negligible magnitude compared to plastic strains at the occurrence of local necking, necking instability is assumed to occur when the shear stress on a plane where an element of material is subjected to no straining in length

reaches a critical value, τ_{cr}. The original formulation was initially developed for metal sheets which exhibited normal anisotropy where the directions of stresses and plastic strains in the principle frame of reference are coinciding. From this, the following equation to calculate the inclination, φ, from the critical plane based on plastic strain increments is used, with the established coordinate system of x, y and z respectively aligned with the rolling, traverse and through-thickness directions:

$$\cos 2\varphi = -\frac{d\varepsilon_y^p}{d\varepsilon_y^p + 2d\varepsilon_x^p} \qquad \text{Eq. 3.3-5}$$

For materials which exhibit orthotropic anisotropy principal stresses and principal plastic strains are generally not aligned unless the principal axis of stress coincides with the principal axis of anisotropy. In that case, the following relationship was according to Reyes et al. [6] presented by Hopperstad et al. in a 2006 report, and later confirmed by Brunet and Clerc [50]:

$$\begin{aligned}(sin^2\varphi\, cos^2\theta - cos^2\varphi)\, d\varepsilon_y^p + sin^2\varphi \cos\theta \sin\theta\, d\gamma_{xy}^p \\ + (sin^2\varphi\, sin^2\theta - cos^2\varphi)\, d\varepsilon_y^p = 0\end{aligned} \qquad \text{Eq. 3.3-6}$$

The above equation reduces to the Eq. 3.3-5 presented by Bressan and Williams when the angle between the rolling direction and the major principle stress, θ, is zero.

From this, the TTSIC is satisfied when the shear stress on the critical plane, τ_φ, reaches a critical value, τ_{cr}.

$$\tau_\varphi = \frac{\sin(2\varphi)}{2}\sigma_1 \geq \tau_{cr} \qquad \text{Eq. 3.3-7}$$

With this, the assumption of τ_{cr} as an isotropic value in an orthotropic must be considered if is justifiable to the assessed material. In the mentioned article by Reyes et al. [6] the assumption is justified for the two materials in the study (AA2008-T4 and AA6111-T4), based on their moderate planar anisotropic characteristics.

3.3.4 Original Cockcroft-Latham fracture criterion (OCLFC)

Fracture because of strain localisations from local necking instability is perhaps the primary phenomenon which causes rupture in aluminium sheet forming. As the presence of local necks is unwanted in metal sheet forming products, the necking strains are often what constrains the forming limit curve. However, rupture from ductile damage from void nucleation, growth and coalescence as described in *Ch. 2.3.2* can occur without the preliminary local neck, and thus a criterion describing fracture is sometimes required implemented into FEA-code to successfully describe the behaviour of the material.

Introduced by Cockcroft and Latham in 1968 [9], the ductile fracture criterion is assumed to be satisfied when a critical amount of plastic work performed by positive values to the major principal stress is reached. Thus, unlike the previously introduces local necking criteria, which were only reliant on the current state of strains or stresses in a material, the Cockcroft-Latham fracture criterion considers the loading history.

As several modifications to the Cockcroft-Latham fracture criterion exists, the expression presented in the following equation will be referred to as the original Cockcroft-Latham fracture criterion (OCLFC). The plastic work from the positive values of the major principal stress is formulated as

$$W_1 = \int_0^{\bar{\varepsilon}} \max(\sigma_1, 0) d\bar{\varepsilon} \geq W_{cr} \qquad \text{Eq. 3.3-8}$$

where $\bar{\varepsilon}$ is the accumulated plastic strain, and W_{cr} is a material constant which can be adjusted to observations from experiments where strain localization is controlled.

In the work of Dimitry Vysochinskiy [10], two different plane strain tension tests specimen geometries with three parallels each were used to calculate the OCLFC. Although the fracture was reportedly provoked by strain concentrations around the notched, relatively large scatters were seen in the six measured values of W_{cr}. Averaging over the path, the critical plastic work of AA6016-T4 was calculated by Vysochinskiy to 211.5 MPa.

3.3.5 Generalized incremental stress state dependent damage model (GISSMO)

The non-local instability criteria, along with the through-thickness shear instability criterion and the original Cockcroft-Latham criterion for ductile fracture were presented as so-called uncoupled damage models. The criteria are either limits to a current state, or an accumulation of quantity, which eventually classifies the material as damaged or "necked" instantaneously, and the stress state in material points fulfilling these criteria are is set to zero. In reality, extensive plastic stains are associated with some form of damage which reduces the stiffness of the strained material.

The purpose of damage coupling is to establish a mathematical phenomenological model describing the onset of damage, the accumulation of damage and its effect on the constitutive description of the material, up until the occurrence of failure. To provide an understanding of modern damage coupling model models, an example, in the generalizes incremental stress state dependent damage model (GISSMO), is detailed described in the following.

The damage model – recently introduced by Andrade et al. in 2015 [18] can be viewed as a general version of the classical principle of effective stress described by Lemaitre in 1985 [51] enabling enhanced flexibility by allowing a more accurate description of material damage for relatively coarser meshes in FEA-simulations.

The critical strains, ε_{cr}, which determines the onset of damage accumulation, as well as the strains at the occurrence of fracture, $\varepsilon_f(\eta)$, is dependent on the stress state, or more specifically the stress triaxiality, η. Thus, we have

$$\varepsilon_{cr} = \varepsilon_{cr}(\eta) \qquad \text{Eq. 3.3-9}$$

and

$$\varepsilon_f = \varepsilon_f(\eta) \qquad \text{Eq. 3.3-10}$$

where the stress triaxiality is the ratio of hydrostatic pressure to effective von Mises stresses

$$\eta = \frac{\sigma_m}{\sigma_e} \qquad \text{Eq. 3.3-11}$$

The generalizes incremental stress state dependent damage model (GISSMO) does not define the shape of the functions $\varepsilon_{crit}(\eta)$ and $\varepsilon_f(\eta)$, and is thus compatible with the multiple various functions found in the literature to describe these curves.

An instability variable, which activates the accumulation of damage when it reaches unity, i.e. when $\varepsilon^p = \varepsilon_{crit}(\eta)$, is formulated as

$$F = \left(\frac{\varepsilon^p}{\varepsilon_{crit}(\eta)}\right)^n \leq 1 \qquad \text{Eq. 3.3-12}$$

where n is a damage exponent. when the instability variable, F, reaches the value of 1, the accumulation of damage begins. To express the growth of the instability variable as a sum of increments, its derivative with respect to time assuming constant triaxiality is

$$\dot{F} = \frac{n}{\varepsilon_{crit}(\eta)} F^{(1-1/n)} \dot{\varepsilon}^p \qquad \text{Eq. 3.3-13}$$

With the aim to establish a description of the damage evolution, a damage variable on the same form as the instability variable is written as

$$D = \left(\frac{\varepsilon^p}{\varepsilon_f(\eta)}\right)^n \qquad \text{Eq. 3.3-14}$$

where $\varepsilon_f(\eta)$ are the strains at fracture, presented in Eq. 3.3-10 as a function of the triaxiality. Again, assuming constant triaxiality, D is differentiated with respect to time to be

$$\dot{D} = \frac{n}{\varepsilon_f(\eta)} D^{(1-1/n)} \dot{\varepsilon}^p \qquad \text{Eq. 3.3-15}$$

A function representing the damage which takes place at strain localization, $\widetilde{D}$, can then be written as a function of the damage variable. If $F = 1$,

$$\widetilde{D} = \left(\frac{D - D_{cr}}{1 - D_{cr}}\right)^{m} \quad \text{Eq. 3.3-16}$$

where the D_{cr} is the value of D when F reaches 1, while m is the fading exponent which allows for a non-linear evolution of $\widetilde{D}$. While the general damage variable, D, starts accumulating at the onset of plastic deformations, $\widetilde{D}$ represents the damage evolution which is present after the criterion indicating strain localization is satisfied. Thus, for plastic strains which gives $F < 1$, $\widetilde{D}$ is zero.

The current value of $\widetilde{D}$ directly influences the stress tensor as followingly

$$\boldsymbol{\sigma_{ij}} = \left(1 - \widetilde{D}\right)\widetilde{\boldsymbol{\sigma_{ij}}} \quad \text{Eq. 3.3-17}$$

where $\widetilde{\boldsymbol{\sigma}}$ is the undamaged stress tensor.

By substituting Eq. 3.3-16 into Eq. 3.3-17 the effects of the damage variable on the stress tensor becomes evident

$$\boldsymbol{\sigma_{ij}} = \widetilde{\boldsymbol{\sigma_{ij}}}\left[1 - \left(\frac{D - D_{cr}}{1 - D_{cr}}\right)^{m}\right] \quad \text{Eq. 3.3-18}$$

The model reduces to the Lemaitre-formulation when D_{cr} is set to zero, and the fading exponent m is set to unity.

3.4 Roping model

To attempt to model the effects of roping which was reportedly observed in the AA6016-T4 sheets subject to tests in the experimental program by Dimitry Vysochinskiy [10], an approach to this is followingly presented.

In the FEA-based software LS-DYNA, a pre-programmed module to model perturbations to the thickness of shells as one or more harmonic waves exists in the keyword **PERTURBATION_SHELL_THICKNESS*. The keyword allows the user to specify the amplitude, wavelength and periodic offset of waves though the variables AMPL, WL and OFF, respectively. For a shell element with normal direction aligned with the z-direction, the perturbation field of a single harmonic wave takes on the formulation [49]

$$p(x,y) = AMPL\left[sin\left(2\pi\frac{x+XOFF}{XWL}\right) + sin\left(2\pi\frac{y+YOFF}{YWL}\right)\right] \quad \text{Eq. 3.3-19}$$

With this, thickness perturbations due to roping can be modelled to satisfying accuracy by adding multiple harmonic perturbations which add together to approximate a measured thickness distribution.

$$p(x,y) = \sum_{i=1}^{n}\left(AMPL_i\left[sin\left(2\pi\frac{x+XOFF_i}{XWL_i}\right) + sin\left(2\pi\frac{y+YOFF_i}{YWL_i}\right)\right]\right) \quad \text{Eq. 3.3-20}$$

The approach is closely related to the approximation by Fourier series, except the presence of the phase constant, and the missing presence of an intercept term [52].

As roping is reported to the manifestation of the orientation of grain's spatial distribution in the sheets' through-thickness direction [53], the effects which can be observed with analogue measurements in terms of thickness perturbations can be assumed to be accompanied with variation in material characteristics. Thus, naive of information about this variation, the modelled thickness perturbation could be scaled to obtain good correlation between the anisotropy predicted by the FE-model's and the strain limits observed in the experimental results. In the MK-model, the fundamental assumption is that a band a material which is somehow weaker than the rest. This weakness is often thought of and modelled as a reduction in the thickness of the material. When performing the analysis, the magnitude of the imperfection is typically calibrated to match experimental observations. In the same way, a larger thickness variation that what is physically observed can be justified to account for reduced stiffness from spatial variations in material characteristic.

4 Calibration

4.1 Experimental program by Dimitry Vysochinskiy

The material models presented in this thesis are calibrated to measurements obtained in the experimental programme of Dimitry Vysochinskiy [10], where several experiments were conducted to gain knowledge about the formability of the AA6016-T4 aluminium alloy. The measurements were presented in his 2014 thesis for the degree of Ph. D., while the experiments were conducted in February and March of 2012.

On specimens carved from the AA6016-T4 aluminium alloy sheets, uniaxial tensile tests and disc compression tests were conducted to calibrate the advanced triaxial yield criterion Yld2004-18p by F. Barlat [11]. Marciniak-Kuczynski (MK)-tests and Nakajima (NK) tests were performed, and an experimental forming limit diagram was presented from the results of the MK-tests. Additionally, plane strain tension tests were performed on specimens with two different geometries, referred to as PSTv60 and PSTv50. The numbers of parallels performed for each test are presented in Table 4-1.

Table 4-1: Number of parallels in the test programme of Dimitry Vysochinskiy [10].

Test Type	Specimen orientation							
	0°	15°	30°	45°	60°	75°	90°	Total
Uniaxial tension (UT)	*4*	*2*	*2*	*2*	*2*	*2*	*3*	*17*
Disc compression (DK)	*12*	-	-	-	-	-	-	*12*
Plane strain tension (PSTv60)	*3*	-	*2*	*2*	-	-	*2*	*9*
Plane strain tension (PSTv50)	*3*	-	-	*2*	-	-	*2*	*7*
Marciniak-Kuczynski (MK)	*10*	-	-	-	-	-	*6*	*16*
Nakajima (NK)	*13*	-	-	-	-	-	*9*	*22*

Other experiments, such as in-plane shear tests and cyclic shear tests, in addition to experiments on AA6016-T4 aluminium alloy sheets pre-strained by rolling, are also

presented in the work of Dimitry Vysochinskiy [10]. The material discussed in this thesis is labelled as material ID 6, while pre-strained sheets are referred to as material ID 7.

4.1.1 Uniaxial tensile tests

Uniaxial tensile tests were performed with intervals of 15 degrees angle between the longitudinal axes and the rolling direction. The number of parallels performed at each angle is viewed in Table 4-1.

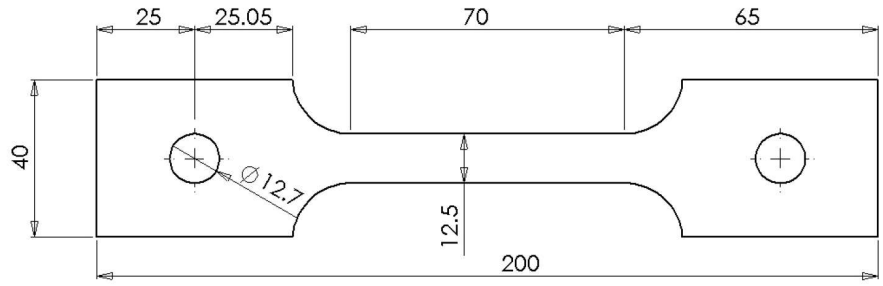

Figure 4-1: Geometry of the SIMLab UT200 uniaxial tensile test specimen. Figure rendered with permission from the PhD-thesis of Dimitry Vysochinskiy [10].

Unlike for the other experimental measurements where the results are simply rendered as presented in the thesis of Dimitry Vysochinskiy, the results from the uniaxial tensile tests are calculated and displayed by the author based on raw test data provided by Vysochinskiy. The test data was obtained through digital image correlation (DIC). By monitoring the displacements of two points through a sequence of digital images the strain evolution is mapped for the history of the experiment. The virtual extensometer-method, which is performed in both the length- and the width-direction of the specimen, is described in detail by Vysochinskiy in his PhD-thesis [10].

Fig. 4-2 displays the work diagrams from the different uniaxial tensile tests. In addition to plots of nominal stresses vs. nominal strains taken directly from the raw data supplied by Vysochinskiy, plots of true stresses vs. true strains are calculated and plotted. The constant volume assumption to express the logarithmic thickness strains from the strains

in the logarithmic strains in the length- and width-directions. From this, the true stresses were calculated as the force, F, divided by the current area, A, and the logarithmic strains were calculated as $\varepsilon = ln(A_o/A)$, according to the equations presented in *Ch. 2.2.5*. By using the logarithmic relationship of the initial area to the current area, the true diagrams are assumed to be valid beyond strains corresponding to the onset of diffuse necking. Both the nominal and the true diagrams are plotted up until the point of ultimate true stress. The reference system for the individual test uniaxial tensile test specimens is on the form $UT\theta - \#$, where θ is the specimen's orientation to the sheets rolling direction, and # indicates the parallel number. All parallels are plotted for each direction.

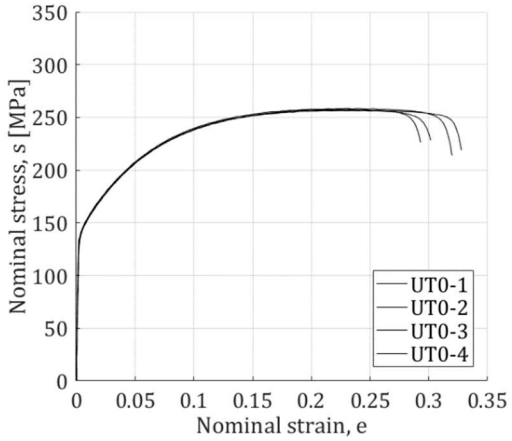

a.i)

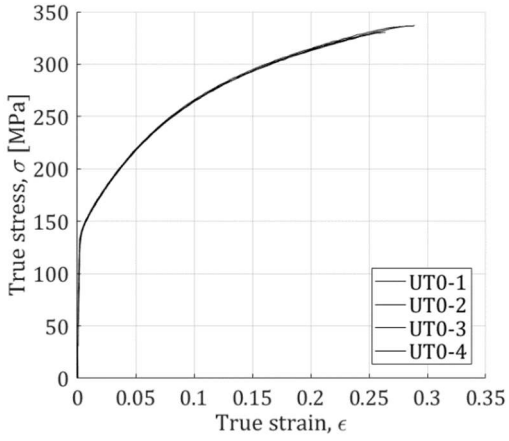

a.ii)

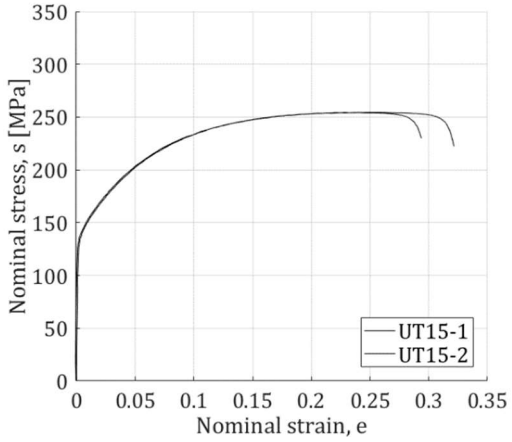

b.i)

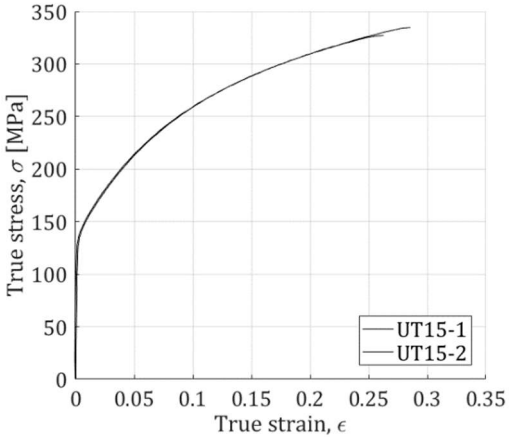

b.ii)

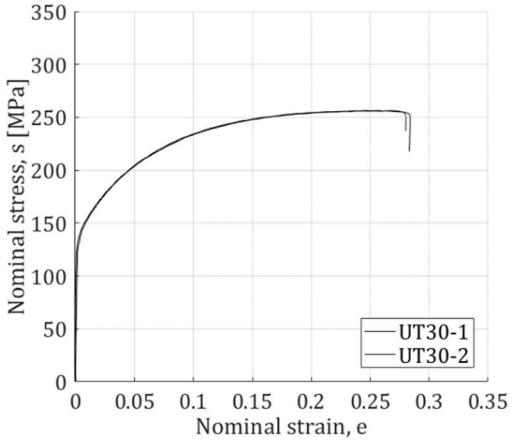

c.i)

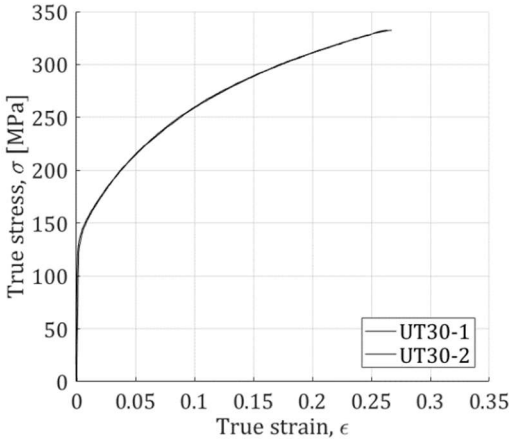

c.ii)

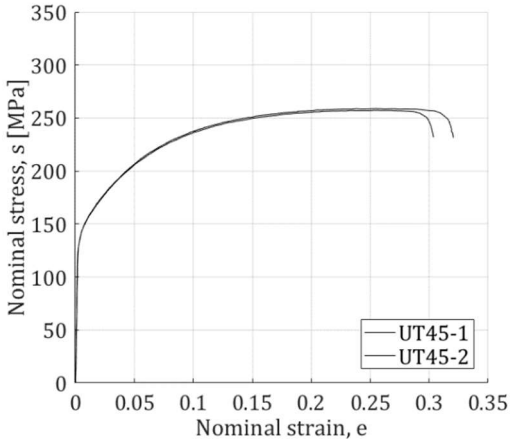

d.i)

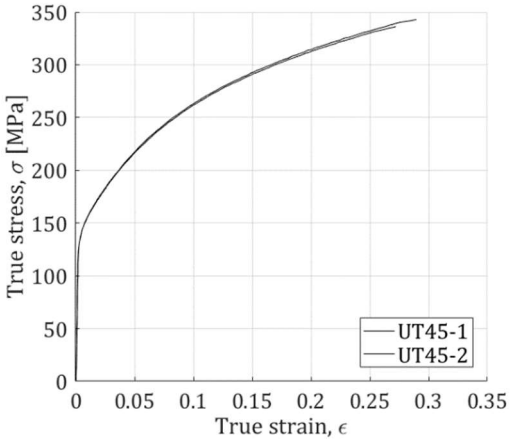

d.ii)

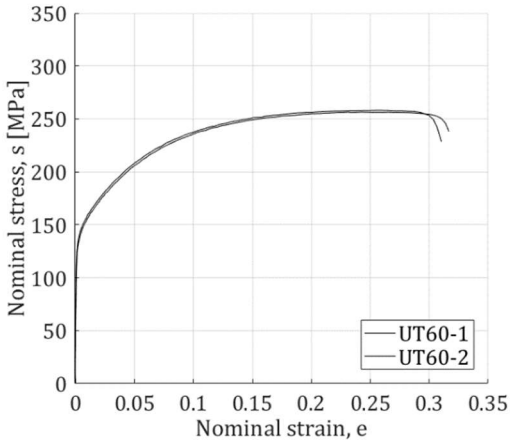

e.i)

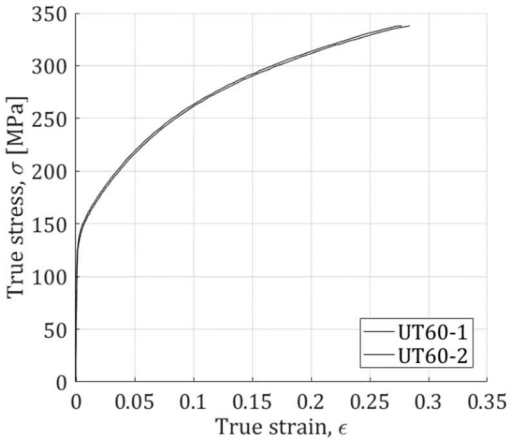

e.ii)

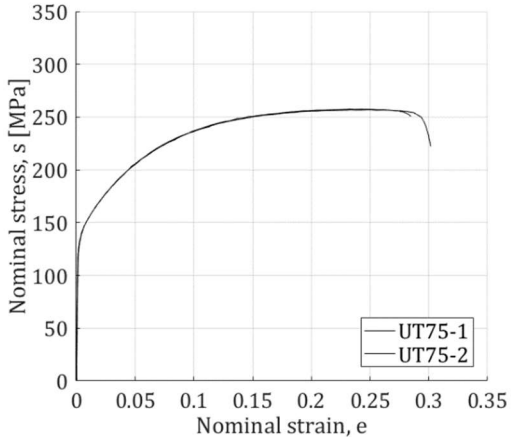

f.i)

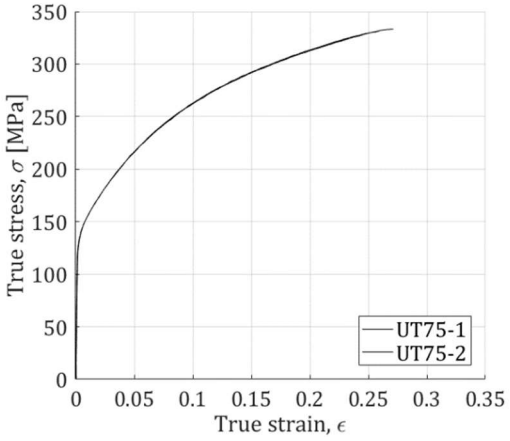

f.ii)

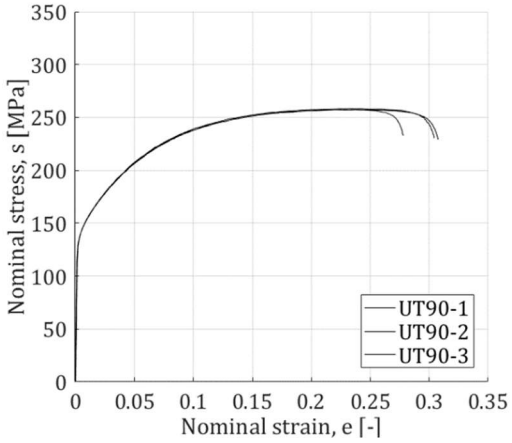

g.i)

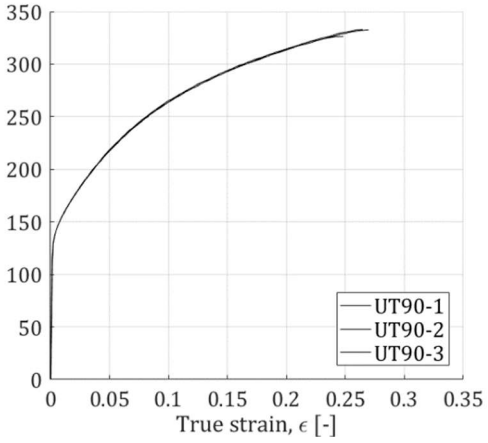

g.ii)

Figure 4-2: Engineering (i) and true (ii) stress-strain diagrams from uniaxial tensile tests from the experimental program by Dimitry Vysochinskiy [10]. *The uniaxial tensile tests are sampled with longitudinal directions at 15 different angles to the sheets rolling direction.*

Although the traverse strain ratios are usually unchanged and relatively stable throughout the plastic evolution, the convention of calculating Lankford coefficients from quantities captured at an elongation of 20% is usually practised for the sake of comparison [54]. With the virtual extensometer data available, the evolutions of the Lankford constants were nevertheless plotted for the sake of curiosity and is displayed in Fig. 4-3 with the engineering strains in the specimen's length-direction plotted on the abscissa.

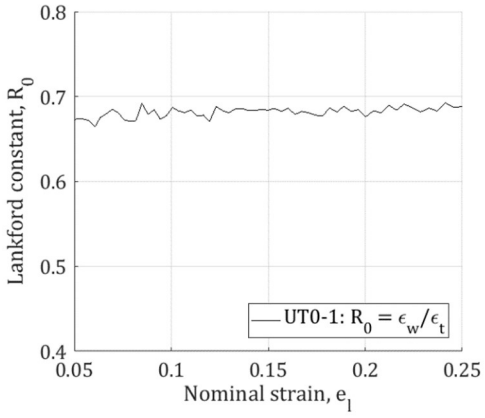

Figure 4-3: Evolution of the Lankford constant as a function of nominal strains in the length direction of specimen UT0-1.

Table 3-2: Traverse strain ratios calculated at 20 % elongation based on experimental data provided by D. Vysochinskiy.

Parallel	R_0	R_{15}	R_{30}	R_{45}	R_{60}	R_{75}	R_{90}
1	*0.677*	*0.580*	*0.440*	*0.412*	*0.497*	*0.785*	*1.056*
2	*0.626*	*0.577*	*0.429*	*0.437*	*0.529*	*0.529*	*1.037*
3	*0.730*	-	-	-	-	-	*0.988*
4	*0.719*	-	-	-	-	-	-

As discrepancies between the values presented by Vysochinskiy and the calculated Lankford constants were discovered, the true strains in the width-direction, ε_w, vs. the true strains in the thickness-direction, ε_t, were plotted to compare the two values for the same quantity. The plots in Fig. 4-5 shows the width- vs. thickness-strains for parallel tensile test, along with the constant ratio calculated from the arithmetic means of the tests, captured at 20% elongation, and the equivalent quantities as presented in the thesis of Vysochinskiy. It is observed that the values previously presented by Vysochinskiy – illustrated by the slope of the plotted lines – are consequently lower than the observed values for an unknown reason. As the values calculated from the arithmetic average at 20% elongation seemingly coincided better with the experimental data for the entire range of the analysis, the material models in this study were calibrated to this data.

Table 4-3: Average of traverse strain ratios calculated at 20 % elongation based on experimental data provided by D. Vysochinskiy, and

	R_0	R_{15}	R_{30}	R_{45}	R_{60}	R_{75}	R_{90}
Av. 20% elong.	*0.688*	*0.579*	*0.435*	*0.425*	*0.513*	*0.753*	*1.030*
Vysochinskiy	*0.527*	*0.516*	*0.355*	*0.345*	*0.422*	*0.644*	*0.867*

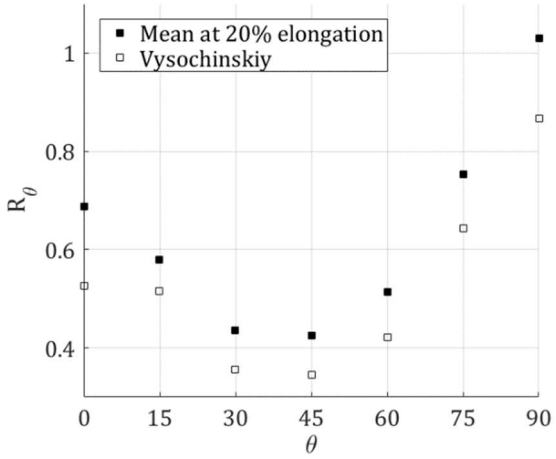

Figure 4-4: Lankford constants calculated at 20% elongation from experimental data provided by Dimitry Vysochinskiy, compared to the calculated values presented by Vysochinskiy [10].

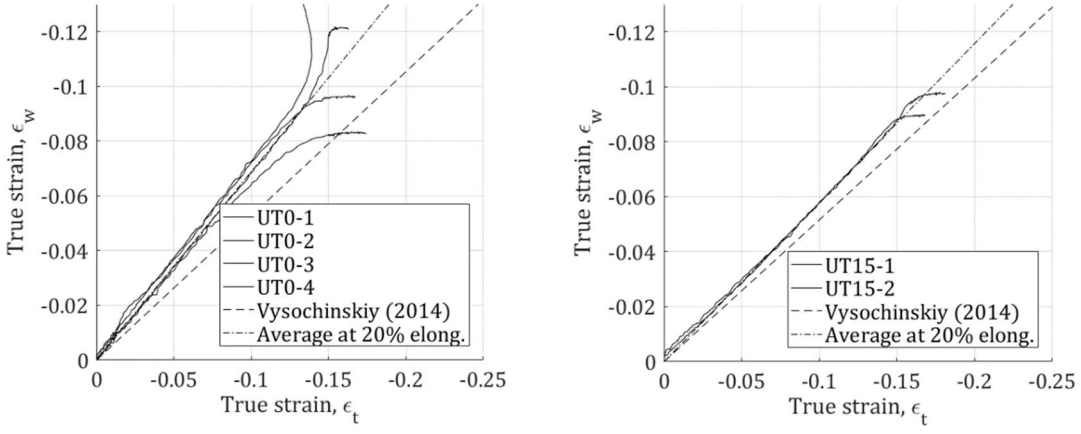

a) *b)*

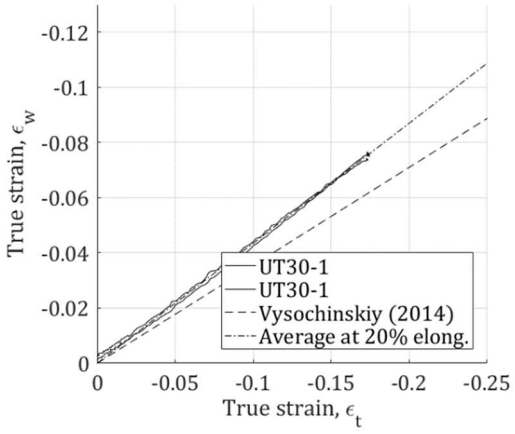

c)

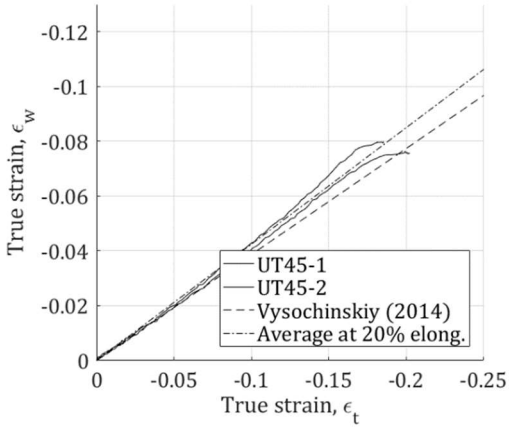

d)

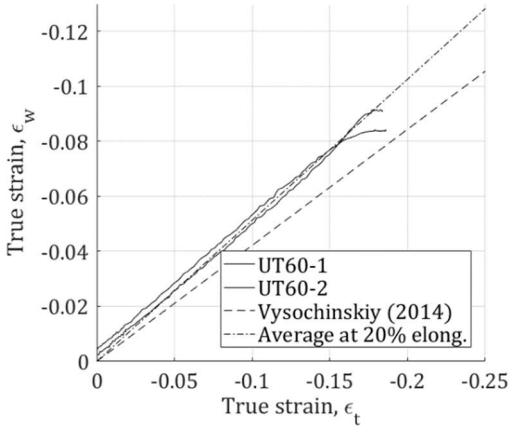

e)

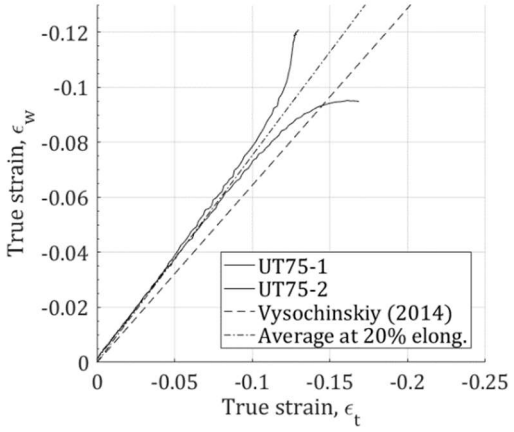

f)

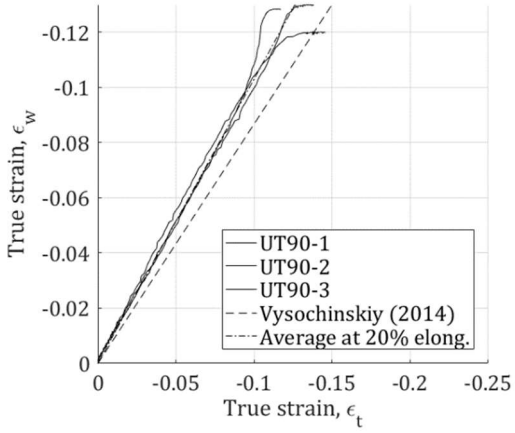

g)

Figure 4-5: Relationships of traverse strains from measurements, compared to the values calculated by Vysochinskiy [10]*, and the average at 20% calculated by the author.*

4.1.2 Marciniak-Kuczynski tests

Table 4-4: Experimental necking strains, fracture strains and crack orientations relative to RD as presented in the Ph.D.-thesis by Vysochinskiy [10].

Sample	Crack orientation to RD	Necking strains		Fracture strains	
		$\boldsymbol{\varepsilon_{RD}}$	$\boldsymbol{\varepsilon_{TD}}$	$\boldsymbol{\varepsilon_{RD}}$	$\boldsymbol{\varepsilon_{TD}}$
MK155-0-1	⊥	*0.2499*	*0.0356*	*0.3215*	*0.0417*
MK155-0-2	⊥	*0.2683*	*0.0409*	*0.3690*	*0.0431*
MK155-90-1	‖	*0.0201*	*0.1426*	*0.0236*	*0.2840*
MK155-90-2	‖	*0.0228*	*0.1524*	*0.0241*	*0.2981*
MK160-0-1	⊥	*0.2778*	*0.0894*	*0.4180*	*0.1320*
MK160-0-2	⊥	*0.2856*	*0.0936*	*0.3980*	*0.1320*
MK160-90-1	‖	*0.0409*	*0.1418*	*0.0605*	*0.3130*
MK160-90-2	‖	*0.0391*	*0.1376*	*0.0542*	*0.2870*
MK165-0-1	‖	*0.2523*	*0.1477*	*0.2800*	*0.2220*
MK165-0-2	‖	*0.2772*	*0.1664*	*0.3240*	*0.2570*
MK165-90-1	‖	*0.0911*	*0.1768*	*0.1200*	*0.2970*
MK165-90-2	‖	*0.0737*	*0.1485*	*0.1033*	*0.2470*
MK205-1	‖	*0.1930*	*0.1728*	*0.2830*	*0.2190*
MK205-2	‖	*0.1741*	*0.1546*	*0.2960*	*0.2170*
MK205-3	‖	*0.1584*	*0.1396*	*0.3070*	*0.2190*
MK205-4	‖	*0.1899*	*0.1694*	*0.3110*	*0.2390*

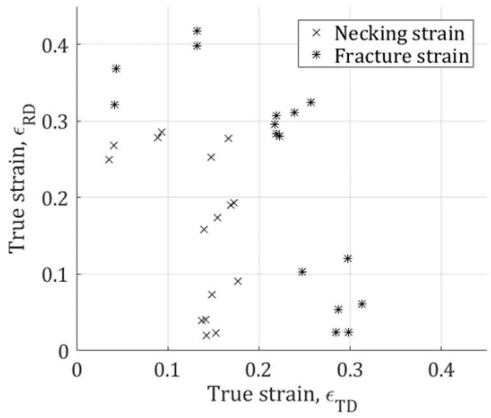

a.i)

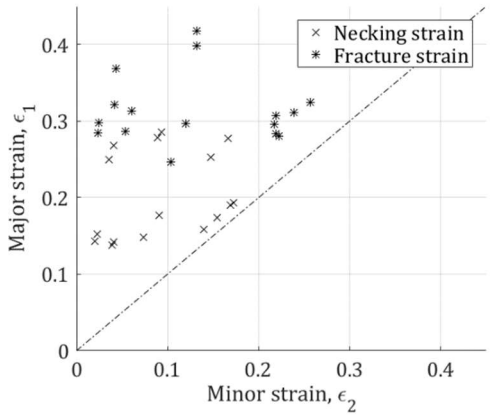

a.ii)

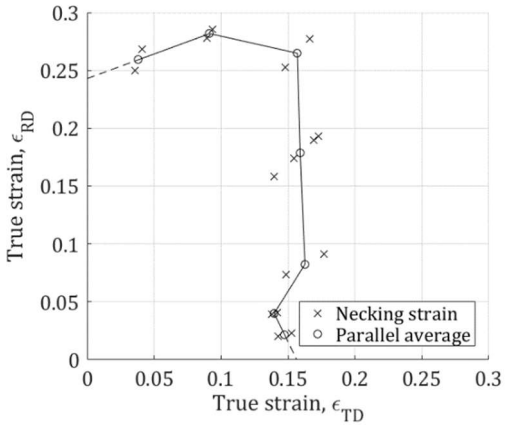

b.i)

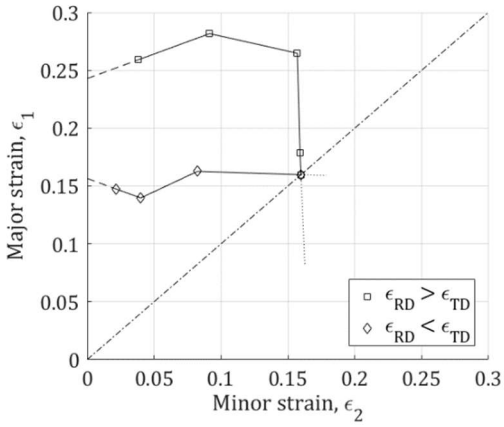

b.ii)

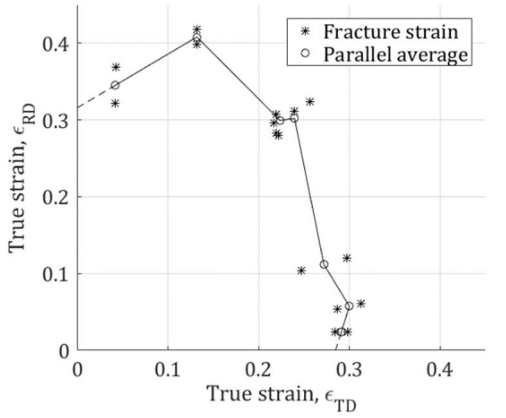

c.i)

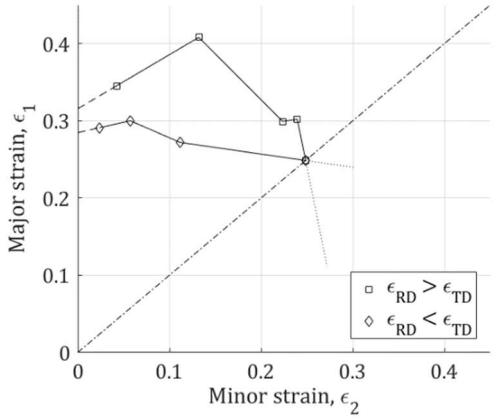

c.ii)

Figure 4-6: a) Scatter of experimentally measured strains from MK-test at the onset of local necking and fracture. b) Experimental forming limit curve (onset of local necking) from MK-tests, based on averages of experimental measurements. c) Experimental fracture limit curve from MK-tests, based on averages of experimental measurements.

4.2 Yield functions

4.2.1 Calibration methods

When calibrating the yield function, a number of coefficients determining the shape of the yield loci must be fitted for the plastic characteristics of the model to match the experimental observations in the best way possible.

The essence of the calibration process is to mathematically manipulate the current yield function to formulate expressions representing quantities which are practically measurable through experiments. Paired with a flow rule and the proper stress tensor configuration, ratios of stresses and strains can be expressed through rearranging of the yield function and its partial derivatives.

The number of anisotropy coefficients present in the yield function might affect the accuracy of the yield function, as the number of degrees of freedom in a function should be paired with an equal number of experimental test data.

Generally, there are two ways to fit a yield function to experiments. For simpler anisotropic yield functions with few anisotropy coefficients, analytical expressions which directly relates the anisotropic coefficients to experimental data might be available. For the yield functions presented in this paper where such analytical expressions are available, these expressions are presented in the respective chapters addressing the yield function.

For more complex yield functions with a larger number of anisotropy coefficients, such analytical expressions might be difficult to obtain mathematically. In such cases, a numerical calibration is performed through an optimization where the sum of squared differences between experimental data and the corresponding quantity predicted by the yield function is minimized. The error function which is subject to minimization can be formulated as

$$err = \sum_{l} \left(\frac{x(\boldsymbol{\sigma_{ij}}, \alpha_k)_l^{pre} - x_l^{exp}}{x_l^{exp}} \right)^2 \qquad \text{Eq. 4.2-1}$$

where $\boldsymbol{\alpha}$ is the vector of anisotropy coefficients, and $\boldsymbol{\sigma_{ij}}$ is the Cauchy stress tensor, while i represents the different entities used in the calibration. Superscripts pre and exp refer to predicted and experimental values of the current entities, respectively.

To set up Eq. 4.2-1, formulations of the predictions, $x(\boldsymbol{\sigma_{ij}}, \alpha_k)_l^{pre}$, must be established for the different entities. These initially large mathematical expressions are usually greatly reduced when the appropriate stress state of the experiment is implemented as the experiments are often of plane stress – leaving many zero-components to the stress tensor,

$\boldsymbol{\sigma_{ij}}$. As the components of the stress tensor is given by the nature of the experiments, the anisotropy parameters, α_k, can be found by minimizing the error function in Eq. 4.2-1.

The proposed experiments which must be conducted to calibrate a certain yield criterion might differ between models. Many of the more complicated yield criteria rely on experimental values of yield stresses, σ^Y, and Lankford constants (transverse strain ratios), R, to be obtained for several stress states. This might demand uniaxial tensile tests at multiple angles to the sheet rolling direction to obtain σ_θ^Y and R_θ, bulge tests to obtain the biaxial yield stress, σ_b^Y, and through-thickness disc compression tests to obtain the biaxial strain ratio, R_b - to acquire the calibration data. When the calibration is performed by minimization of an error function, setting one or more anisotropic coefficients to their isotropic value can sometimes be justified in cases where the number of data points provided is less than the number of anisotropy coefficients in the yield function.

Expressions for comparisons to the measured yield stresses are obtained by using the yield functions description of effective stresses, while expressions for the predicted Lankford constants can be obtained from the given flow rule. This is done for each experiment, by using the appropriate configuration of the Cauchy stress tensor, $\boldsymbol{\sigma}$**,** as input. For uniaxial tensile tests carved at an angle θ to the rolling direction, the components of the Cauchy stress tensor, $\boldsymbol{\sigma}$, in the material frame of reference are calculated as

$$\sigma_x = \sigma_\theta^Y \cdot \cos^2\theta$$

$$\sigma_y = \sigma_\theta^Y \cdot \sin^2\theta \qquad \text{Eq. 4.2-2}$$

$$\tau_{xy} = \tau_{yx} = \sigma_\theta^Y \cdot \cos\theta \cdot \sin\theta$$

Meanwhile, an equibiaxial tensile test yields the following components:

$$\sigma_x = \sigma_y = \sigma_b^Y$$

$$\tau_{xy} = \tau_{yx} = 0 \qquad \text{Eq. 4.2-3}$$

The predicted normalized yield stresses are calculated from the yield function as

$$\sigma_{\theta_i}^{Y,pre} = \sigma_0^{Y,exp} / \sigma^Y(\boldsymbol{\sigma})$$

Eq. 4.2-4

$$\sigma_b^{Y,pre} = \sigma_0^{Y,exp} / \sigma^Y(\boldsymbol{\sigma})$$

where the effective stress, $\sigma^Y(\boldsymbol{\sigma})$, is calculated as proposed by the current yield function, with the appropriate stress states of the Cauchy stress tensor, $\boldsymbol{\sigma}$, as inputs.

Using the associate flow rule which considers the gradient of a yield function predictions of Lankford constants obtained from uniaxial tensile tests performed at angle θ to the rolling direction can be expressed as [47]

$$R_\theta^{pre} = \frac{\sin^2\theta \frac{\partial f(\boldsymbol{\sigma})}{\partial \sigma_x} + \cos^2\theta \frac{\partial f(\boldsymbol{\sigma})}{\partial \sigma_y} - \sin\theta\cos\theta \frac{\partial f(\boldsymbol{\sigma})}{\partial \tau_{xy}}}{\frac{\partial f(\boldsymbol{\sigma})}{\partial \sigma_x} + \frac{\partial f(\boldsymbol{\sigma})}{\partial \sigma_y}}$$

Eq. 4.2-5

In the experimental data used for calibration in this thesis, the biaxial strain ratio was obtained by Dimitry Vysochinskiy from disc compression tests – a method to experimentally test the biaxial strain ratio which was first suggested in the article presenting the Yld2000-2d yield function by Barlat [16]. If the biaxial strain ratio is presented as the relationship between the minor and major traverse strain as,

$$R_b = \frac{\varepsilon_2}{\varepsilon_1} = \frac{(\partial f/\partial \sigma_2)}{(\partial f/\partial \sigma_1)} \leq 1$$

Eq. 4.2-6

consideration regarding the orientation of the major principal strain direction must be made, as the above equation does not contain the information of whether the major strain is aligned with the sheets rolling direction, x, or the sheets traverse direction, y. Therefore – for disc compression tests – the biaxial strain ratio is more appropriately described in terms of the coordinated aligned with the axis of anisotropy.

$$R_b^{pre} = \frac{(\partial f(\boldsymbol{\sigma})/\partial \sigma_y)}{(\partial f(\boldsymbol{\sigma})/\partial \sigma_x)} \begin{cases} < 1 \; if \; the \; major \; strain \; is \; in \; the \; x - direction \\ > 1 \; if \; the \; major \; strain \; is \; in \; the \; y - direction \end{cases} \quad \text{Eq. 4.2-7}$$

Followingly, the predicted values must be compared to the corresponding experimental values

$$R_b^{exp} = \begin{cases} R_b \; if \; the \; major \; strain \; is \; in \; the \; x - direction \\ {R_b}^{-1} \; if \; the \; major \; strain \; is \; in \; the \; y - direction \end{cases} \quad \text{Eq. 4.2-8}$$

Using ratios of stress and traverse strains from tests of equibiaxial tension as well as uniaxial tensile tests at different angles to the rolling direction, the error function as presented in Eq. 4.2-1 takes the form

$$err = \; err_\sigma + err_R$$

$$err_\sigma = \sum_i \left(\frac{\sigma_{\theta_i}^{Y,pre} - \sigma_{\theta_i}^{Y,exp}}{\sigma_{\theta_i}^{Y,exp}} \right)^2 + \left(\frac{\sigma_b^{Y,pre} - \sigma_b^{Y,exp}}{\sigma_b^{Y,exp}} \right)^2 \quad \text{Eq. 4.2-9}$$

$$err_R = \sum_i \left(\frac{R_{\theta_i}^{pre} - R_{\theta_i}^{exp}}{R_{\theta_i}^{exp}} \right)^2 + \left(\frac{R_b^{pre} - R_b^{exp}}{R_b^{exp}} \right)^2$$

where θ_i is the uniaxial tensile tests direction relative to the sheets rolling direction, and the superscripts pre and exp refers to predicted and experimental values of the current entities, respectively. It can be useful to express all yield stresses as normalized by the yield stress in the reference direction, $\sigma_0^{Y,exp}$. The error function is minimized by using any numerical solver capable of minimizing non-linear functions by changing all anisotropy variables simultaneously.

Three calibration programs were made by the author during the work on this thesis with the aim to calibrate the two linear transformation-based anisotropic yield functions Yld2000-2d and Yld89. The programs were made in Excel by establishing the mathematical description of the yield functions and their derivatives, as well as addressing all mathematical singularities. While both functions were calibrated through the minimization of the sum of squared errors (MSSE)-method in their respective

programs, the Yld89-function was calibrated in a third program by the semi-analytical approach proposed in the original article by Barlat and Lian [5].

4.2.2 Hill48 calibration

To calibrate the quadratic anisotropic yield criterion Hill48, experimental values presented in the previous chapter based on experiments conducted by Vysochinskiy [10] were used. Although several tests were performed in the study of Vysochinskiy, only three data points are needed to calibrate the Hill48 yield function, namely the traverse strain ratios at 0° and 90° angle to the rolling direction, R_0 and R_{90}, along with the flow-stress ratio, r_θ, from the specimen with $\theta = 45$.

Using the experimentally obtained data points, the Hill's constants for plane stress, along with the formulations of the anisotropic coefficients as requested for input by the FEA-software Abaqus/CAE, were calculated as presented in the theory chapter on Hill48. The fully analytical method constrains the yield function to the three provided data points. Thus, the model perfectly coincides with experimental values for these configurations, but for other configurations, the predicted flow-stress ratios and Lankford constants are free to deviate from the ones measured in experiments. The anisotropy coefficients are presented in the following table, followed by plots which display the characteristics of the identified plasticity model.

Table 4-5: Hill48 anisotropy coefficients for AA6016-T4.

		Hill's constants		*Abaqus/CAE input*
Hill48	$\boldsymbol{F}$	*0.3956*	$\boldsymbol{R11}$	*1.0000*
	$\boldsymbol{G}$	*0.5925*	$\boldsymbol{R22}$	*1.1159*
	$\boldsymbol{H}$	*0.4075*	$\boldsymbol{R33}$	*1.0060*
	$\boldsymbol{N}$	*1.5032*	$\boldsymbol{R12}$	*0.9989*

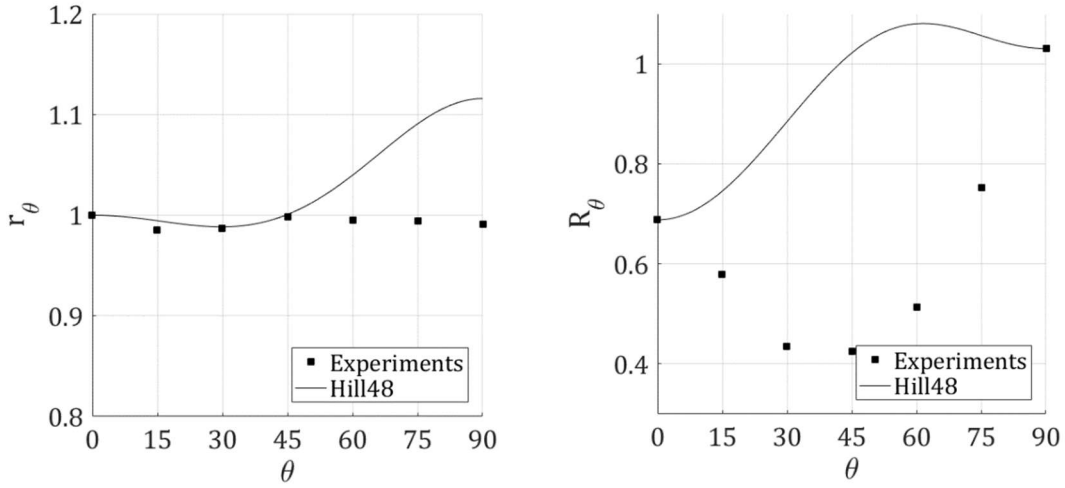

a) *b)*

Figure 4-7: a) Experimental and Hill48-predicted flow-stress ratios for AA6016-T4 as functions of the angle to the rolling direction. θ. b) Experimental and Hill48-predicted traverse stress ratios for AA6016-T4 as functions of the angle to the rolling direction.

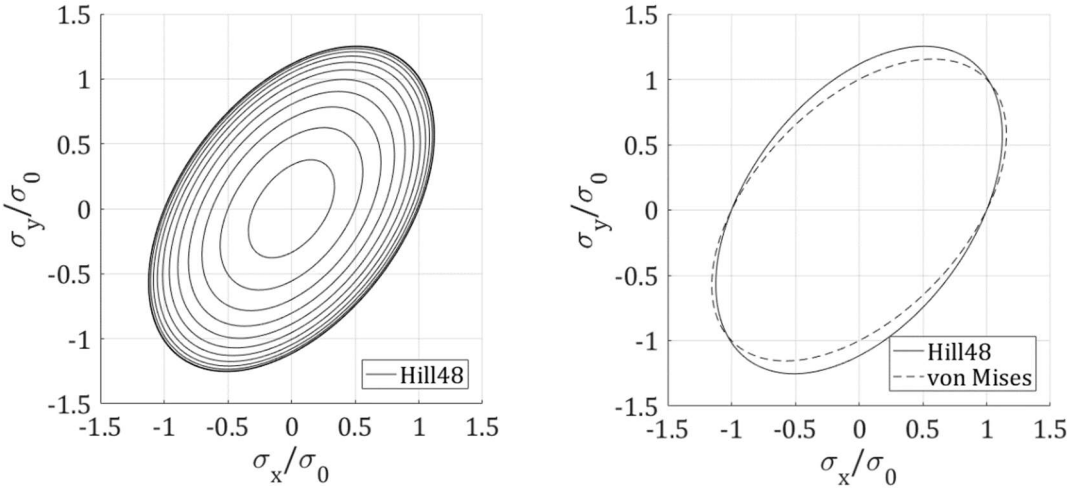

a) *b)*

Figure 4-8: a) Identified Hill48 yield loci for AA6016-T4 plotted in the space of σ_x, σ_y and τ_{xy}. b) Comparison of identified Hill48 yield surface for AA6016-T4 to the isotropic formulation.

Fig. 4-7 displays the plots of flow-stress ratios and Lankford constants predicted by Hill48 along with the experimental values. The flow-stress ratio at $\theta = 0$ by definition is equal

to the experimental value, and the value for $\theta = 45$ is constrained to the experimental value through the analytical calibration. From this, the model captures the flow-stress variation well for the lower angles but overshoot the predicted stresses as θ approaches the traverse direction of the sheet. The predicted Lankford constants, R_θ, are constrained to the experimental values at $\theta = 0$ and 90 through the analytical calibration. For the angles in between, the model is not at all capable of predicting the experimental values.

As the Hill48 yield criterion reduces to the von Mises criterion, one could naively imagine that a calibration of the anisotropic yield function to a material with isotropic yield characteristics would give Hill's constants which reproduces the isotropic characteristics of the material. Instead, the Hill48 yield function calibrated from Lankford constants gives severe anisotropic characteristics although calibrated to a material which from experiments is shown to have rather symmetrical yield strengths in rotation. This is in compliance with what is described in the literature about using similar quadratic yield functions to describe the behaviour of metals with face-centred cubic (FCC) crystal structure [55].

As plenty experimental data for AA6016-T4 is provided through the mentioned experimental program by Dimitry Vysochinskiy, the Hill48 yield function could have been calibrated in a minimized sum or squared errors-approach as described in the chapter *Calibration methods*. Though this would probably have provided a fairer comparison of the Hill48 to the other yield function examined in this thesis, this effort was not made as the literature suggests that quadratic yield functions are not suitable to describe the plasticity characteristics of aluminium alloys.

4.2.3 Yld89 calibration

Three different approaches were evaluated when calibrating the Yld89 yield function. First, the semi-analytical approach suggested by Barlat and Lien in the original article [5] was carried out. The method, described in detail in *Ch. 3.1.2*, uses only three experimental datapoints for calibration, namely the traverse strain ratios from uniaxial tensile tests, R_θ, with angles to the longitudinal axis θ at 0, 45 and 90 degrees to the sheets rolling direction.

The second approach, later referred to as *MSSE*, was to numerically calibrate through the minimization of a function of squared errors as described in the chapter on calibration methods. In the original article by Barlat and Lian [5], the relationship $a = 2 - c$ is specified. From the understanding of the author, there is nothing obvious in the article's proof which indicates that a violation of this relationship can yield loss of convexity for the function. Thus, a calibration considering all four anisotropy coefficients a, c, h and p as free parameters as seen done by Reyes et al. [6] can provide a better fit to experimental data. However, because obeying the relationship between a and c seems to be the normal in the literature, the proposed relationship was obeyed and thus only three of the four anisotropy the three variables were subjected to calibration. 14 data points – both traverse strain ratios, R_θ, and flow-stress ratios, r_θ, from all seven uniaxial tensile tests – were used for the calibration of the three anisotropy coefficients. The yield function exponent M = 8 was used, as is conventional for FCC metals.

The third calibration approach later referred to as *weighted MSSE*, was identical the previous, except a weighing among the squared errors was added. When considering the influence of discrepancies in the results among parallel experimental test on the yield function, the traverse strain ratios, R_θ, is seen to dominate the calibration. To address this, a weighting of the error function is common. The weighting of traverse strain ratios by the exponent $1/(w-1)$, as used by Reyes et al. [6], was therefore adopted. For the weighted MSSE, $w = M$ was used, while $w = 2$ was used for the non-weighted MSSE. The error function used to calibrate Yld89 takes on the following form.

$$err = \sum_i \left(\left(\frac{\sigma_{\theta_i}^{Y,pre} - \sigma_{\theta_i}^{Y,exp}}{\sigma_{\theta_i}^{Y,exp}} \right)^2 + \left(\frac{\left(R_{\theta_i}^{pre}\right)^{1/(w-1)} - \left(R_{\theta_i}^{exp}\right)^{1/(w-1)}}{\left(R_{\theta_i}^{exp}\right)^{1/(w-1)}} \right)^2 \right) \qquad \text{Eq. 4.2-10}$$

with $\theta_i = 0, 15, 30, 45, 60, 75$ and 90.

Table 4-6: Yld89 anisotropy coefficients for AA6016-T4 (with M = 8)

		Semi-analytical	*MSSE* $(w = 2)$	*Weighted MSSE* $(w = M)$
Yld89	$\boldsymbol{a}$	*1.0905*	*1.1072*	*1.1996*
	$\boldsymbol{c}$	*0.9095*	*0.8928*	*0.8004*
	$\boldsymbol{h}$	*0.8963*	*0.9433*	*1.0160*
	$\boldsymbol{p}$	*0.8429*	*0.8668*	*0.9655*

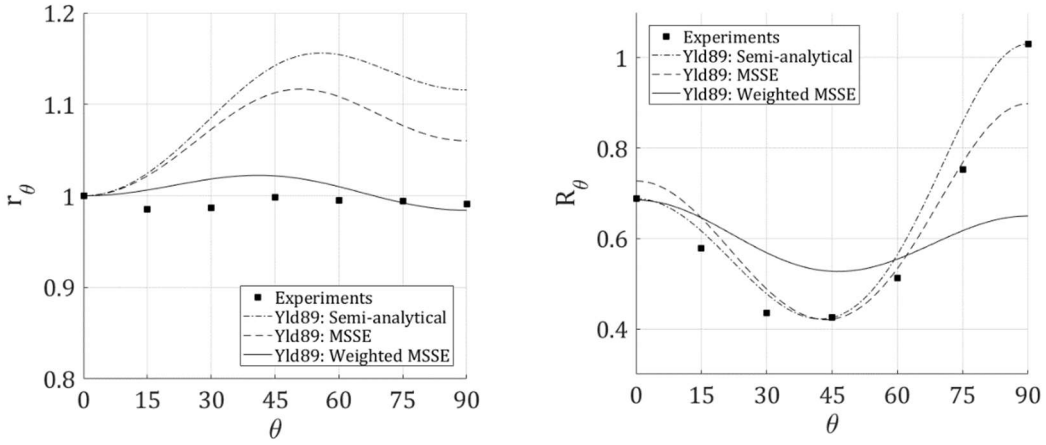

a) *b)*

Figure 4-9: Experimental and Yld89-predicted flow-stress ratios and traverse stress ratios for AA6016-T4 as functions of the angle to the rolling direction, θ. The different lines represent the different calibration methods.

The plots in Fig. 4-9 shows the comparisons between experimental values and values predicted by the different calibration method of Yld89. As the semi-analytical calibration constrains the model to three of the experimental traverse strain ratio-values, the description of the experimental values of this quantity is very good – however, artificially high ratios of flow-stresses are produced. The plain MSSE-approach also seems to capture the nature of the Lankford constant to a respectable good accuracy, but also this approach yields a false additional flow-stress when θ differs from zero. The weighted MSSE-approach is less successful in capturing the traverse strain ratios, but with a larger contribution of flow-stress ratio in the error function, the calibration yields a plasticity model which quite accurately describes the weak anisotropy of aluminium alloy AA6016-T4.

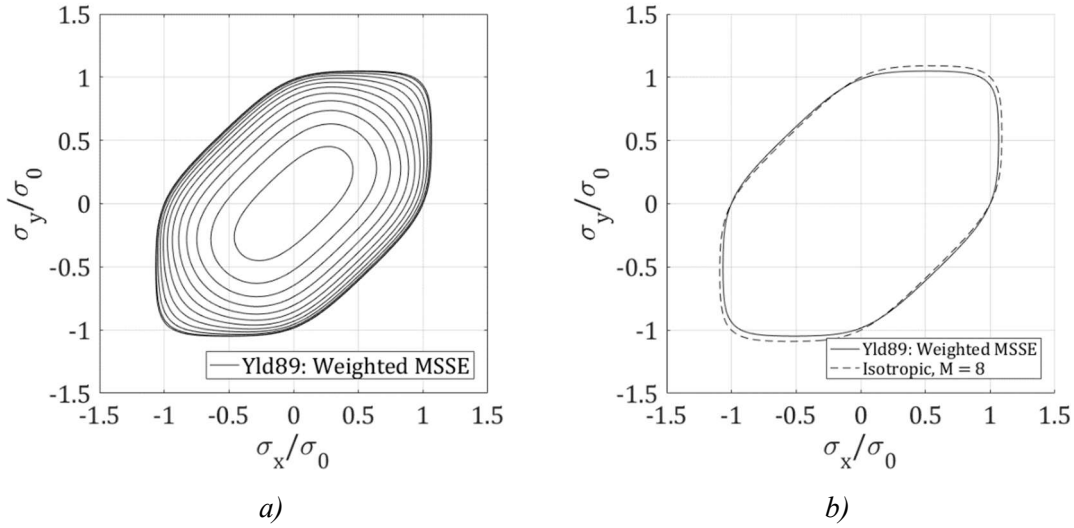

Figure 4-10: a) Identified Yld89 yield loci for AA6016-T4 plotted in the space of σ_x, σ_y and τ_{xy}. b) Comparison of identified Yld89 yield surface for AA6016-T4 to the isotropic formulation.

As a concluding remark, the Yld89-model seems to describe the plasticity of aluminium alloy AA6016-T4 significantly better than the quadratic Hill48 yield function. However, the accuracy in one of the two examined quantity seems to be obtained at the expense of the other. Therefore, consideration must be taken of whether a weighting of the two quantities should be used on not.

4.2.4 Yld2000-2d calibration

In the original article by F. Barlat presenting Yld2000-2d [16] the eight independent coefficients α_1 to α_8, which fits the Yld2000-2d criterion to capture the anisotropic yield characteristics of a material, are suggested to be simultaneously found from a numerical procedure. As with Yld89, this was done through minimization of an error function describing the sum of squared errors between the experimental and predicted descriptions of the same quantities (MSSE).

From the original article's suggestion, eight data points in the form of flow-stress ratios, r_θ, and Lankford constants, R_θ, are needed for the calibration.

Six data points are obtained through measurements from uniaxial tensile test-specimens carved at 0°, 45° and 90° to the rolling direction. Because these experimental quantities were available for $\theta = 0°$, 15°, 30°, 45°, 60°, 75° and 90° to the rolling direction, 14 experimental data points from uniaxial tensile tests were used for the calibration.

The two additional datapoints are suggested to be the same two quantities obtained from equibiaxial tension. In the article, Barlat suggests the traverse strain ratio from equibiaxial tension, R_b, to be obtained from a disc compression test – which is what was conducted by Dimitry Vysochinskiy to obtain the value presented in the chapter *Experimental calibration data.* The biaxial flow-stress ratio, r_b, is typically obtained by performing a bulge test, where a clamped circular freestanding part of the sheet metal is subjected to a pressurized fluid on one side, while the resulting bulge on the opposite side is monitored [48]. As such a measurement wasn't performed in the experimental program of Vysochinskiy, the data point was set to the isotropic value of 1. Thus, a total of 16 data points were used to calibrate the eight anisotropy coefficients. The exponent, M, was set to 8, as has proved to be a good fit for FCC metals.

In the calibration program that was written for this task by the author, two different calibrations were performed by the MSSE-method. First, a calibration where all errors were treated equivalently was performed. Then – as for the Yld89-calibration – the weighting of traverse strain ratios by an exponent of $1/(w-1)$, as used by Reyes et al. [6], was used. For the weighted MSSE, $w = M$ was used, while $w = 2$ was used for the un-weighted MSSE. The error function is presented in Eq. 4.2-11, while Table 4-7 presents the anisotropy coefficients obtained from calibration.

$$err = err_\sigma + err_R$$

$$err_\sigma = \sum_i \left(\frac{\sigma_{\theta_i}^{Y,pre} - \sigma_{\theta_i}^{Y,exp}}{\sigma_{\theta_i}^{Y,exp}} \right)^2 + \left(\frac{\sigma_b^{Y,pre} - \sigma_b^{Y,exp}}{\sigma_b^{Y,exp}} \right)^2 \qquad \text{Eq. 4.2-11}$$

$$err_R = \sum_i \left(\frac{\left(R_{\theta_i}^{pre}\right)^{\frac{1}{w-1}} - \left(R_{\theta_i}^{exp}\right)^{\frac{1}{w-1}}}{\left(R_{\theta_i}^{exp}\right)^{\frac{1}{w-1}}} \right)^2 + \left(\frac{\left(R_b^{pre}\right)^{\frac{1}{w-1}} - \left(R_b^{exp}\right)^{\frac{1}{w-1}}}{\left(R_b^{exp}\right)^{\frac{1}{w-1}}} \right)^2$$

Table 4-7: Yld2000-2d anisotropy coefficients for AA6016-T4 (with M = 8).

		MSSE $(w = 2)$	*Weighted MSSE* $(w = M)$
Yld2000-2d	$\boldsymbol{\alpha_1}$	*1.0328*	*1.0178*
	$\boldsymbol{\alpha_2}$	*1.1171*	*1.1508*
	$\boldsymbol{\alpha_3}$	*1.0650*	*1.0554*
	$\boldsymbol{\alpha_4}$	*1.0787*	*1.0915*
	$\boldsymbol{\alpha_5}$	*1.1135*	*1.1205*
	$\boldsymbol{\alpha_6}$	*1.0843*	*1.1008*
	$\boldsymbol{\alpha_7}$	*1.0159*	*1.0134*
	$\boldsymbol{\alpha_8}$	*1.2822*	*1.2380*

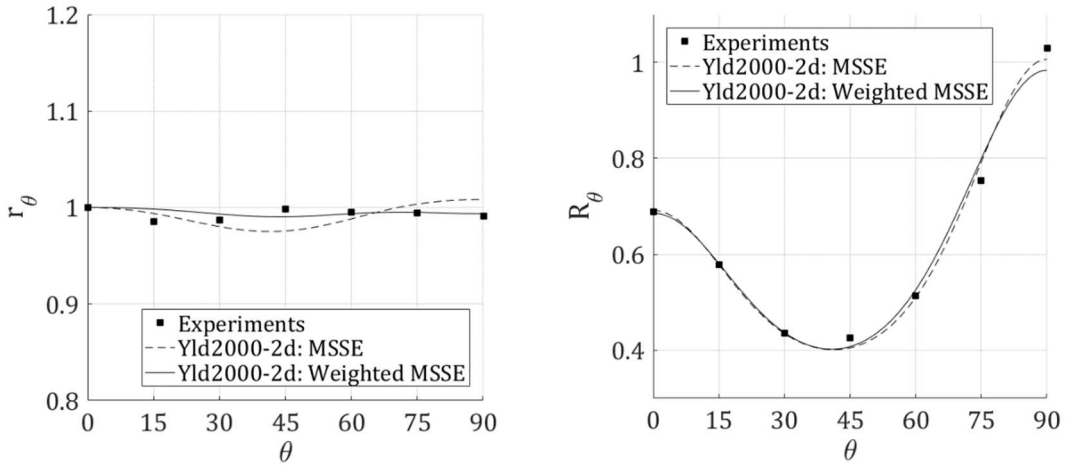

a) *b)*

Figure 4-11: Experimental and Yld2000-2d-predicted flow-stress ratios and traverse stress ratios for AA6016-T4 as functions of the angle to the rolling direction, θ. The different lines represent the different calibration methods.

Comparisons between experimental values and values predicted by the two methods used to calibrate Yld2000-2d are displayed plots in Fig. 4-11. Compared to the two previously addressed yield functions, the Yld2000-2d with its eight anisotropy components manages to reproduce the experimental results superiorly. Both the plain MSSE and the weighted MSSE yields traverse strain ratios with comparable accuracy to the semi-analytical and non-weighted calibrations of Yld89. At the same time, both calibrations described the

flow-stress ratios with similar or better precision than the weighted MSSE-calibrated Yld89 yield function.

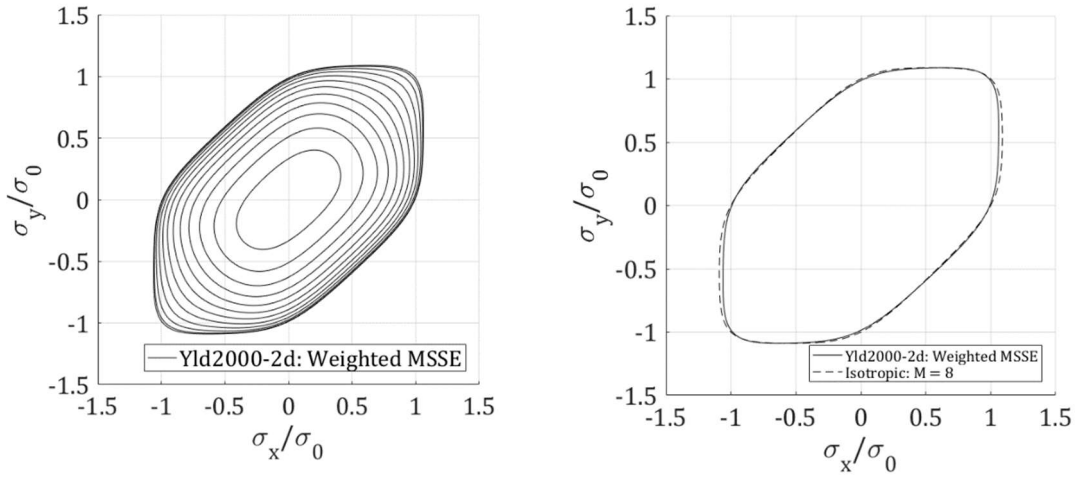

a) *b)*

Figure 4-12: a) Identified Yld2000-2d yield loci for AA6016-T4 plotted in the space of σ_x, σ_y and τ_{xy}. b) Comparison of Identified Yld2000-2d yield surface for AA6016-T4 to the isotropic formulation.

4.3 Hardening calibration

Coefficients which calibrates four different hardening functions, namely the Power law, the Ludqik's law and the one- and two-term Voce hardening rule, to AA6016-T4 aluminium alloy is presented in this chapter. While the parameters for the Power law and the two-term Voce rule were presented in the Ph.D.-thesis of Dimitry Vysochinskiy [10], the Ludwik's law and the one-term Voce rule were additionally calibrated by the author of this thesis to the very same experimental data.

The calibrations were performed by numerically minimizing the sum of squared discrepancies between the respective work hardening functions and the true stress vs. plastic strain curves obtained from the four uniaxial tensile tests with longitudinal axis parallel to the reference rolling direction. Only data from strains beyond the onset of yield at $\varepsilon^t = 0.002$ were considered in the fitting. The hardening parameters are presented in

Table 4-8, while Fig. 4-13 displays the fitted curves along with the experimental data points from one of the uniaxial tensile tests (UT0-1).

Table 4-8: Hardening coefficients for AA6016-T4

Power law (from Vysochinskiy [10]*)*

K [MPa]	n
516.3	*0.298*

Ludwik's law

σ_0 [MPa]	K [MPa]	n
95.4	*404.45*	*0.38*

One-term Voce rule

σ_0 [MPa]	Q_{R1} [MPa]	Q_{R2} [MPa]
142.6	*207.15*	*1927.27*

Two-term Voce rule (from Vysochinskiy [10]*)*

σ_0 [MPa]	Q_{R1} [MPa]	Q_{R2} [MPa]	Θ_{R1} [MPa]	Θ_{R2} [MPa]
139.0	*44.26*	*171.93*	*1070.93*	*1259.17*

The hardening curves for small values of the effective plastic strain is displayed in Fig. 4-13.b). The comparison between the different hardening models and the experimental results shows that the three hardening models which include the yield stress term, σ_0, all manage quite well to replicate the experimental hardening curve, while the Power law curve to some extent deviates from the measurements. For effective plastic strains exceeding the fracture strain of the uniaxial tensile specimen, the Power law and the Ludwik's law predicts a more aggressive work hardening-evolution than the two Voce-

models. The two curves begin to deviate at the strain level of the last experimental data point, which seems to be placed between the stress values predicted by the two models.

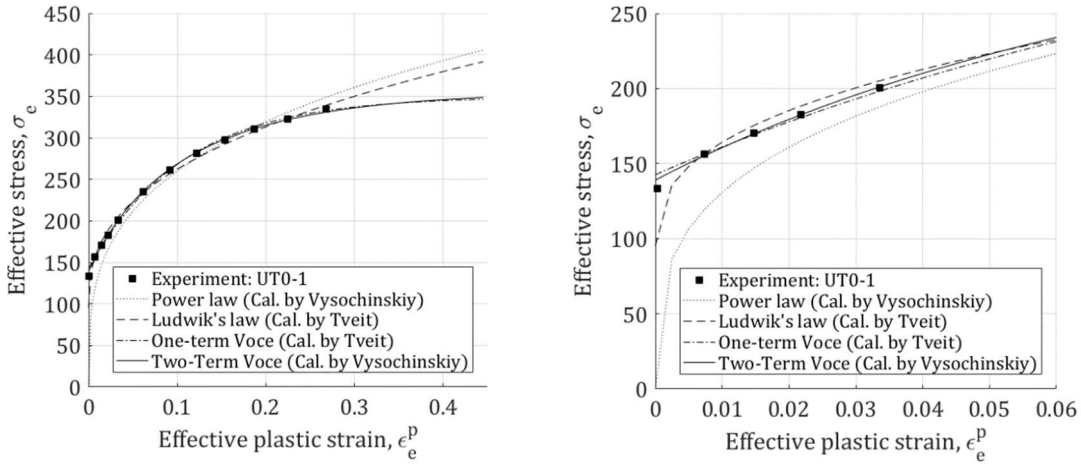

a) *b)*

Figure 4-13: a) Comparison of the four fitted hardening curves to the experimental data points from UT0-1. b) Expanded view of the work hardening models for small strains, displaying the discrepancies between models and experiments for small effective plastic strains.

Although the Voce hardening rule is established as the favourable model to describe the work hardening of aluminium alloys, its saturation at large plastic strains is a known issue. In such cases, a modification to the Voce function by a constant stiffness which overrules the original function when the Voce stiffness drops below it can be used [8]. Therefore, an evaluation of whether such an extension is appropriate or not should be made based on the levels of effective plastic strains at fracture for the assessed model.

4.4 Through-thickness shear instability criterion

The through-thickness shear instability criterion was calibrated to each material model in a one-step inverse modelling procedure by performing a Finite Element analysis in LS-DYNA of one element in the patch-model with dimensions 1.2 mm by 1.2 mm.

The model was calibrated using the equations as presented in the chapter addressing the theory chapter on the TTSI-criterion. As the major strain directions of the PST tests were in the sheets rolling direction so that $\theta = 0$, the principal axis of stress coincide with the principal axis of anisotropy. Thus, the angle of the inclination of the maximum shear plane, φ, can be calculated for an isotropic material by the same equation presented by Bressan & Williams [7] in the original article anisotropic materials as shown by Brunet & Clerc [50]. With fracture strains for the PST test at $\bar{\varepsilon}^*_{x,PST} = 0.6237$ and $\bar{\varepsilon}^*_{y,PST} = -0.1323$, the inclination of the maximum shear plane, $\varphi = 48.41°$.

A non-local proportional strain corresponding to the average strain path of the six plane strain tension (PST) tests as presented by Vysochinskiy [10] was applied to the element in the Finite Element analysis. The time at which the FE-analysis reached the average fracture strains from the experimental PST tests was recorded, and the value of the major stress component $\sigma_1^* = \sigma_x^*$ was read for each individual plasticity model. From this, the critical shear stress, τ_{cr}, as predicted by the TTSI-model was calculated for the different plasticity models using Eq. 3.3-7.

Table 4-9: Critical values of the TTSIC calibrated for Yld2003 and different calibrations of Yld89.

	$\boldsymbol{\tau_{cr}}$ **[MPa]**
Yld89 – Semi-analytical	*180.29*
Yld89 - MSSE	*180.53*
Yld89 – Weighted MSSE	*179.35*
Yld2003 – LS-DYNA calibration	*179.83*

As the TTSI-criterion is calibrated for use in the LS-DYNA material model which is referred to by the program as *135-WTM-STM*, the critical shear stress was only calculated for the yield functions Yld89 and Yld2003, as these are the only yield functions available in this LS-DYNA material model. The critical values are presented in Table 4-9. As displayed, the discrepancies between different values are very small. The critical values

for Yld2003 lie in the interval of discrepancies between the different calibrations of Yld89.

4.5 Roping model calibration

The fitting of the sum of sine waves in the **PERTURBATION_SHELL_THICKNESS*-keyword is performed using the Sum of Sines Models-tool in MATLAB R2020a. The tool allows fitting the sum of up to eight sine waves to a provided set of data describing the detailed distribution of thickness variations along one axis. As the roping effect mainly produces variation in thickness along the traverse direction, a unidirectional model was used. The formulation used in MATLAB takes the following form:

$$p(y) = \sum_{i=1}^{n} a_i \sin(b_i y + c_i) \ for\ 1 \leq n \leq 8 \qquad \text{Eq. 4.2-12}$$

From this, the fitted parameters a_i, b_i and c_i, which produces an approximated perturbation field from the sum of harmonic perturbations, is related to the input variables requested in LS-DYNA as

$$AMPL_i = a_i$$
$$YWL_i = \frac{2\pi}{b_i} \qquad \text{Eq. 4.2-13}$$
$$YOFF_i = \frac{c_i}{b_i}$$

In this study, very limited information was available about the nature of the roping phenomenon of the assessed aluminium sheets. Thus, information about the distance between valleys formed by roping was taken from visual inspections on the effective strain map from DIC for the last image before fracture, presented by Vysochinskiy [10]. Using the sample which most clearly showed the localisations of strains, namely the sample labelled as MK160-90-2 in Vysochinskiy's study, (see Fig. 4-14) the approximated distance between roping valleys was roughly measured to be 12.5 mm in

the last image prior to fracture. With the reported non-local logarithmic fracture strain at 0.2870 for the sample, the initial distance was calculated to be approximately 8.9 mm.

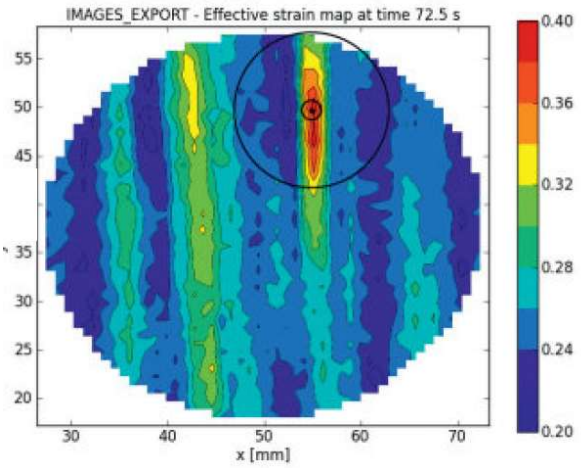

Figure 4-14: Effective strain map at the last frame prior to fracture of the sample labelled as MK160-90-2 of virgin AA6016-T4 (ID=6). Figure rendered from 'Formability of aluminium alloy subjected to pre-strain by rolling' by D. Vysochinskiy [10] *with permission from the author.*

From this approximated distance between grooves, along with the mean measured thickness of 1.496 mm and standard deviation of 0.004 mm from thickness measurements performed in the experimental study, a fictive thickness profile was established which could be used to fit a four-term sine wave roping perturbation model to. Fig. 4.15 shows the fictive perturbation measurements along with the fitted four-term sine wave model, while Table 4-10 displays the amplitude, $AMPL_i$, wavelength, YWL_i, and off-set, $YOFF_i$, for each of the four harmonic functions.

Table 4-10: Fitted parameters of the four-term sine wave roping perturbation.

	$\boldsymbol{AMPL_i[mm]}$	$\boldsymbol{YWL_i\ [mm]}$	$\boldsymbol{YOFF_i\ [mm]}$
$i = 1$	*0.001681*	*4.46249*	*3.382102*

$i = 2$	*0.001298*	*2.976402*	*-0.6920891*
$i = 3$	*0.004363*	*8.907266*	*-2.266799*
$i = 4$	*-5.2460E-6*	*8.824698*	*-5.549157*

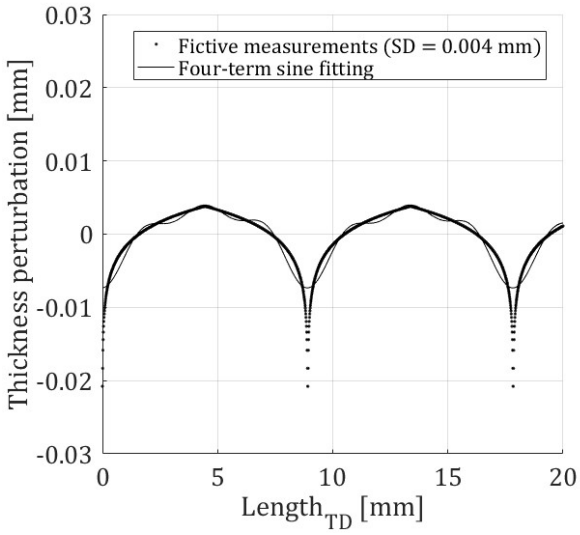

Figure 4-15: The scatter of dots represented the fictive thickness profile, which is based on the measured mean thickness and standard deviations, along with a visual inspection of effective strain plots from DIC. The curve represents the four-term sine wave model fitted to the fictive profile.

5 Non-linear finite element analysis in LS-DYNA

Several Finite Element Analysis-software allows for multiple pre-programmed options for the program formulation. Some of the key components of the finite element are the keywords which describe the different parts of the constitutive behaviour of the material. A large number of different models aiming to describe the behaviour of materials for different purposes have been presented in the literature throughout the years – some more successful than others. Thus, the number of different pre-programmed material models available in the various FEA-software differ. For solids such as aluminium, the material description might include the following;

- Elasticity:
    - Elastic stiffness
    - Poisson ratio
- Plasticity:
    - Yield function
    - Flow rule
    - Hardening
- Damage and failure:
    - Damage initiation criterion
    - Damage evolution
    - Failure criterion

In describing these different features of the material model, some pre-programmed material models exclude the use of others.

In addition to the pre-programmed modules, many advanced FEA-programs allows the user to interact with the finite element code. This way, material models – or other features which are not implemented in the software originally – may be programmed by the user. Such operations might require somewhat advanced knowledge about the current programming language used, in addition to extended program licenses. As user-programmed material models were considered beyond the scope of this thesis, only the pre-programmed models were used to conduct the analyses.

In preliminary work of this study, the multi-purpose finite element-software Abaqus/CAE was used to establish a model which could recreate the behaviour of AA6016-T4. However, due to the lack of material models suitable for aluminium alloys among the commercially available pre-programmed modules in Abaqus/CAE, a switch was made to the Livermore Technologies produced FEA-software LS-DYNA, which was used to conduct analyses in this study.

Seeking to explore if the constellations of some of the material models describing plasticity, local necking and fracture accompanied with the four-term sine wave roping model were able to describe the behaviour of AA6016-T4 observed in the experimental program by Dimitry Vysochinskiy [10], a model was established in the finite element method program LS-DYNA.

The plane stress material model referred to in the program as *WTM_STM*, short for Weak Texture Model and Strong Texture Model, was used. The pre-programmed and commercially available module is an anisotropic viscoplastic material model which adopts two of the anisotropic yield functions previously addressed in this study, namely Yld89 by Barlat and Lian [5] (WTM) and Yld2003 (STM) by Aretz [17]. While the WTM requires its input of the form of the four Yld89 anisotropy coefficients a, c, h and p, the STM allowed input for Yld2003 both as the eight coefficients of anisotropy a_1 to a_8, and as direct experimental values of r_0, r_{45}, r_{90}, r_b, R_0, R_{45}, R_{90} and R_b – conveniently, as Yld2003 was not included in the calibration program in this thesis.

Fig. 5-1 displays the flow-stress ratios and traverse strain ratios as functions of the angle to the rolling direction, θ, predicted by Yld2003 calibrated automatically in LS-DYNA. The graph is compared to the predictions by the weighted MSSE-calibrated Yld2000-2d yield function, which was considered to be the most suiting of the calibrated model in the previous chapter. From visual inspection of the figure, Yld2003 seems to provide a fit to experiments comparable to that of Yld2000-2d.

According to the LS-DYNA material manual [56], files with data to plot of the yield loci were supposed to be generated when using the automatic calibration of Yld2003. Unfortunately, the generated files contained zero information. As the eight anisotropy coefficients are not generated, and no information about the used calibration method is

provided, a plot of the automatically calibrated Yld2003 yield surface is missing in this thesis. Instead, the input data used is summarized in table 5-1 for verifiability reasons.

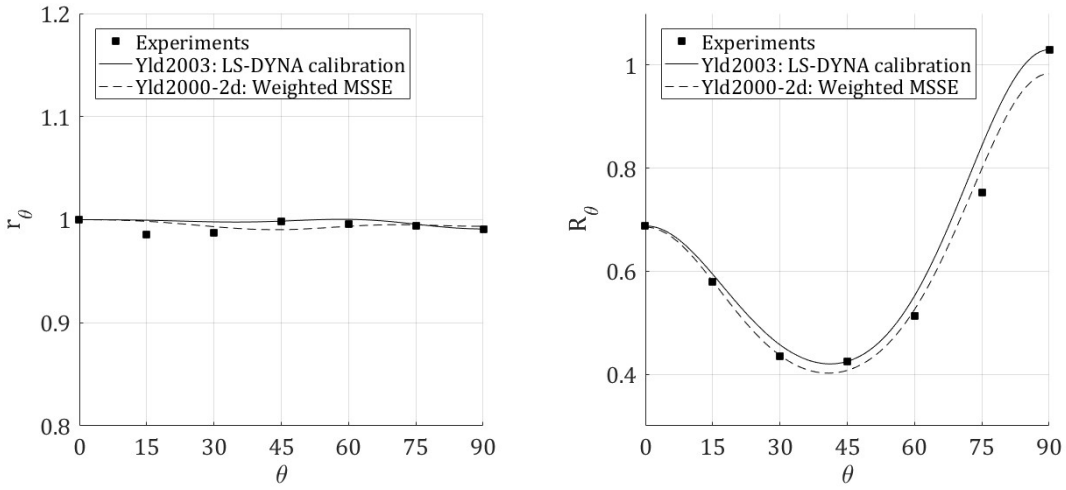

Figure 5-1: Experimental and Yld2003-predicted flow-stress ratios and traverse stress ratios for AA6016-T4 as functions of the angle to the rolling direction, θ, calibrated automatically in LS-DYNA.

Table 5-1: LS-DYNA input values for automatic calibration of the Yld2003 yield function, based on experiments conducted by Vysochinskiy [10].

	r_0	r_{45}	r_{90}	r_b	R_0	R_{45}	R_{90}	R_b	M
LS-DYNA notation	***S00***	***S45***	***S90***	***SBB***	***R00***	***R45***	***R90***	***RBB***	***2K***
	1.000	*0.9986*	*0.9910*	*1.000*	*0.6880*	*0.4250*	*1.030*	*0.7850*	*8*

In addition to the plasticity models, which are accompanied with the associate flow-rule, *WTM_STM* also incorporates the though-thickness shear instability criterion (TTSIC) for the prediction of local necking and the original Cockcroft-Latham criterion (OCLFC) for fracture. Accompanied by the material keyword *NONLOCAL*, a history variable describing the state of the non-local instability criterion (NLIC) is supposedly produced by the *WTM_STM* material model [49]. As mentioned in the theory chapters, this history

variable describes the relationship between the local and non-local through-thickness strain increment, β_i, was seemingly not produced as output from the analysis as requested. Thus, the non-local extremal thickness strain deviation criterion (NLETSDC) – addressed in detail in the theory chapters – was established to detect the onset of local necking from the available history variables.

In preliminary runs conducted to validate the FEA-model with the material model WTM_STM, the 60 mm by 60 mm patch (further introduced in *Ch. 5.2 Forming and fracture diagrams from FEA in LS-DYNA*) was subjected to equibiaxial strains with the two different yield functions available in the model, namely Yld89 (WTM) and Yld2003 (STM). When displaying the results as colour plots of effective Von Mises stresses, unexplainable stress concentrations, structurally aligned in diagonals, were observed when using the WTM. Fig. 5-2.a) and b) shows the described stress concentrations with 50x50 and 70x70 Belytschko-Tsay elements, respectively.

The two patches were equipped an unperturbed, perfectly even thickness of 1.496 mm. As the mysterious interference pattern remained unexplained, a decision to proceed only with the Yld2003 yield function as plasticity model.

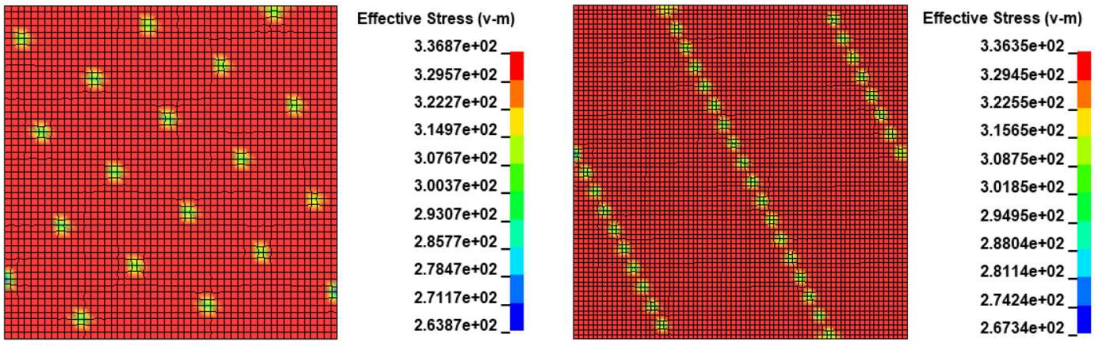

a) *b)*

Figure 5-2: Unexplained stress concentrations which emerged when using the weak texture model in the WTM_STM material keyword in LS-DYNA with input from the weighted MSSE-calibration of Yld89. a) 50x50 Belytschko-Tsay shell elements. b) 70x70 Belytschko-Tsay shell elements.

5.1 Uniaxial tensile tests

To assure the correct appliance of the *WTM_STM* material keyword in LS-DYNA, an attempt was made to approximately simulate the experimental uniaxial tensile tests performed by Vysochinskiy. In the experimental program, uniaxial tensile tests were performed at seven different angles to the rolling direction, θ, and the notation UTθ was to address the different tests. On seven identical FEM-models, the material model was assigned to a local coordinate system which was rotated at the same seven different angles to the specimen's longitudinal direction.

Modelling the 12.5 mm wide and 70 mm long gauge of the dog-bone type specimen (which geometry is presented in the *Ch. 4.1.1*), 13x70 Belytschko-Tsay shell elements with five integrations points in the through-thickness direction was used after convergence had been verified in a mesh refinement procedure. The shell thickness was set to 1.496 mm which corresponds to the mean of measurements as presented in the experimental report.

As the main aim of the analysis was to validate the finite element model prior to further analyses, no attempts were made to model phenomena unique to uniaxial tensile tests. While the OCLFC and the TTSIC were implemented for the sake of curiosity, no attempts were made to address the phenomenon of diffuse necking. Instead, attention was aimed at the anisotropy of the plasticity model and strain hardening.

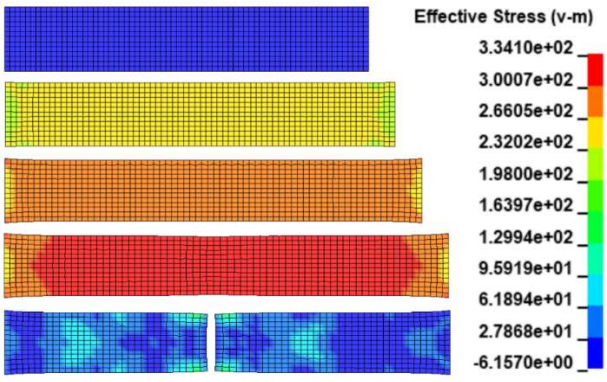

Figure 5-3: Field plots of effective Von Mises stress at five different stages of the analysis of the UT0-specimen.

Field plots of the effective Von Mises stress from a nodal averaging scheme at five different instances for the simulation of the UT0-specimen is illustrated in Fig. 5-3. The fourth frame from the top shows the last frame prior elements are deleted due to TTSIC, while the fifth frame shows the state of the modelled specimen right after fracture.

To validate the plasticity model, the effective strains to the effective Von Mises stress was plotted for the most centred of the elements which first were deleted from the fracture criteria. Fig. 5-4 displays the comparisons of the different simulations.

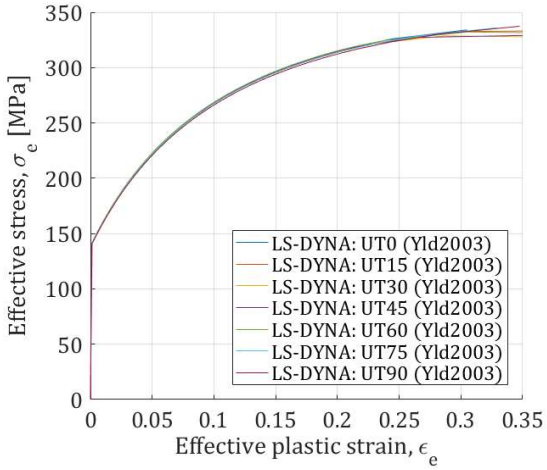

Figure 5-4: Effective stresses vs. effective plastic strains from the FE-analysis of uniaxial tensile tests with the longitudinal axis at different angles to the rolling direction.

With the moderate anisotropy of stresses for the AA6016-T4, the global work-hardening curves are not suited to validate the FE-model, and directional stress differences at low strains were therefore further investigated. With time intervals between result outputs being 0.05 seconds, the interpolated values for effective Von Mises stress at effective plastic strains of 0.0014 was used to approximately calculate the flow-stress ratios, as can be seen in Fig. 5-5. As evident from the figure, the approximate calculations of flow-stress ratios from the FE-model expectedly coincided with the predictions of the underlying model, verifying the correct appliance of the material model in the FEA-model.

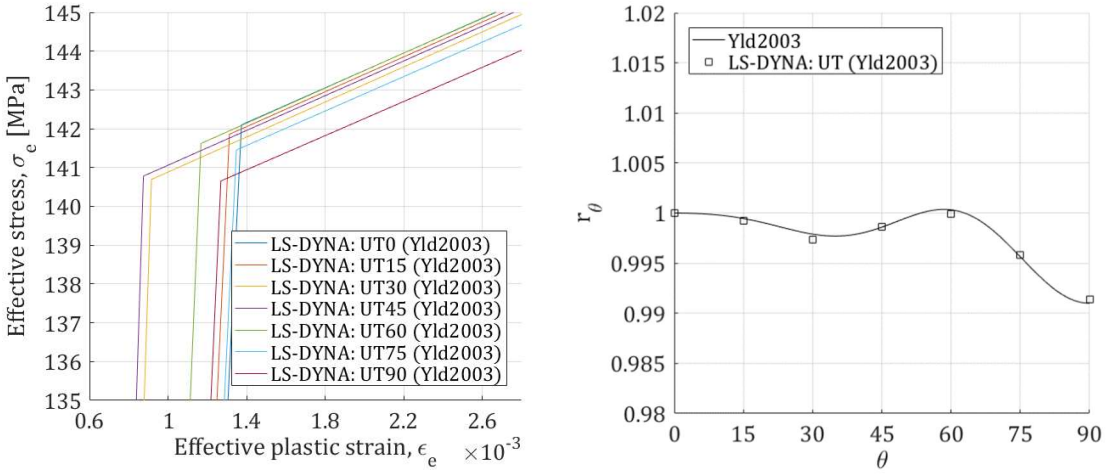

a) *b)*

Figure 5-5: a) Magnification of work hardening plots from UT simulations to display values at low plastic strains. b) Flow-stress variation of Yld2003 and values read from LS-DYNA simulations of uniaxial tensile tests. The values were calculated from the interpolated value at effective plastic strains of 0.0014.

Comparisons of the individual simulations to their corresponding experimental true stress to true strain curves are furtherly displayed in Fig. 5-6. The isotropic two-term Voce hardening law fitted by Vysochinskiy [10] to the UT0-data seems to somewhat accurately describe the work hardening observed in the differently angled specimens. The observation made in the calibration chapter that the Voce hardening seems to predict a continuation of the hardening curve which is somewhat flatter than what can be imagined by visually judging the fit is furtherly confirmed.

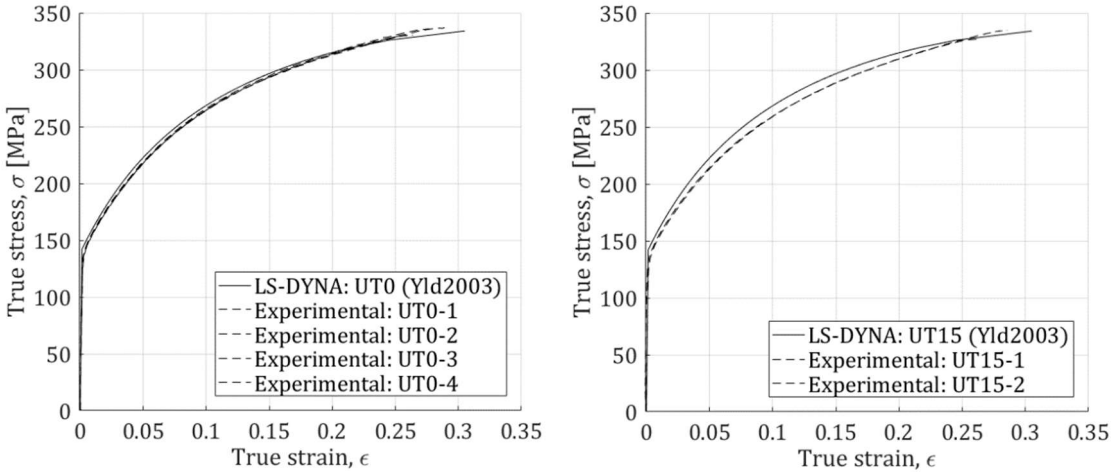

a) *b)*

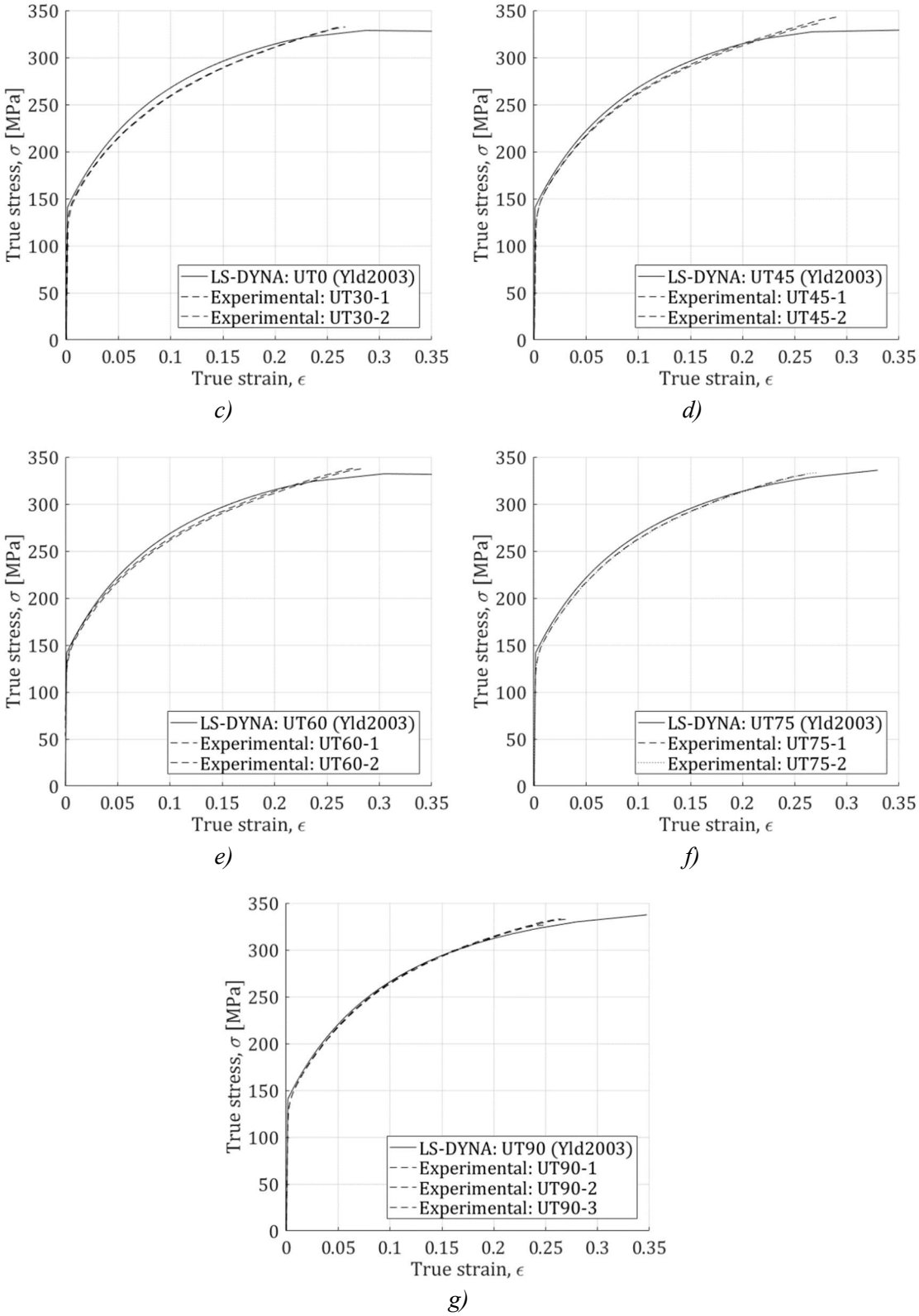

Figure 5-6: Comparisons between experimental and FEA work diagrams from uniaxial tensile tests.

5.2 Forming and fracture diagrams from FEA in LS-DYNA

5.2.1 FEA-model

To construct the FEA-generated forming and fracture limit diagrams in LS-DYNA, a 60 mm by 60 mm squared patch of Belytschko-Tsay shell elements was subjected to 15 different proportional biaxial deformations. The evenly distributed thickness of 1.496 mm, corresponding to the mean values from measurements, were represented by five through-thickness integration points. The four individual edges were constrained in every direction except for in the direction of the edges themselves. A controlled displacement was then assigned to the right and the top edge in their normal directions to create the non-local, proportional, biaxial strain paths.

Different element sizes were explored to assure the model's convergence. For this, the Yld2003 plasticity model was used along with the TTSIC and the OCLFC. Meshes with 50x50, 70x70 and 90x90 elements were used to model the 60 mm by 60 mm patch with even thickness of 1.496 mm, subjected to plane strain tension in the rolling direction. By plotting the effective mises stresses vs. the effective plastic strains for one of the elements which were first deleted due to fracture for the three different models, only a negligible difference was observed. The three models also experienced element removal from the TSSIC at nearly identical strains. Meanwhile, the CPU time of the analysis was increased 2.5 times when the mesh was refined to 70x70, and 5.4 times for the 90x90 mesh.

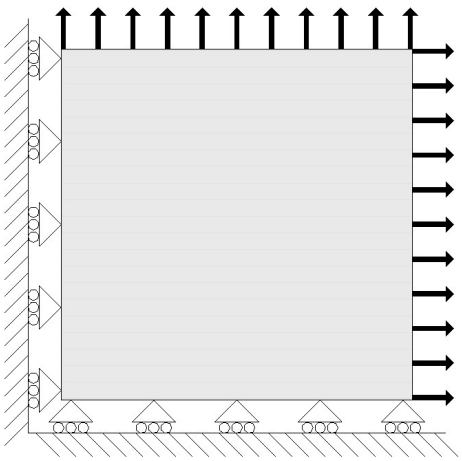

Figure 5-7: Boundary conditions of the patch model subjected to biaxial strains paths for the construction of FEA-generated forming and fracture limit diagrams. The rolling supports should be considered continuous along the edges.

Along with the Yld2003 yield function, three different criteria to simulate local necking and fracture were implemented to see if the models could recreate experimental limits. Through the material keyword *WTM_STM*, TTSIC and OCLFC were implemented as uncoupled criteria where satisfaction of either of the criteria in 3 out of the 5 through-thickness integration points in an element caused the element to be removed from the model. As the NLETSDC was not implemented into the material model, the fulfilment of the criterion was detected through manually monitoring the through-thickness strains. When either of the criteria was satisfied, the displacements in the two directions were recorded, and the non-local strain values were calculated as the necking or fracture strains.

5.2.2 Non-local extremal thickness strain deviation criterion (NLETSDC)

The non-local extremal thickness strain deviation criterion which was used as a replacement for the established NLIC, as LS-DYNA seemingly failed to output the requested non-local history variable used in the criterion. The NLETSDC was first implemented with the four-term sine wave shell thickness perturbation fitted to the artificial thickness section presented in *Ch. 4.5*, which was generated based on the thickness measurements presented by Dimitry Vysochinskiy [10], with a mean thickness,

$\bar{t}$, of 1.496 mm and standard deviation, SD, of 0.004 mm. The thickness perturbation serves as an imperfection which naturally triggers strain localizations in the weaker sections in the patch when the equilibrium condition is imposed. As neither of the non-local

To test the unexplored criterion, a sensitivity analysis of the critical extremal thickness strain ratio, ξ_{cr}. On the unscaled roping perturbation model, forming limit curves were plotted with the critical values set to 1.5, 2.0 and 3.0. The different curves, displayed in Fig. 5-8.a), shows that variations in critical value yield small differences in forming limits. The even and predictable shape of the forming limits produced by the NLETSDC indicates that the criterion is capable of producing stable results for the model. For further analysis, ξ_{cr} = 2.0 was used as the critical value.

With the four-wave sine wave perturbation model unscaled (Sc. = 1.0), i.e. fitted to the artificial measurements with the measured thickness standard deviation presented in *Ch. 4.5*, the forming limit diagram exhibited moderate anisotropy in the direction of the experimental observations. The two plane strain configurations exhibited forming limits close to the measured values but were clearly overestimated in both the rolling and traverse direction as strains approached biaxial symmetry.

Because roping in the form of ridges and valleys in the sheet surface is the manifestation of band clusters of grains with the same orientation, the material itself could be assumed to have varying material characteristics which are spatially distributed according to the sheet thickness. Thus, naive of information about this distribution of plasticity characteristics a scaling of the four-wave sine wave perturbation was performed to simulate furtherly reduced stiffness, in order to meet the strong anisotropy of forming limits as observed in experiments. The scaling was performed by multiplying the amplitude of each curve in the four-term sine wave model with a scalar to amplify the effect of roping.

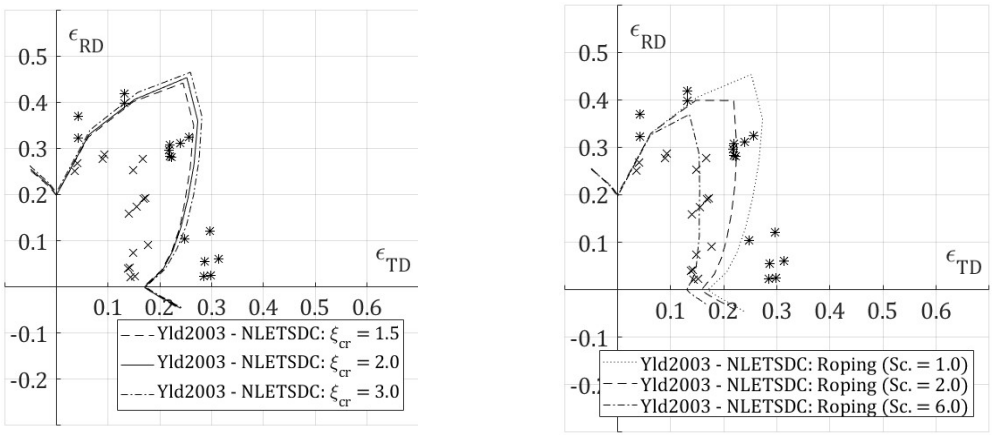

a) *b)*

Figure 5-8: a) Sensitivity analysis of the critical extremal thickness strain ratio in the NLETSDC. The analysis was carried out on a model with a four-term sine wave roping perturbation fitted to the measured mean thickness and standard deviation of sheets subject to experiments. b) Forming limit curves for the NLETSDC with different scales of the four-term sine wave perturbation.

From Fig. 5-8.b), it is evident that the effect of amplifying the roping perturbation model yielded a significant reduction in forming limit strains in the sheet's traverse direction. With an amplification six times the perturbation that was fitted to the artificial measurements, results from the FEA coincided superbly with forming limits measured for configurations where $\varepsilon_{TD} > \varepsilon_{RD}$. Nevertheless, the forming limit strains were still exaggerated by the FEA-model for its symmetric counterpart.

With roping modelled from the four harmonic functions, no thickness variations are introduced in the sheet's rolling direction. In the perturbation plot generated from white-light interferometry images by O. Engler presented in *Ch. 2.1.1*, the alternating valleys and ridges were accompanied by unstructured thickness deviations in the rolling directions as well. In an attempt to simulate this a FORTRAN-program, which generated random unstructured thicknesses perturbations based on a mean thickness and a standard deviation, was provided by Torodd Berstad at Structural Impact Laboratory (SIMLab) at the Norwegian University of Science and Technology. Each time the random thickness perturbation FORTRAN-program is run, different random thickness perturbations are generated.

As the random perturbation is added of top of the existing four-term sine wave perturbation, a rather moderate standard deviation of 0.002 mm was used along with the mean thickness of 1.496 mm. A scaling of six, which had proved to display excellent coincidence with the experimental local necking strains where $\varepsilon_{TD} > \varepsilon_{RD}$, was used for the four-term sine wave perturbation. Fig. 5-9 shows the comparison of the measured thickness perturbation in a 15 % elongated AA6016-T4 sheet as presented by O. Engler et al. [24] in a), to the undeformed described FEA-model in b).

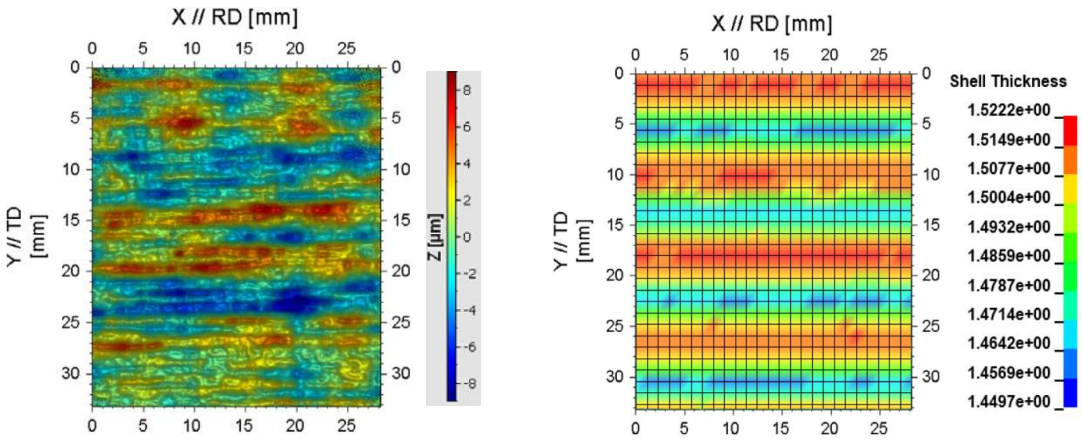

a) *b)*

Figure 5-9: a) Measured thickness perturbation for 15 % elongated AA6016-T4 rendered with permission from the 2012 article "Crystal-plasticity simulation of the correlation of microtexture and roping in AA 6xxx Al–Mg–Si sheet alloys for automotive applications" by O. Engler et al. [24] *with permission from the author. © 2012 Acta Materialia Inc. Published by Elsevier Ltd. All rights reserved. b) Thickness variation of the FEA-model with four-term sine wave perturbation (Sc. = 6) and random perturbation with SD = 0.002 mm.*

The FLCs produced by the six times amplified four-term sine wave perturbation, with and without the random perturbation with SD = 0.002 mm, are compared in Fig. 5-10. When the harmonic perturbation was accompanied by the random perturbation, the forming limits for strain paths when $\varepsilon_{TD} > \varepsilon_{RD}$ remained nearly unchanged, while its symmetric counterpart predicted drastically reduced necking strains, just on the conservative side of the experimentally detected forming limit strains indicated by the scattering of crosses. From this, it can be concluded that by introducing the two

perturbation models to the finite element analysis, both the shape and magnitudes of the experimentally detected forming limit strains can be simulated to good accuracy.

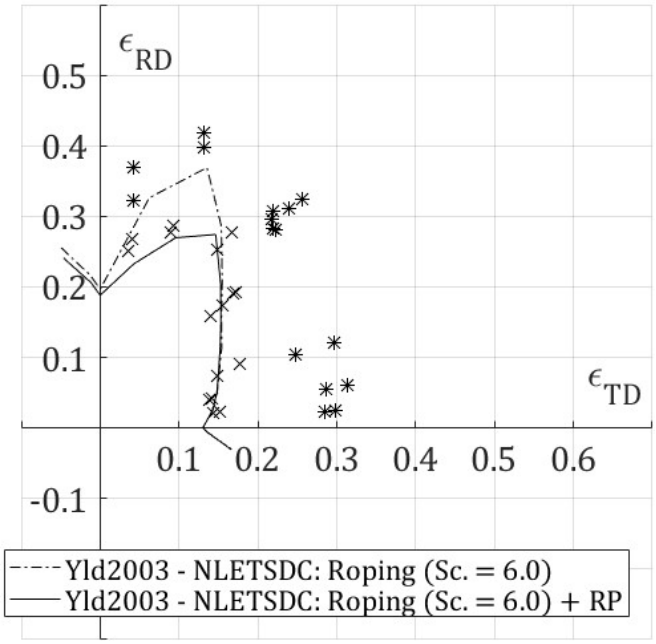

Figure 5-10: Forming limit curve with roping model (amplified six times), with and without additional random thickness perturbation with SD = 0.002 mm. The scatter of crosses and stars represents necking and fracture strain, respectively.

While the random thickness perturbation generator that was provided by Torodd Berstad generates different perturbations each time it is run, the same generation was used for the 15 different analysis which makes up the FEA-generated forming limit diagram, the same initial random thickness perturbation was used, yielding an even curve in biaxial strain space. As pointed out by Reyes et al. [6], who used the same random thickness perturbation approach was use, it should be noted that this is only one realization of the given input. This issue was investigated in the 2009 article by Fyllingen et al. [57] where random fields were used to model the spatial thickness variations in a Monte Carlo-coupled FEA. By varying the smoothness, effective range and the coefficient of variance of the random field, the generated stochastic FLD took the form of a rather wide band in biaxial strain space. Although the Monte Carlo-simulation is beyond the scope of the current study, further analyses with different perturbations generated from the same

random perturbation-program should be conducted before a more reliable FEA-generated FLD can be presented.

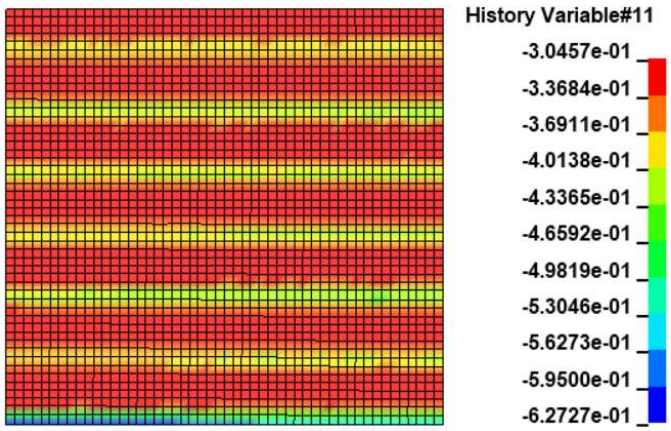

Figure 5-11: Logarithmic strains in the through-thickness direction, ε_t, at the onset of local necking according to the NLETSDC criterion for the analysis with displacement relationship $D_{TD}/D_{RD} = 0.7270$. The FEA-model is implemented with the Yld2003 yield function with four-term sine wave perturbation (Sc. = 6) and random perturbation (SD = 0.002). The plot displays strain localizations in the direction parallel to major strain.

Table 5-2 displays the registered necking strains and the crack direction relative to the rolling direction for the model with both the four-term sine wave perturbation scales six times, and the random perturbation with SD = 0.002 mm. In the analysis with displacement relationship $D_{TD}/D_{RD} = 0.7270$ (displayed in Fig. 5-11), the orientation of the crack was parallel to the rolling direction, i.e. parallel to the direction of major strain. The same phenomenon was observed during experiments, but for at a strain configuration where the major strain was furtherly dominant.

Table 5-2: FEA-generated necking strains and crack orientations relative to RD from the NLETSDC with four-term sine wave perturbation (Sc. = 6) and random perturbation (SD = 0.002).

Displacement ratio	Crack orientation to RD	Necking strains	
		ε_{RD}	ε_{TD}
$D_{TD}/D_{RD} = -0.1667$	/	*0.2409*	*-0.0465*
$D_{TD}/D_{RD} = -0.0500$	/	*0.2058*	*-0.0115*
$D_{TD}/D_{RD} = 0.0000$	⊥	*0.1881*	*0.0000*
$D_{TD}/D_{RD} = 0.1667$	⊥	*0.2326*	*0.0427*
$D_{TD}/D_{RD} = 0.3250$	⊥	*0.2697*	*0.0958*
$D_{TD}/D_{RD} = 0.5000$	*Undef.*	*0.2743*	*0.1465*
$D_{TD}/D_{RD} = 0.7270$	‖	*0.2046*	*0.1527*
$D_{TD}/D_{RD} = 1.0000$	‖	*0.1531*	*0.1531*
$D_{RD}/D_{TD} = 0.7270$	‖	*0.1128*	*0.1521*
$D_{RD}/D_{TD} = 0.5000$	‖	*0.0778*	*0.1501*
$D_{RD}/D_{TD} = 0.3250$	‖	*0.0505*	*0.1480*
$D_{RD}/D_{TD} = 0.1667$	‖	*0.0253*	*0.1429*
$D_{RD}/D_{TD} = 0.0000$	‖	*0.0000*	*0.1301*
$D_{RD}/D_{TD} = -0.0500$	‖	*-0.0074*	*0.1377*
$D_{RD}/D_{TD} = -0.1667$	‖	*-0.0306*	*0.1663*

5.2.3 Through-thickness shear instability criterion (TTSIC)

While the non-local criterions describing necking instabilities required initial imperfections in the strength of the analyzed specimens to generate physical results, the second local necking prediction model investigated in this study is based on the stress state and therefore can be used without the introduction of imperfections. Thus, the first FE-analysis with the TTSIC a patch with perfect uniform thickness was first carried out to explore the effects of plastic anisotropy on the forming limits. Then, the four-term sine wave perturbation was introduced with different scaling to the amplitudes of the four

waves, aiming to investigate its effects on anisotropy, and whether the criterion was able to recreate the necking strains observed in experimental measurements.

Curves representing necking instabilities predicted by the described models are displayed in Fig. 5-12, along with experimental necking strains and fracture strains, respectively indicated by crosses and stars.

Evidently, the model with perfectly uniform thickness was not able to produce the shape nor the magnitude of the forming limits from experiments. The model predicted necking strains slightly lower than what was observed in the experimental results for strain paths in the vicinity of plane strain with zero strains in the traverse. For strain paths approaching the equibiaxial axis and traverse strain-dominated configurations displayed overestimated limits. Strain paths with low strains in the rolling direction were also overestimated, but only moderately.

In compliance with the observation of Dimitry Vysochinskiy [10] of FLDs generated from the MK-model, where the anisotropy of the plasticity of AA6016-T4 encouraged anisotropy of forming limits in the opposite direction of what was observed in experiments, the finite element simulation predicted the same effect from through-thickness shear instability.

The predicted necking strains for strain paths which were nearly equibiaxial or traverse strain-dominated were effectively reduced with the introduction of the harmonic perturbation. I addition, the introduction of a roping model managed to accurately recreate the shape of the forming limit curve, which for the unperturbed model was deviating from the experiments. As the different scaling the roping model's amplitude only affected the strain paths where strains in the traverse directions were considerable, roping was observed to distinctly affects the anisotropy of necking strains in the direction of what was experimentally observed.

Although the TTSIC slightly underestimated necking strains for the equibiaxial and rolling direction strain-dominated strain paths, the model seems to serve as a good but slightly conservative criterion to describe local necking when the roping amplitudes were scaled six times what was initially fitted to the artificial thickness profile which was based on the mean thickness and standard deviation of measurements as described in *Ch. 4.5*.

Because the TTSIC does not require a random perturbation like the one provided from the FORTRAN-based program provided by Torodd Berstad for the NLETSDC, the shear-instability criterion could serve a useful tool for engineers without knowledge of coding, to substitute a non-local instability criterion in the detection of local necking limits.

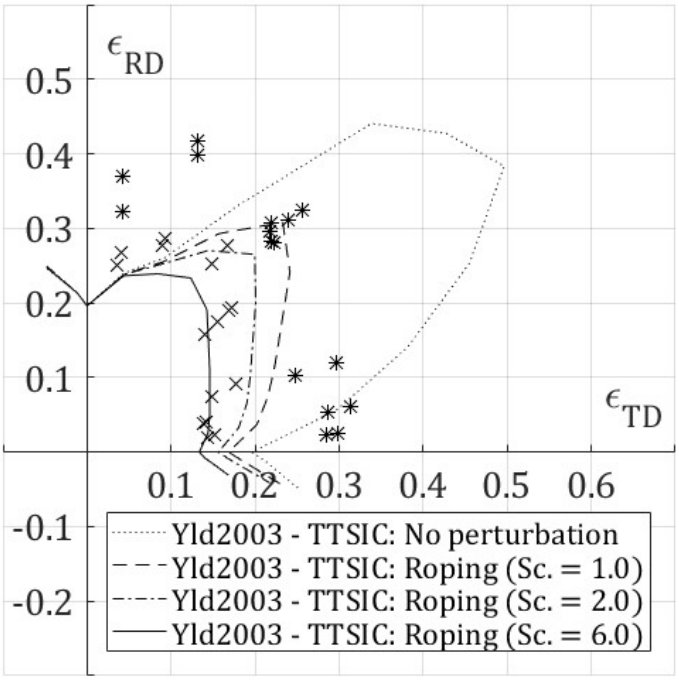

Figure 5-12: FEA-generated fracture limits from the through-thickness shear instability criterion with perfectly uniform thickness and with different scaling to the four-term sine wave roping model. The scatter of crosses and stars represents necking and fracture strain, respectively.

Table 5-3 shows the registered necking strains and the crack direction relative to RD for the model with both the four-term sine wave perturbation scales six times for the TTSIC criterion. For pure tension configurations where the major strain was parallel to RD, the model showed no significant necking direction. In the analysis with displacement relationship $D_{RD}/D_{TD} = 0.7270$ (displayed in Fig. 5-13), multiple local necks were produced. The same phenomenon was reportedly observed in several of the samples in the experimental program.

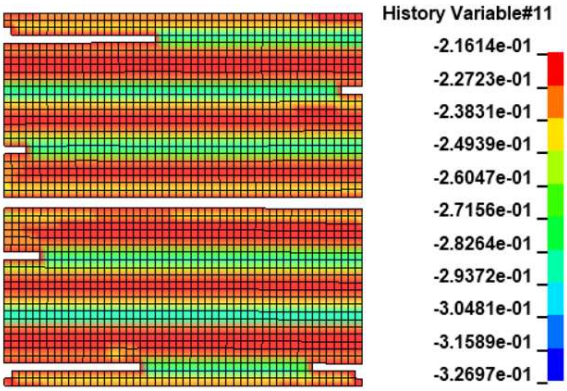

Figure 5-13: Logarithmic strains in the through-thickness direction, ε_t, at the first frame after element deletion by the TTSIC for the analysis with displacement relationship $D_{RD}/D_{TD} = 0.7270$. The FEA-model is implemented with the Yld2003 yield function with four-term sine wave perturbation (Sc. = 6). The plot displays the formation of multiple local necks as a result of roping.

Table 5-3: FEA-generated necking strains and crack orientations relative to RD from the TTSIC with four-term sine wave perturbation (Sc. = 6).

Displacement ratio	Crack orientation to RD	Necking strains	
		ε_{RD}	ε_{TD}
$D_{TD}/D_{RD} = -0.1667$	⊥	*0.2476*	*-0.0480*
$D_{TD}/D_{RD} = -0.0500$	⊥	*0.2136*	*-0.0120*
$D_{TD}/D_{RD} = 0.0000$	⊥	*0.1961*	*0.0000*
$D_{TD}/D_{RD} = 0.1667$	*Undef.*	*0.2364*	*0.0435*
$D_{TD}/D_{RD} = 0.3250$	*Undef.*	*0.2390*	*0.0841*
$D_{TD}/D_{RD} = 0.5000$	*Undef.*	*0.2334*	*0.1235*
$D_{TD}/D_{RD} = 0.7270$	*Undef.*	*0.1912*	*0.1425*
$D_{TD}/D_{RD} = 1.0000$	‖	*0.1446*	*0.1446*
$D_{RD}/D_{TD} = 0.7270$	‖ *(multiple)*	*0.1082*	*0.1460*
$D_{RD}/D_{TD} = 0.5000$	‖	*0.0756*	*0.1459*
$D_{RD}/D_{TD} = 0.3250$	‖	*0.0498*	*0.1460*
$D_{RD}/D_{TD} = 0.1667$	‖	*0.0255*	*0.1439*
$D_{RD}/D_{TD} = 0.0000$	‖	*0.0000*	*0.1335*
$D_{RD}/D_{TD} = -0.0500$	‖	*-0.0075*	*0.1398*
$D_{RD}/D_{TD} = -0.1667$	‖	*-0.0310*	*0.1683*

5.2.4 Original Cockcroft-Latham fracture criterion (OCLFC)

While the NLESD/NLIC is based on relationships of strains and strain rates, and the TTSIC is only dependent on the current stress state in the material, the original Cockcroft-Latham – which unlike the two others is a fracture criterion – works as a limit to the plastic work performed by the tensile major principle stress, and thus considers the history of loading. For the patches subjected to proportional strain paths in this study, this nature of the OCLFC is mainly of theoretical importance. Just like the TTSIC, the limit to the positive plastic work of the major principle stress does not need any initial imperfections to the strength of the analysed component for the critical limit to be reached.

Thus, the same procedure as with the TTSCI was followed, starting with a patch perfectly uniform in the through-thickness directions, before the four-term sine wave roping model was introduced with different scaling. In the forming limit diagram presented in Fig. 5-14, the FEA-generated curves were plotted along with scatters of necking strains and fracture strains represented by crosses and starts respectively. Unlike the two necking instability criteria, where comparisons to the necking stains are of greatest interest, the OCLFC-generated fracture limit curve should naturally be compared to the experimental fracture limits

Even if the ductile fracture criterion describes a different phenomenon, many of the same observations made from the corresponding curves produced with the TTSIC were recognized in the analysis with the OCLFC as the fracture limit. For the unperturbed patch, were the plasticity model was the only source of anisotropy in the model, the fracture limit curve displayed anisotropy of opposite nature compared to what was observed in experiments. With the introduction of the harmonic perturbation, fracture limits in the traverse direction were effectively reduced with different scaling. The magnitudes of the predicted fracture strains were undershot for the strain paths in the vicinity to the two plane-strain axes, while strains were within the range of experimental scatter or larger when approaching the equibiaxial configurations. Due to this – although the introduction of roping helped – the original Cockcroft-Latham fracture criterion was not able to satisfyingly recreate the shape of the fracture strains.

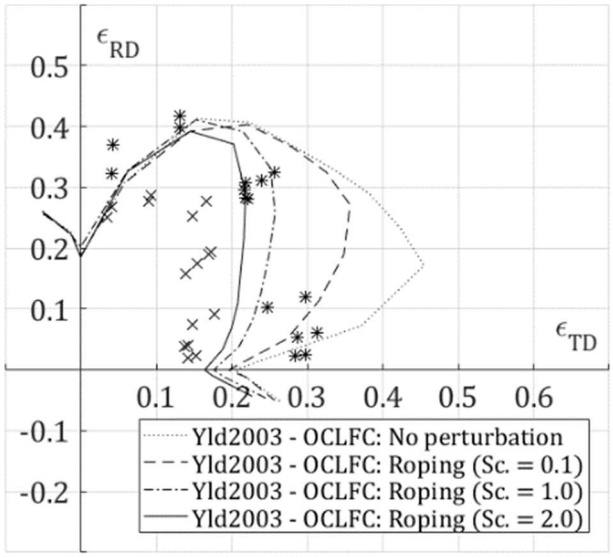

Figure 5-14: FEA-generated fracture limits from the original Cockcroft-Latham fracture criterion with perfectly uniform thickness and with different scaling to the four-term sine wave roping model. The scatter of crosses and stars represents necking and fracture strain, respectively.

Table 5-4 displays the registered necking strains and the crack direction relative to RD for the model with both the four-term sine wave perturbation scales six times for the OCLFC criterion. The OCLFC managed to produce comparable results to the NLETSDC regarding crack orientation. The analysis with displacement relationship $D_{RD}/D_{TD} = 0.5000$ (displayed in Fig. 5-15), which did not yield a single definite crack direction by use of the NLETSDC, exhibited multiple cracks parallel to the rolling direction with the ductile fracture criterion. With the non-local strain in RD at twice the magnitude of the non-local TD strain, the model seems to somewhat predict the unexpected directions of cracks in the AA6016-T4 sheets subjected to roping.

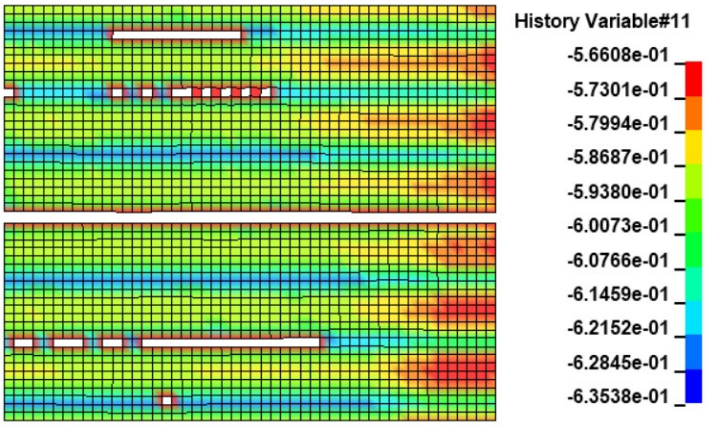

Figure 5-15: Logarithmic strains in the through-thickness direction, ε_t, at the first frame after element deletion by the OCLFC for the analysis with displacement relationship $D_{RD}/D_{TD} = 0.5000$. The FEA-model is implemented with the Yld2003 yield function.

Table 5-4: FEA-generated necking strains and crack orientations relative to RD from the OCLFC with the unscaled four-term sine wave perturbation.

Displacement ratio	Crack orientation to RD	Fracture	
		ε_{RD}	ε_{TD}
$D_{TD}/D_{RD} = -0.1667$	/	*0.2605*	*-0.0509*
$D_{TD}/D_{RD} = -0.0500$	/	*0.2212*	*-0.0125*
$D_{TD}/D_{RD} = 0.0000$	⊥	*0.2019*	*0.0000*
$D_{TD}/D_{RD} = 0.1667$	⊥	*0.3279*	*0.0627*
$D_{TD}/D_{RD} = 0.3250$	⊥	*0.4107*	*0.1528*
$D_{TD}/D_{RD} = 0.5000$	‖ *(multiple)*	*0.3916*	*0.2149*
$D_{TD}/D_{RD} = 0.7270$	‖	*0.3316*	*0.2514*
$D_{TD}/D_{RD} = 1.0000$	‖	*0.2574*	*0.2574*
$D_{RD}/D_{TD} = 0.7270$	‖	*0.1871*	*0.2491*
$D_{RD}/D_{TD} = 0.5000$	‖	*0.1266*	*0.2389*
$D_{RD}/D_{TD} = 0.3250$	‖	*0.0795*	*0.2269*
$D_{RD}/D_{TD} = 0.1667$	‖	*0.0381*	*0.2097*
$D_{RD}/D_{TD} = 0.0000$	‖	*0.0000*	*0.1763*
$D_{RD}/D_{TD} = -0.0500$	‖	*-0.0104*	*0.1882*
$D_{RD}/D_{TD} = -0.1667$	‖	*-0.0480*	*0.2476*

6 Discussion

A substantial share of the hours spent during the work on the current thesis was dedicated to becoming familiar with, and to calibrate the linear transformation-based anisotropic yield functions. In earlier stages of the project, the plan was to conduct FEA with all the presented yield and hardening functions in order to evaluate the different plasticity models' effects on the forming limits. However, in order to implement the presented failure models, the *WTM_STM*-keyword was used, where only the yield functions Yld89 and Yld2003, in conjunctions with the two-term Voce rule hardening model were available through the pre-programmed modules. As the Yld89 model seemingly produced unexplainable stress concentrations as displayed in Fig. 5-2, the scope of the non-linear FEA was restricted to the Yld2003 plasticity model. Initially, the Yld2003 yield function model was not one of the assessed models in this study and had therefore not been included in the calibration program, but the material model *WTM_STM* in LS-DYNA provides the possibility to automatically calibrate the eight-term yield function from eight experimental data point. However, information about which calibration method LS-DYNA uses is not described in the software-manual [56], and the initial plan to investigate the impact of different calibration methods was discarded. From the calibration results, the Yld2000-2d yield functions were able to provide good fits to the experimental data for both the weighted and non-weighted calibration, while the Yld89 functions – which were generally less accurate – were more sensitive to different calibration methods. Whether this would have been reflected in FLDs produced by FEA remains unanswered.

In the results presented from the calibrations of the isotropic hardening functions, the saturations of the one and two-term Voce hardening rule at high strains were discussed. From the comparison between the experimental curve from the uniaxial tensile test sample UT0-1 and the two-term Voce curve which was later used in the FE-analyses, the fitted curve seemingly displayed somewhat reduced stiffness than what could be imagined would be the continuation of the experimental curve, which ended at plastic strain value of 0.268. When later conducting FEA of biaxially deformed patches, some of the samples reached local effective plastic strain values well beyond twice this magnitude. The *WTM_STM*-keyword which was used to implement the plasticity model

in LS-DYNA provides the possibility to specify a lower limit to the isotropic hardening rate [56], where a linear hardening model with the constant term E_{min} takes over when the slope of the Voce function falls below the slope specified by the linear stiffness modulus. Unfortunately, this extension of the two-term Voce rule in the *WTM_STM*-keyword was not discovered until after the analyses were conducted.

Along with the Yld2003 yield function, the unidirectional harmonic perturbation with the proper scaling managed to reproduce local necking instability limits to good accuracy by the TTSIC. However, the NLETSDC – which is a criterion to detect local necking by strain locations which occur as a consequence of material imperfections, inspired by the work of Marciniak and Kuczynski [4] – overestimated the magnitudes of strains at necking with the roping model alone, as the model does not introduce imperfections in the sheet's rolling direction. Therefore, an extension to the unidirectional harmonic perturbation was provided by Dr Torodd Berstad at SIMLab at NTNU in the form of a FORTRAN-program which generated a field of random perturbation, using a mean thickness and a standard deviation as input. By adding the random perturbation with a standard deviation of 0.002 mm to the unidirectional harmonic roping model, the FEA-generated FLC took on a shape which coincided excellently with the band of experimental values, with slightly conservative values for necking strains in the rolling direction. Nevertheless, a reminder of the issue addressed in the discussion following the presented FLC in *Ch. 5.2.2* about the scattering results which may be produced with such random perturbation programs is appropriate. The random perturbation used in the presented results is only one of infinitely any realization of the given input. Beyond the statistical boundary condition of the specified standard deviation, the analyst has no control over the shell thickness generated at each node, unless the generated thicknesses are checked prior to conducting the analysis. Although non-physical conditions are unlikely to occur, differences in smoothness and effective range were reported in the 2009 article by Fyllingen et al. [57] to cause relatively large scatters in forming limits.

As displayed in Fig. 5-10 in *Ch. 5.2.2*, the thickness field which was generated with the unidirectional four-term sine wave model accompanied with the random perturbation-extension displayed a better visual resemblance to the measured topography of 15 % elongated AA6016-T4 sheets presented by Engler et al. [24], where thickness-deviations

were observed along the valleys and ridges from roping. However, with access to such measurement data in a future study, the demand for a random perturbation could be eliminated. Instead of relying on a randomly distributed perturbation to simulate the uneven nature of valleys and ridges in the rolling direction, a two-dimensional harmonic perturbation-model, as presented in Eq. 3.3-20, could instead be fitted directly to the two-dimensional data to serve the same purpose.

With the FLCs sensitivity to scaling of the roping model, multiple analysis where the amplitudes of the four harmonic functions were magnified by the same scalar in order to target the experimentally observed forming limits. This procedure was carried out for the three different failure criteria. When multiple analyses are conducted in a trial-and-error fashion, discretely changing variables to target a good fit, a tool to handle the masses of information of more and less obvious correlations among the many history variables is called for. With the rapid development in the increasingly recognized field of machine learning (ML), the implementation of such algorithms to streamline trail-and-error tasks and to recognize inconspicuous correlations in FEA-results could be a very interesting next step in the field of metal sheet forming.

7 Summary and concluding remarks

In this thesis, a short introduction to aluminium alloys as a material, along with a general presentation to key theory relevant to aluminium sheet forming was given.

Then, a number of material models which are used to describe the plasticity, work hardening and failure for aluminium alloys were presented, including four anisotropic yield functions, four models to describe isotropic work hardening and five models to describe failure. Here, one of the presented failure models was proposed by the author to replace the non-local instability criterion (NLIC) due to difficulties which were met during later implementation in the FEA-software LS-DYNA. Additionally, a method to model the effects roping – a phenomenon sometimes observed in aluminium alloy sheets – by thickness perturbations described as a sum of multiple harmonic functions, was presented.

Furthermore, several of the presented material models were calibrated to data from experiments conducted by Dimitry Vysochinskiy [10] on sheets of aluminium alloys AA6016-T4 where the phenomenon of roping was observed to strongly affect the anisotropy of necking and fracture strains. In this work, programs to calibrate the linear transformation-based anisotropic yield functions Yld89 [5] and Yld2000-2d [16] were written in Microsoft-Excel, for future in-house use. From the results of the calibrations of the anisotropic yield functions, the quadratic Hill48 yield function with four plane stress anisotropy coefficients was considered unsuited to describe the plasticity of the alloy, further confirming the established fact that such quadratic yield functions are inadequate to simulate the behaviour of metals with FCC crystal structure [55]. The non-quadratic yield function Yld89 was more successful in the task with the same number of coefficients, although an accurate fit to the experimental data could not be obtained simultaneously for both the flow-stresses and the traverse strain ratios. The eight-term non-quadratic yield functions Yld2000-2d were both able to closely resemble the experimentally measured quantities of the AA6016-T4 aluminium alloy. The same was observed for the Yld2003 yield function, which was later calibrated automatically in the FEA-software LS-DYNA. Different methods were used to calibrate the two yield

functions Yld89 and Yld2000-2d, where a weighted MSSE-approach was preferred for enhanced flexibility.

In *Ch. 5*, an attempt was made to produce FEA-based forming limit diagrams (FLD) for aluminium alloy AA6016-T4 subjected to the roping. On a 60 mm by 60 mm patch of 50x50 Belytschko-Tsay shell elements with five integration points in the though-thickness direction, the effect of roping was simulated by a unidirectional four-term sine wave perturbation model, which was fitted to a fictive thickness profile generated based on the available information in the PhD-thesis of Dimitry Vysochinskiy [10]. 15 non-local proportional strain paths were run to construct the diagrams.

The non-quadratic anisotropic yield function Yld2003 by H. Aretz [17] was used along with the associate flow rule and isotropic two-term Voce hardening. Accompanied with a FORTRAN-generated random thickness perturbation, the model excellently reconstructed experimental local necking strains from MK-tests by a non-local extremal thickness strain deviation criterion (NLETSDC) when the amplitude of the harmonic roping perturbation was scaled six times. Also, a through-thickness shear instability criterion (TTSIC) [7] generated very similar results without the extension of the FORTRAN-generated random perturbation to the roping model, although strains in the sheets rolling direction were somewhat conservative. The original Cockcroft-Latham ductile fracture criterion (OCLFC) [9] was also tested with the four-term harmonic perturbation to see if the model would recreate fracture strains observed in the same experiments. While the model did manage to predict somewhat accurate fracture strains for strain paths in the vicinity of equibiaxial strains, the model underestimated fracture strains for the plane strain configurations and was not considered suited to fulfil its purpose.

When the models were run without the introduction of the harmonic roping model, all three criteria produced FLDs with anisotropic characteristics opposite to what was observed in experiments. From this, the conclusion drawn by Dimitry Vysochinskiy [10], that the plasticity's effect on the forming limits were overruled by the effect of roping, was furtherly confirmed. The predicted forming and fracture limits in the traverse direction from the three models were all sensitive to the introduction of the harmonic perturbation model. The best fit to experiments was achieved when the four-term sine

wave perturbation, which was initially fitted to the amplitudes of measured thickness deviations, was scaled to a factor of 6. This was justified by the assumption that the spatial distribution of macroscopic valleys and ridges in the surface of sheets due to roping, also represents a spatial distribution of varying plasticity characteristics.

From this, it can be concluded that the method of introducing thickness perturbations in a shell-based FEA described as a sum of harmonic functions based on the spatial distribution of macroscopic valleys and ridges in the sheet surface, was successful in describing the effects of roping of forming limits from proportional strain paths in AA6016-T4 aluminium alloy sheets.

As discussed in the *Ch. 2.3.1* a weakness of the FLD is that it only serves as a valid damage criterion for processes of proportional strain paths. As the strain path in a piece of material during metal sheet forming might very well expect a varying history of strain ratios, a natural next step in further research would be to conduct similar analyses with the introduction of non-proportional strain paths, to see if the applied method is capable of generating similarly accurate descriptions is such cases. Another question which remains unanswered for further research is whether the effects of different yield functions and calibration methods would have been reflected in the FEA-generated FLDs with the use of the implemented roping model.

Additionally, utilization of the rapidly evolving field of machine learning to streamline trail-and-error tasks and to recognize inconspicuous correlations in FEA-results is also suggested as a direction for further research in the field of metal sheet forming.

References

[1] R. Hill, “A Theory of the Yielding and Plastic Flow of Anisotropic Metals,” *Mathematical and Physical Sciences,* vol. 193, pp. 281-297, 27 May 1948.

[2] A. V. Hershey, “The plasticity of an isotropic aggregate of anisotropic cubic crystals,” *J. Appl. Mechanics,* pp. 241-249, 1954.

[3] R. W. Logan and W. F. Hosford, “Upper bound anisotropic yield locus calculations assuming 〈111〉-pencil glide,” *International Journal of Mechanical Sciences,* vol. 22, pp. 419-430, 1980.

[4] Z. Marciniak and K. Kuczynski, “Limit strains in the processes of stretch-forming sheet metal,” *International Journal of Mechanical Sciences, 9(9),* vol. 9, pp. 609-620, 1967.

[5] F. Barlat and J. Lian, “Plastic behaviour and stretchability of sheet metals. Part I: A yield function for orthotropic sheets under plane stress conditions,” *International Journal of Plasticity,,* vol. 5, pp. 51-66, 1989.

[6] A. Reyes, O. S. Hopperstad, T. Berstad and O.-G. Lademo, “Prediction of necking for two aluminum alloys under non-proportional loading by using an FE-based approach,” *International Journal of Material Forming,* pp. 211-232, December 2008.

[7] J. D. Bressan and J. A. Williams, “The use of a shear instability criterion to predict local necking in sheet metal deformations,” *International Journal of Mechanical Sciences,* vol. 25, pp. 155-168, 1983.

[8] O. -G. Lademo, O. Engler, S. Keller, T. Berstad, K. Pedersen and O. S. Hopperstad, “Identification and validation of constitutive model and fracture criterion for AlMgSi alloy with application to sheet forming,” *Materials and Design,* p. 3005–3019, 2009.

[9] M. G. Cockcroft and D. J. Latham, “Ductility and the Workability of Metals,” *Journal Institute of Metals,* vol. 68, pp. 33-39, 1968.

[10] D. Vysochinskiy, “Formability of aluminium alloy, Thesis for the degree of Philosophiae Doctor,” Norwegian University of Science and Technology Faculty of Engineering Science and Technology Department of Structural Engineering, Trondheim, Norway, 2014.

[11] F. Barlat, H. Aretz, J. Yoon, M. Karabin, J. Brem and R. Dick, “Linear transfomation-based anisotropic yield functions,” *International Journal of Plasticity,* vol. 21, pp. 1009-1039, 2005.

[12] S. Tveit, “Non-linear finite element analysis of cantilever I-section of 6082 T6 aluminium alloy,” Oslo Metropolitan University, Oslo, Norway, 2019.

[13] S. Tveit, “Preliminary study: Formability of aluminum alloy AA6016,” Oslo Metropolitan University, Oslo, Norway, 2019.

[14] R. v. Mises, “Mechanik der festen Körper im plastisch-deformablen Zustand,” *Nachrichten von der Gesellschaft der Wissenschaften zu Göttingen. Mathematisch-Physikalische Klasse,* pp. 582-592, 1913.

[15] W. F. Hosford and R. M. Candell, “13 - Plastic Anisotropy,” in *Metal Forming: Mechanics and Metallurgy*, 3rd ed., Cambridge, Cambridge University Press, 2007, pp. 207-219.

[16] F. Barlat, J. Brem, J. Yoon, K.Chung, R. Dick, D. Lege, F. Pourboghrat, S.-H. Choi and E. Chu, “Plane stress yield function for aluminum alloy sheets—part 1: theory,” *International Journal of Plasticity,* vol. 19, p. 1297–1319, 2003.

[17] H. Aretz, “A non-quadratic plane stress yield function for orthotropic sheet metals,” *Journal of Materials Processing Technology,* vol. 168, no. 1, pp. 1-9, 15 September 2005.

[18] F. Andrade, M. Feucht, A. Haufe and F. Neukamm, “An incremental stress state dependent damage model for ductile failure prediction,” *International Journal of Fracture,* vol. 200, pp. 127-150, 3 February 2016.

[19] MSKS IP Inc, “Aluminum and the Auto Industry,” Metal Supermarkets, 21 May 2015. [Online]. Available: https://www.metalsupermarkets.com/aluminum-and-the-auto-industry/. [Accessed 5 May 2020].

[20] “Om aluminium - Livssyklusen til aluminium,” Norsk Hydro ASA, 27 February 2019. [Online]. Available: https://www.hydro.com/no-NO/om-aluminium/livssyklusen-til-aluminium/. [Accessed 5 May 2020].

[21] Nameplates Div, “How Aluminum Plates and Sheets are Made,” Nameplates Div, 2017. [Online]. Available: https://nameplatesdiv.com/how-aluminum-plates-and-sheets-are-made/. [Accessed 5 May 2020].

[22] The Aluminum Association, “Aluminum Alloys 101,” The Aluminum Association, [Online]. Available: https://www.aluminum.org/resources/industry-standards/aluminum-alloys-101. [Accessed 6 May 2020].

[23] MSKS IP Inc., “The Aluminum Numbering System,” Metal Supermarkets, 11 January 2018. [Online]. Available: https://www.metalsupermarkets.com/aluminum-numbering-system/. [Accessed 6 May 2020].

[24] O. Engler, C. Schäfer and H.-J. Brinkman, “Crystal-plasticity simulation of the correlation of microtexture and roping in AA 6xxx Al–Mg–Si sheet alloys for automotive applications,” *Acta Materialia 60,* vol. 60, no. 13-14, pp. 5217-5232, 2012.

[25] P. Bate, “Texture inhomogeneity and limit strains in aluminium sheet,” *Scripta Metallurgica et Materialia,* vol. 27, p. 515–520, 1992.

[26] P. D. Wu, D. J. Lloyd, A. Bosland, H. Jin and S. MacEwen, “Analysis of roping in AA6111 automotive sheet,” *Acta Materialia,* p. 1945–1957, 27 November 2003.

[27] Wikimedia Commons, “File: Components stress tensor.svg,” Wikimedia Commons, the free media repository, 2014.

[28] W. Hosford and R. Caddell, Metal Forming: Mechanics and Metallurgy, 4. ed., Cambridge: Cambridge University Press, 2011.

[29] W. F. Hosford, "A Generalized Isotropic Yield Criterion," *Journal of Applied Mechanics,* vol. 39, no. 2, p. 607, 1972.

[30] A. A. Mamun, J. Kelleher, R. Moat and P. J. Bouchard, “Origin of the Bauschinger effect in a polycrystalline material,” *Materials Science and Engineering: A,* vol. 707, pp. 576-584, 7 November 2017.

[31] M. Rosenschon and M. Merklein, “Analysis of the stress and directional dependent Bauschinger-effect of sheet metals,” in *IOP Conf. Series: Materials Science and Engineering 418*, Waterloo, 2018.

[32] H. Eggleston, “GENERAL PROPERTIES OF CONVEX FUNCTIONS,” in *Convexity*, Cambridge, Cambridge University Press, 1958, pp. 45-58.

[33] M. Marcus and H. Minc, A Survey of Matrix Theory and Matrix Inequalities, New York: Dover, 1988, p. 69.

[34] W. F. Langford, S. C. Snyder and J. Bausch, “New criteria for predicting the press performance of deep drawing steels,” *Trans, Amer. Soc. Metals,* vol. 42, pp. 1197-1232, 1950.

[35] L. Yang, L. Smith, A. Gothekar and X. Chen, “Measure Strain Distribution Using Digital Image Correlation,” Oakland University, Dept. of Mechanical Engineering, Rochester, MI, 2010.

[36] H. Hooputra, H. Gese, H. Dell and H. Werner, “A comprehensive failure model for crashworthiness simulation of aluminium extrusions,” *International Journal of Crashworthiness,* vol. 69, pp. 449-464, 2014.

[37] Z. Marciniak, J. Hu and J. Duncan, “Load instability and tearing,” in *Mechanics of Sheet Metal Forming*, 2nd ed., Elsevier Science & Technology/Butterworth-Heinemann, 2002, p. 80.

[38] G. M. Goodwin, “Application of strain analysis to sheet metal forming problems in the press shop,” *SAE Technical Paper 680093,* 1968.

[39] S. P. Keeler, “Circular grid system – a valuable aid for evaluating sheet metal formability,” *SAE Technical Paper 680092,* 1968.

[40] International Organization for Standardization, “ISO 12004-2: Metallic materials - Sheet and strip - Determination of forming-limit curves - Part 2: Determination of forming limit curves in the laboratory,” International Organization for Standardization, Geneva, Switzerland, 2008.

[41] D. Vysochinskiy, T. Coudert, O. S. Hopperstad, O.-G. Lademo and A. Reyes, “Experimental detection of the onset of local necking in an aluminium sheet,” *Materials Science Forum,* Vols. 794-796, pp. 590-595, 2014.

[42] K. Yoshida and T. Kuwabara, “Effect of strain hardening behavior on forming limit stresses of steel tube subjected to nonproportional loading paths,” *International Journal of Plasticity,* vol. 23, p. 1260–1284, July 2007.

[43] D. Zeng, L. Chappuis, Z. C. Xia and X. Zhu, “A path independent forming limit criterion for sheet metal forming simulations,” *SAE International Journal of Materials and Manufacturing,* vol. 1, no. 1, pp. 809-817, 2009 April 2008.

[44] S. Gatea, H. Ou, B. Lu and D. G. Mccartney, “Modelling of ductile fracture in single point incremental forming using a modified GTN model,” *Engineering Fracture Mechanics ,* vol. 186, pp. 59-79, December 2017.

[45] S. Zhang, L. Leotoing, D. Guines and S. Thuillier, “Calibration of material parameters of anisotropic yield,” in *16th annual ESAFORM Conference on Material Forming*, Aviero, Portugal, 2013.

[46] F. Barlat and O. Richmond, “Prediction of Tricomponent Plane Stress Yield Surfaces and Associated Flow and Failure Behavior of Strongly Textured F.C.C. Polycrystalline Sheets,” *Materials Science and Engineering,* vol. 95, pp. 15-29, November 1987.

[47] J. Zhu, S.-y. Huang, W. Liu, J.-h. Hu and X.-f. Zou, “Calibration of anisotropic yield function by introducing plane strain test instead of equi-biaxial tensile test,” *Transactions of Nonferrous Metals Society of China,* vol. 28, no. 11, pp. 2307-2313, 28 November 2018.

[48] O. Kraft, “Thin Films: Mechanical Testing,” in *Encyclopedia of Materials: Science and Technology*, 2 ed., Oxford, Pergamon/Elsevier, 2001, pp. 9257-9261.

[49] Livermore Software Technology Corporation (LSTC), *LS-DYNA® KEYWORD USER'S MANUAL,* vol. I, 2018.

[50] M. Brunet and P. Clerc, “Two prediction methods for ductile sheet metal failure,” in *10th ESAFORM Conference on Material Forming*, Zaragoza, Spain, 2007.

[51] J. Lemaitre, “A Continuous Damage Mechanics Model for Ductile Fracture,” *Journal of Engineering Materials and Technology,* vol. 107, pp. 83-89, January 1985.

[52] MATLAB & Simulink, “Sum of Sine Models - R2020a,” MathWorks Nordic, [Online]. Available: https://se.mathworks.com/help/curvefit/sum-of-sine.html. [Accessed 7 April 2020].

[53] P. D. Wu and D. J. Lloyd, “Analysis of surface roughening in AA6111 automotive sheet,” *Acta Materialia,* vol. 52, pp. 1785-1798, 19 April 2004.

[54] D. Baranic, “2.1.1 Uniaxial Anisotropy Coefficients,” in *Sheet Metal Forming Processes - Constitutive Modelling and Numerical Simulation*, Berlin Heidelberg, Springer Verlag, 2010, pp. 30-36.

[55] P. Dasappa, K. Inal and R. Mishra, "The effects of anisotropic yield functions and their material parameterson prediction of forming limit diagrams," *The effects of anisotropic yield functions and their material parameterson prediction of forming limit diagramsPrasad Dasappaa, Kaan Inala,⇑, Raja MishrabaDepartment Mechanical and Mechatronics Engineering, University of Waterloo, Waterloo, ON, Canada N2L,* vol. 49, no. 25, pp. 3528-3550, 1 December 2012.

[56] Livermore Software Technology Corporation (LSTC), *LS-DYNA® KEYWORD USER'S MANUAL - Material Models,* vol. II, 2018.

[57] Ø. Fyllingen, O. Hopperstad, O.-G. Lademo and M. Langseth, “Estimation of forming limit diagrams by the use of the finite element method and Monte Carlo simulation,” *Computers and Structures,* no. 87, pp. 128-139, 2009.

[58] F. Barlat, D. J. Lege and J. C. Brem, “A six-component yield function for anisotropic materials,” *International Journal of Plasticity,* pp. 693-712, 1991.

[59] F. A. C. M. Habraken and J. H. Dautzenberg, “Some Applications of the Barlat 1991 Yield Criterion,” *CIRP Annals,* pp. 185-188, 1995.

[60] W. F. Hosford and W. A. Backofen, Fundamentals of Deformation Processing, Syracuse, New York: Syracuse University Press, 1964, pp. 259-298.

[61] P. D. Wu, D. J. Lloyd and S. R. MacEwen, “A simple model describing roping in A1 sheet,” *Scripta Materialia,* vol. 48, p. 1243–1248, 2003.

[62] A. Guillotin, G. Guiglionda, C. Maurice and a. J. H. Driver, “Correlation of Surface Roping with Through-Thickness Microtextures in an AA6xxx Sheet,” *Metallurgical and Materials Transactions A,* vol. 42, pp. 1919-1924.

[63] T. Stoughton, “General forming limit criterion for sheet metal forming,” *International Journal of Mechanical Sciences,* vol. 42, pp. 1-27, January 2000.

[64] M. Butuc, J. Gracio and A. B. D. Rocha, “An experimental and theoretical analysis on the application of stress-based forming limit criterion,” *International Journal of Mechanical Sciences,* vol. 48, pp. 414-429, April 2006.

[65] P. D. Wu, A. Graf, S. R. MacEwen, D. J. Lloyd and K. W. N. M. Jain, “On forming limit stress diagram analysis,” *International Journal of Solids and Structures,* vol. 42, pp. 2225-2241, April 2005.

[66] K. Yoshida, T. Kuwabara and M. Kuroda, “Path-dependence of the forming limit stresses in a sheet metal,” *International Journal of Plasticity,* vol. 23, pp. 361-384, March 2007.

[67] K. Marciniak, K. Kuczynski and T. Pokora, “Influence of the plastic properties of a material on the forming limit diagram for sheet metal in tension,” *International Journal of Mechanical Science,* vol. 15, no. 10, pp. 789-800, October 1973.

[68] C. Mühlstätter and M. Hartmann, “Material modelling of cast aluminum by application of the Wilkins damage model,” in *ECCOMAS*, Crete, Greece, 2016.

[69] F. Neukamm, M. Feucht, A. Haufe and K. Roll, “On Closing the Constitutive Gap Between Forming and Crash Simulations,” in *10th International LS-DYNA(R) User Conference - Metal Forming*, Stuttgart, Germany, 2008.

[70] H. Wang, M. Wan, X. Wu and Y. Yan, “The equivalent plastic strain-dependent Yld2000-2d yield function and the experimental verification,” *Computational Materials Science,* pp. 12-22, 10 June 2009.

[71] T. A. Bennett, R. H. Petrov and L. A. I. Kestens, “Texture-induced surface roping in an automotive aluminium sheet,” *Scripta Materialia,* vol. 81, pp. 733-736, 2009.